Rock mechanics, failure phenomena with pre-existing cracks and internal fluid flow through cracks

Nikolić, Mijo

ENSC-2014/2015

THÈSE DE DOCTORAT
DE L'ÉCOLE NORMALE SUPÉRIEURE DE CACHAN

Présentée par

Mijo Nikolić

pour obtenir le grade de

DOCTEUR DE L'ÉCOLE NORMALE SUPÉRIEURE DE CACHAN

Domaine

MÉCANIQUE - GÉNIE MÉCANIQUE - GÉNIE CIVIL

Sujet de la thèse

Rock mechanics, failure phenomena with pre-existing cracks and internal fluid flow through cracks

Soutenue à Split le 28 septembre 2015 devant le jury composé de :

Hermann G. Matthies	Professeur, TU Braunschweig	Président
Bernhard A. Schrefler	Professeur, Université de Padoue	Rapporteur
Ivica Kožar	Professeur, University of Rijeka	Rapporteur
Adnan Ibrahimbegovic	Professeur, UT Compiegne	Directeur de thèse
Predrag Miščević	Professeur, University of Split	Co-directeur de thèse

LMT-Cachan
ENS Cachan / CNRS / UPMC / PRES UniverSud Paris
61 avenue du Président Wilson, F-94235 Cachan cedex, France

ÉCOLE NORMALE SUPÉRIEURE DE CACHAN
Laboratoire de Mécanique et Technologie

UNIVERSITY OF SPLIT
Faculty of Civil Engineering, Architecture and Geodesy

Mijo Nikolić

Rock mechanics, failure phenomena with pre-existing cracks and internal fluid flow through cracks

Doctoral dissertation

Cachan, Split, 2015

Mijo Nikolić

Serial number: 39

This doctoral dissertation has been submitted for evaluation to Faculty of Civil Engineering, Architecture and Geodesy of University of Split, for the purpose of obtaining the doctoral degree in the field of Technical sciences, scientific field of Civil engineering.

Supervisors: Prof. Adnan Ibrahimbegović, PhD and Prof. Predrag Miščević, PhD

The committee for evaluation:

Prof. Ivica Kožar, PhD
Prof. Adnan Ibrahimbegović, PhD
Prof. Predrag Miščević, PhD
Prof. Hermann Matthies, PhD
Prof. Bernhard Schrefler, PhD

The defence committee:

Prof. Hermann Matthies, PhD

Prof. Adnan Ibrahimbegović, PhD

Prof. Predrag Miščević, PhD

Prof. Bernhard Schrefler, PhD

Prof. Ivica Kožar, PhD

The doctoral dissertation has been defended on 28th September, 2015.

Secretary:

Saša Delić, LL.M.

This dissertation contains:

107 pages

56 figures

7 tables

98 references

Leonu

This thesis has been supported by the Faculty of Civil Engineering, Architecture and Geodesy of University of Split, scholarship of the French Government through the Campus France programme and by École Normale Supérieure de Cachan excellence scholarship for doctoral students. Additional support has been provided by Split-Dalmatia County (in each of the 3 academic years), Erasmus programme, Županijske ceste Split and Vodoprivreda Split. This support is gratefully acknowledged.

I would like to thank in particular all those who contributed to this thesis:

my 'french' supervisor, prof. Adnan Ibrahimbegović, who generously accepted me and who offered me all of his scientific knowledge which helped me to successfully finish this thesis and who was always at a disposal for assisting in many different situations like applications for scholarships or accommodation, and in whose home, for the first time upon arriving to France, I ate a 'wholesome' meal (thanks are here also to his wife Nita)

my 'croatian' supervisor, prof. Predrag Miščević, who offered me his knowledge and continuous support from the very beginning of the thesis

reviewers of this thesis and also members of the committee for evaluation of the thesis, prof. Ivica Kožar, prof. Bernhard Schrefler, prof. Hermann Matthies, for their participation, useful comments and remarks

the members of the Geotechnical department, especially prof. Tanja Roje-Bonacci, who supported me joining the department and who was always encouraging my scientific work, and doc.dr.sc. Nataša Štambuk-Cvitanović, with who I realized a great collaboration

the former and the present dean of the Faculty of Civil Engineering, Architecture and Geodesy in Split, prof. Alen Harapin and prof. Boris Trogrlić, who were very supportive towards this thesis

Last but not the least, I thank to Svjetlana, who was raising our son during my stay in France, and my parents and sister, for their continuous support

UDC 624.121.5:531.3]:519.6](043.3)

Rock mechanics, failure phenomena with pre-existing cracks and internal fluid flow through cracks

Mijo Nikolić

Abstract

This thesis deals with the problem of localized failure in rocks, which occurs often in civil engineering practice like in dam failure, foundation collapse, stability of excavations, slopes and tunnels, landslides and rock falls. The risk of localized failure should be better understood in order to be prevented. The localized failure in rocks is usually characterized by a sudden and brittle failure without warning in a sense of larger and visible deformations prior to failure. This happens also under the strong influence of material heterogeneities, pre-existing cracks and other defects.

The three novel numerical models, incorporating the localized failure mechanisms, heterogeneity of rock and pre-existing cracks and other defects, are presented in this thesis. First model deals with 2D plane strain two-phase rock composite, where stronger phase represents the intact rock and weaker phase initial defects. Second model represents the extension of the previous model towards the 3D space, where full set of 3D failure mechanisms is considered. Heterogeneous properties are taken here through the random distribution and Gauss statistical variation of material properties. The latter model is also used for the analysis of intact rock core specimens geometrical shape deviations influencing the uniaxial compressive strength. Third model is a 2D, dealing with volumetric fluid-structure interaction and localized failure under the influence of fluid flow through the porous rock medium.

The discrete beam lattice approach is chosen for general framework for three models, where Voronoi cells represent the rock grains kept together by Timoshenko beams as cohesive links. The enhanced kinematics characterized for embedded discontinuity approach is added upon standard kinematics of cohesive links. This serves for the macro-crack propagation in all failure modes and their combinations, between the rock grains. The fracture process zone formation followed by micro-cracks coalescence, preceding the localized failure, is considered as well. Fluid flow is governed by a Darcy law, while coupling conditions obey Biot's theory of poroplasticity.

The results of the numerical models were verified by the benchmarks available from literature in 2D case. The 3D model was validated against the experimental results conducted on 90 rock specimens, where even slight geometrical deviations of specimens are considered.

Presentation of these models, as well as their implementation aspects are given in full detail. Embedded discontinuity concept and the local nature of enhancements required to capture the displacement discontinuities leads to the very efficient approach with static condensation of enhanced degrees of freedom and technique that can be efficiently incorporated into finite element code architecture.

UDK 624.121.5:531.3]:519.6](043.3)

Mehanika stijena, fenomen loma s postojećim pukotinama i unutrašnjim protokom fluida kroz pukotine

Mijo Nikolić

Sažetak

Ova doktorska disertacija bavi se problemom lokaliziranog sloma u stijenama koji se često pojavljuje u različitima zadaćama u inženjerskoj praksi kod otkazivanja nosivosti brana, sloma temelja, stabilnosti iskopa, klizišta i tunela ili stijenskih odrona. Bolje razumijevanje ovog fenomena je nužno zbog prevencije rizika od lokaliziranog sloma. Lokalizirani slom u stijenama karakteriziran je iznenadnim i krtim slomom bez upozorenja u obliku velikih i vidljivih deformacija, a uvjetovan je materijalnim heterogenostima, postojećim pukotinama i oslabljenjima.

U ovome radu prezentirana su tri nova numerička modela koja uključuju mehanizme lokaliziranog sloma, materijalnu heterogenost stijene s postojećim pukotinama i drugim oslabljenjima. Prvi je 2D model za analizu ravninskog stanja deformacija dvofazne kompozitne stijene, kod koje čvršća faza predstavlja intaktnu stijenu, a slabija faza početne nepravilnosti (oslabljenja) u stijeni. Drugi model predstavlja proširenje opisanog 2D modela u 3D područje, gdje su uključeni 3D mehanizmi sloma. Heterogenost je uzeta u obzir pomoću slučajne raspodjele i Gaussove statističke varijacije materijalnih karakteristika. Ovaj model je upotrijebljen u analizi utjecaja geometrijskih nepravilnosti oblika stijenskih uzoraka na jednoosnu tlačnu čvrstoću. Treći numerički model je dvodimenzionalni, a bavi se volumenskom interakcijom tekućine i konstrukcije i lokaliziranim slomom pod utjecajem protoka tekućine kroz poroznu stijensku sredinu.

Osnova sva tri numerička modela je pristup zasnovan na diskretnoj rešetkastoj mreži greda u kojem su Voronoi ćelije kao diskretne čestice stijene međusobno povezane kohezivnim vezama modeliranima pomoću Timoshenkovih greda. Poboljšana kinematika, karakteristična za metodu konačnih elemenata s ugrađenim diskontinuitetima, je dodana standardnoj kinematici kohezivnih veza što omogućuje nastanak i širenje makropukotina između mineralnih zrna stijene u svim mehanizmima sloma i njihovim kombinacijama. Proces nastanka mikropukotina koji prethodi lokaliziranom slomu stijene je također uzet u obzir u modelu. Protok tekućine definiran je Darcijevim zakonom dok je volumenska interakcija tekućine i stijene zasnovana na Biotovoj teoriji poroplastičnosti.

Rezultati razvijenih numeričkih 2D modela su verificirani na primjerima iz literature. Validacija 3D modela provedena je usporedbom s eksperimentalnim rezultatima dobivenima ispitivanjem 90 stijenskih uzoraka, gdje su razmatrane i geometrijske nepravilnosti stijenskih uzoraka. U ovoj doktorskoj disertaciji detaljno su prezentirani svi razvijeni numerički modeli, kao i njihova matematička i numerička implementacija. Pristup s ugrađenim diskontinuitetima i lokalnim poboljšanjima za simulaciju diskontinuiteta u polja pomaka te statičkom kondenzacijom dodatnih stupnjeva slobode je na vrlo efikasan način ugrađen u program za analizu konstrukcija metodom konačnih elemenata.

UDC 624.121.5:531.3]:519.6](043.3)

Mécanique des roches, phénomènes de rupture avec la prise en compte des fissures existantes et l'écoulement du fluide interne à travers les fissures

Mijo Nikolić

Resumé

Cette thèse aborde le problème de la rupture localisée dans les roches, qui charcterise un grand nombre d'applications dans le domaine du génie civil, tels que la rupture du barrage, effondrement desfondations, la stabilité des excavations ou les tunnels, les glissements de terrain et éboulements. Le risque de rupture localisée devrait être mieux apprehendé pour mieux l'évitér. La rupture localisée dans les roches est généralement caractérisé par une une rupture soudaine et quasi-fragile sans avertissement dans un sens de plus grandes déformations et visibles avant l'échec. Cela se produit également sous l'influence des hétérogénéités matériels, influencé par des fissures existantes et d'autres défauts initaux.

Les trois nouveaux modèles numériques, intégrant les mécanismes de rupture localisées, l'hétérogénéité de la roche et de fissures existantes et d'autres défauts, sont présentés dans cette thèse. Premier modèle propose une représentation 2D de roche composite à deux phases, où la phase solide représente la roche intacte et les plus faibles en phase défauts initiaux. Deuxième modèle représente l'extension du modèle précédent vers l'espace 3D, où un ensemble complet de mécanismes de défaillance 3D est considéré. Propriétés hétérogènes sont prises ici par la distribution aléatoire en accord avec la variation statistique Gaussienne des propriétés des matériaux. Ce dernier modèle est également utilisé pour l'analyse de la roche intacte spécimens écarts de forme géométriques qui influencent la résistance à la compression uniaxiale. Troisième modèle est un modèle 2D, traitant interaction volumétrique entre fluide et structure et la rupture localisée sous l'influence de l'écoulement du fluide à travers le milieu de la roche poreuse.

L'approche de lattice discret est choisi pour construire le cadre général pour trois modèles, où les cellules de Voronoi représentent les grains de roche gardés ensemble par Timoshenko poutres que des liens de cohésion. La cinématique améliorées caractérisées pour l'approche intégrée de discontinuité est ajouté sur la cinématique standard de liens cohérents. Cela sert pour la propagation de la fissure macro dans tous les modes de défaillance et de leurs combinaisons, entre les grains de la roche. La formation de la zone de processus de rupture suivie par des micro-fissures coalescence, précédant la rupture localisée, est considéré comme bien. Écoulement de fluide est régie par une loi de Darcy, tandis que les conditions de couplage obéissent à la théorie de Biot de poroélasticité.

Les résultats des modèles numériques ont été vérifiées par les repères de la littérature dans le cas 2D. Le modèle 3D a été validé contre les résultats expérimentaux effectués

sur 90 échantillons de roches, où de légères déviations géométriques de spécimens sont considérés.

Présentation de ces modèles, ainsi que leurs aspects de mise en œuvre sont présentés en détail. Notion de discontinuité intrinsèque et le caractère local des améliorations nécessaires pour capturer les discontinuités de déplacement conduit à l'approche très efficace avec condensation statique des degrés améliorés de liberté et de technique qui peut être efficacement intégrés dans architecture standarde d'un logiciel élément finis.

Contents

List of Figures

List of Tables

Chapter 1

Introduction

Contents

Figure 1.1: Rock falls hitting the coastal roads: Omiš, April 2012.; Omiš, April 2012.; Krilo Jesenice, March 2010.

1 Motivation

Rock material is a natural geological material consisting of different minerals. It is discontinuous, anisotropic, inhomogeneous, inelastic and contains numerous randomly oriented zones of initiation of potential failure, like initial joints, defects, cavities or other natural flaws. Rocks have been used from the early beginnings of the human race in many different ways especially for the building purposes. We were constantly facing its unpredictable nature trying to build roads, tunnels, underground excavations, mining shafts or avoid the sudden rock falls and sliding of slopes. From the early days there was a need for predicting the behaviour of this material and up to present times, we are still trying to fully understand it.

In the Croatian coastal and other karst areas, there is a pressing problem of massive rock fall occurrence that threatens the roads and inhabited places. The intensity of rock falls increases significantly after the heavy rains, requiring mostly additional financial investment into maintenance and reconstruction of roads. Namely, the main Adriatic road is hit by a large amount of rock falls every year, while some road sections like Split-Omiš and Vrgorac-Makarska are closed at least once per year (Figure 1.1).

On the other hand, many inhabited places are endangered as well. Omiš is the most populated city on the Croatian coast which is under the direct danger of rock falls, where even city centre lies beneath the huge rock blocks (Figure 1.2).

Many private houses in Omiš are also under close range of potential rock falls, while some of them have already been hit (Figure 1.3). There is a need to tackle these problems in order to reduce the damage, and most importantly, to avoid the loss of human lives.

Localized failure, usually sudden and unpredictable, represents the main failure mechanism of these rock blocks. It occurs also in many other engineering failure occasions like foundation collapse, stability of excavations, slopes and tunnels, landslides and rock falls, to mention only a few. The risk of localized failure should be better understood in order to be prevented.

Because of the irregular nature of rock material, the prediction of its behaviour has always been a challenging task. Rock mechanics has been developed mostly for the design of rock engineering structures and today we have a wide spectrum of different modelling

Figure 1.2: Omiš city centre under the danger of potential rock falls

approaches for many various rock mechanics problems. That include the approaches based on the previous experiences, simplified mathematical models that can be solved analytically (e.g. Bishop method of slices for slope stability) or general classification systems for rocks that are based on empirical correlations for indirect estimates of rock deformation properties. The latter found large number of applications in various types of engineering projects like designing and construction of excavations in rock. The lack of information about rock properties is a common fact in rock mechanics and engineering design so empirical approaches (including the classification systems) are also widely used. There are couple of rock mass classification system including Rock Mass Rating (RMR), Geological Strength Index (GSI), Tunnelling Quality Index (Q) and Rock Mass Index (RMi) classifications which are used to estimate the rock mass properties.

The development of computers made a significant contribution to the computational mechanics which found its wide use in rock mechanics. Namely, the numerical methods for solving the partial differential equations are used today as the main approach in engineering design and research of rock mechanics. These methods have tried to simulate such a complex behaviour of this natural and unpredictable material and were constantly evolving since their beginnings which occurred in the early 1960s. Today, the simulations stand as significant tool for obtaining more insight into the full control of rock behaviour. Next section provides the overview of the numerical methods used for simulating the rock behaviour.

Figure 1.3: Severe damage of houses is caused by rock falls: Omiš, January 2012.

2 Overview of the numerical methods applied to rock mechanics

The numerical methods can be classified into three main categories: continuum, discontinuum and hybrid continuum/discontinuum methods. Namely, the continuum concept implies that the domain of interest cannot be separated and the continuity between the points / elements must be preserved in order to establish the derivatives. Contrary to the analytical solution of differential equations where the solution is known in each point, the numerical solution is calculated in the finite number of pre-defined nodes which reduces the system complexity. The discontinuum approach on the other side threats the separate elements as discrete ones which are individually continuous and they mutually interact. In the discontinuous methods, the rigid body motion (usually with large movements) is the main case of interest, while in continuum-based methods the deformation of the system is the main objective. Thus, the sliding of the rock block on the pre-existing discontinuity would rather be computed with the discrete methods, while the choice of continuum method would better serve in calculating the deformation of the rock mass above the excavation of the tunnel. In addition there also exist the hybrid continuum/discontinuum methods that use the best properties of both approaches. Such an example is to have the discrete rock block which moves and also deforms under the external loading.

The most notable continuum numerical methods are Finite Difference Method (FDM), Finite Volume Method (FVM), Finite Element Method (FEM), Meshless Methods and Boundary Element Method (BEM). The discontinuum methods are Discrete Element Method (DEM) and Discrete Fracture Network (DFN). The most notable hybrid continuum/discontinuum methods with applications in rock mechanics are Discrete Finite Element Method and Combined Finite Discrete Element Method (Table 1.1).

2.1 Finite Difference and Finite Volume Method (FDM, FVM)

The Finite Difference Method (FDM) is one of the oldest widely-applied numerical methods for solving the partial differential equations that found its application in the rock

Table 1.1: Overview of the most notable numerical methods

Continuum methods:
Finite Difference Method **FDM**
Finite Volume Method **FVM**
Finite Element Method **FEM**
Meshless Methods
Boundary Element Methods **BEM**
Discontinuum Methods:
Discrete Element Method **DEM**
Discrete Fracture Network Method **DFN**
Hybrid Methods:
Discrete Finite Element Method
Combined Finite Discrete Element Method **FEM/DEM**

mechanics field. The general principle of the method is replacing the partial derivatives of the function by the finite differences defined over the certain interval in the coordinate directions. More precisely, the domain needs to be partitioned into grid of nodes, among which the finite differences are defined. It's worth noting that the FDM can be used for solving the time dependent problems.

As a result of meshing the domain, a system of algebraic equations with unknowns related to the pre-defined nodes will arise. Each algebraic equation connected to its corresponding grid node is expressed as combination of function values at its own node, as well as at the surrounding nodes. After introducing the boundary conditions, the system of algebraic equations is finally solved (usually by direct or iterative methods) which produces the values of unknowns at each node leading to the approximate solution of the partial differential equation with an error made because of the difference in partial derivatives and finite differences. Such a direct kind of discretization, together with no practical need to use interpolation functions as in other methods like FEM or BEM, position this method as the most direct and intuitive technique for solving the partial differential equations. The advantage of the method is also in possibility of the simulation of complex nonlinear material behaviour without iterative solutions.

The standard FDM uses regular grids, such as rectangular which is also the most important shortcoming of the method. Thus, representing the irregular geometries together with dealing with heterogeneous nature of rocks and complex boundary conditions seems like a significant disadvantage of this method for simulating rock behaviour in practical rock mechanics tasks. Another important disadvantage lies in continuity requirement of the proposed equations which is not suitable for dealing with fractures. However, the general FDM method [Perrone and Kao, 1975, Brighi et al., 1998] evolved eventually to deal with this shortcomings, mostly with irregular grids, which include irregular quadrilateral, triangular and Voronoi grids.

The further development of this approach continued with the Finite Volume Method (FVM) [Wheel, 1996]. The FVM is also a method for solving the partial differential

equations, not directly as in FDM, but in integral sense. The method is based on the formulation of finite volumes, which represent the volume surrounding each node in mesh. The basic principle is to replace the integrals with algebraic functions of the unknowns in the nodes, taking into account the initial and boundary conditions which lead to the set of algebraic equations.

The main advantages of the FVM are the possibilities of using the irregular unstructured meshes such as arbitrary triangles, quadrilaterals or Voronoi cells and considering the material heterogeneities [Fallah et al., 2000]. The continuity requirement between the neighbouring nodes still makes the fracture propagation impossible to include, which is a main disadvantage of FDM/FVM. The analysis of the fracturing processes in FDM/FVM models can be conducted through the material failure at the nodes or cell centres, but in this way it is not possible to simulate the true fracture propagation. Despite this lacking, the FVM is still one of the most popular numerical methods in rock mechanics with applications in slope stability, tectonic process, rock mass characterization and especially in coupled hydro-mechanical problems. The latest improvements of the FDM/FVM can be seen in [Benito et al., 2001, Onate et al., 1994, Lahrmann, 1992, Jasak and Weller, 2000].

2.2 Finite Element Method (FEM)

The Finite Element Method (FEM) originates from the early 1960s and the works of [Clough, 1960, Argyris, 1960]. It was developed as an alternative to the finite difference method for the numerical solution of stress concentration in continuum mechanics and was the first numerical method which was able to account for material heterogeneities, non-linearities, complex geometries and boundary conditions. Due to this, FEM immediately became the most applied numerical method in rock mechanics, especially because the FDM at that time was limited only to regular grids. The rapid application of the method started in the late 1970s and early 1980s when many rock mechanics problems at that time were solved with FEM [Naylor et al., 1981]. The FEM was evolving fast during the years, and today it is still the most applied numerical method for many advanced rock and soil mechanics simulations of the non-linear, time-dependent and anisotropic behaviour.

The general principle of FEM is to divide the domain of the problem into smaller sub-domains called finite elements, do the local approximation inside each finite element, perform the finite element assembly and find the solution of the global matrix equation. More precisely, the unknown function (usually displacement function) needs to be approximated with a trial functions of the nodal values in a polynomial form, where the numerical integration is performed in each element in Gaussian quadrature points. After the finite element assembly is performed, the algebraic system of equations on a global level is obtained. One of the mostly used advantages of FEM is a possibility of representing heterogeneous rocks, where it is possible to assign the different material properties to different finite elements. Presently, there are many various shapes of finite elements with different number of nodes for 1D, 2D and 3D cases. Special case of elements called the 'infinite elements' was developed to simulate the far-field domain in geotechnical applic-

ations [Zienkiewicz et al., 1983].

Because of the continuum assumptions, the FEM method has restrictions in efficient application of the failure analysis, cracking and damage induced discontinuities or singularities [Ibrahimbegovic, 2009]. Since rock is a discontinuous material and FEM is a continuum method, there have been many attempts to improve it in order to simulate the fracture propagation and other discontinuous effects with it. From the early experiments on rock specimens, it was observed that the experimentally obtained stress-strain curves up to failure are not linear. One of the earliest models that could approximately simulate the stress-strain nonlinear curve due to crack opening was smeared-crack model. This model was perfectly brittle in the beginning, although the rock has some residual load-carrying capacity after reaching its strength resulting with softening behaviour. Another attempt was an indirect representation of the discontinuities with the 'joint' elements where their influence on physical behaviour is considered through constitutive laws of the discontinuities as equivalent continuum. However, no real detachment is possible with them. The 'joint' elements are also limited to small displacements, while large movements across the discontinuities (e.g. sliding on the discontinuities) are not possible due to the continuum assumptions. The first element of this kind was 'Goodman joint element' developed especially for rock applications [Goodman et al., 1968].

The ultimate load computation where structural elements are subjected to progressive failure which leads to the collapse of the structure has been the topic of interest of many authors recently since this is one of the crucial types of failure mechanisms. The key difficulty in failure analysis is correct and mesh-independent representation of the post-peak softening behaviour related to crack propagation. Also, when trying to simulate the fracture growth with FEM, it is essential to have small size of elements and perform the continuous re-meshing as the crack propagates. The 'enhanced' FEM methods have been evolving to overcome the re-meshing, which resulted with couple of new methods. On one side there is the finite element method with embedded discontinuities (ED-FEM), representing cracks truly in each element [Simo et al., 1993, Simo and Rifai, 1990, Ibrahimbegovic and Wilson, 1991, da Costa et al., 2009]. On the other side there is extended finite element method (X-FEM) where cracks are represented globally [Moes et al., 1999, Fries and Belytschko, 2006, Fries and Belytschko, 2010]. The ED-FEM and X-FEM methods are equivalent in their capabilities to handle the most demanding kinematics incorporating both strong and weak discontinuities. The strong discontinuities serve for truly simulating the crack propagation, while the weak discontinuities enable the heterogeneous representation of material within element. The general approach is to enhance the standard kinematics of the finite elements with additional discontinuous functions to simulate discontinuous behaviour. Thus, the enhanced kinematics in the strain and displacement fields serve respectively for dealing with heterogeneities and localization phenomena. The most recent contribution to ED-FEM approach in rock mechanics was made in the following works [Saksala, 2014, Saksala et al., 2015] where the crack propagation due to failure modes I,II, as well as their combination, provide successful simulation of complex failure mechanisms that occur in rocks. This kind of representation is also suitable for connecting the scales where the natural crack growth

from the micro to macro cracks can be simulated. Namely, the cracks form as a result of accumulation of micro-cracks leading to forming larger macro-cracks. Another example of enhanced finite elements is a Generalized Finite Element Method (G-FEM) [Strouboulis et al., 2000, Strouboulis et al., 2001]. The G-FEM uses the local functions which are usually analytical solutions to specific problems. These additional functions are not necessarily polynomials, but are bonded together with the standard space through the partition of unity principle.

Apart FEM being suitable for representing heterogeneous materials and using the unstructured and irregular meshes, it also proved to be the appropriate tool for representing various non-linear and inelastic types of behaviour. These observations carried the challenges up to present time and many different models have been made for representation of material hardening and softening macro responses. Among them, damage and plasticity models, are the most used frameworks for simulation of the non-linear and inelastic behaviour of material [Lemaitre and Chaboche, 1994]. The FEM is also suitable for representing the geometric non-linearities, contact mechanisms, fluid-structure interaction, multi-scale problems, etc. All of these reasons position the FEM as the mostly used numerical method applied in rock mechanics.

2.3 Meshless methods

The application of the FEM in practical engineering problems with complex geometries, material properties and boundary conditions requires mesh generation which sometimes, especially in 3D problems, can be equally as demanding as solving the problem. Another problem can occur as a results of large mesh distortions. The both of these problems can be avoided by meshless methods which developed in a way that elements connecting the nodes are not required. Instead, the trial functions are generated from the neighbouring nodes within a domain of influence. More precisely, it is only necessary to generate the nodes across the domain without defining fixed element topology. Many meshless methods have been developed, but some of the mostly used ones are: Smoothed particle hydrodynamics, Diffuse element method, Element-free Galerkin method, Reproducing kernel particle methods, Moving least-squares reproducing kernel method, hp-cloud method, the method of finite spheres, Finite point method etc. Overview and the implementation aspects of the meshless methods can be found in [Nguyen et al., 2008, Belytschko et al., 1996]

2.4 Boundary Element Method (BEM)

The basic principle of BEM is to fit boundary values into the integral equation. Thus the discretization is needed only at the boundary with a finite number of boundary elements. After finding the solution on a boundary, the interpolation can be used for calculating the solutions inside the domain. The main advantage of the BEM is reduction of model dimensions by 1. The approximation of the solution at the boundary elements is performed using the shape functions similarly to FEM. When applying the boundary conditions into

the matrix equations obtained after the approximation stage, the final global matrix equation with unknowns at boundary is obtained.

The BEM has its origins in the early 1980s [Crouch and Starfield, 1983]. This method has found applications in underground excavations, dynamic rock problems, analysis of in situ stress and borehole drilling. Besides reducing the model dimensions by 1, its strength is accuracy in finding the solution because of its direct integral formulation. The standard BEM was developed for continuous and linear elastic solutions inside domain which was a disadvantage of the method in the beginning. The other main disadvantage over FEM is not efficient dealing with heterogeneity because not complete domain is discretized with elements. The fracture propagation with BEM was simulated in the works of [Blandford et al., 1981, Mi and Aliabadi, 1992], using domain subdivision into subdomains or by Dual BEM. The notable variants of BEM are also Galerkin BEM (GBEM) [Bonnet et al., 1998] and Dual-reciprocity BEM (DRBEM) [Kontoni, 1992].

2.5 Discrete Element Method (DEM)

The DEM started to develop in the field of the rock mechanics applications due to its requirements for the modelling of discontinuous behaviour [Cundall, 1971]. The method was primarily defined as the computational approach that can simulate finite displacements and rotations of discrete bodies including their detachment. The theoretical formulations are based upon the equations of motion of rigid or deformable bodies. The basic concept is to threat the domain of interest as an assembly of particles or blocks which are continuously interacting between each other. In the DEM approach, the contact between components of the system is constantly changing during the deformation process.

The constant evolution of DEM led to many different numerical approaches developed for various rock mechanics problems. The main strength of the approach was the fact that the real discontinuities could be simulated, as well as representing the rock blocks which moves and interacts between each other including the fragmentation process etc. All of DEM based methods have the similar basic approach, while the difference between them are the use of various shapes of discrete elements, the way of computing the contact forces between the discrete bodies, the way of recognizing the contact, the way of integration of equations of motion, etc. The contact between the discrete bodies is essential part of solving the task. The overview of the contact models can be found in [Wriggers, 2006].

The two main approaches of DEM exist according to the numerical integration scheme that can be explicit or implicit. The application of the explicit DEM started in the 1970s and was used mostly for rigid block simulations. The most representative explicit DEM method is Distinct Element Method developed by Cundall [Cundall, 1988]. It was created to simulate the fracturing, cracking and splitting of the blocks under external loading. The method was applied in many various rock mechanic applications including tunnelling, underground works and rock dynamics, nuclear waste disposal, rock slopes, acoustic emission in rock, boreholes, laboratory test simulations etc.

The most well-known method of implicit DEM approach is Discontinuous Deformation Analysis (DDA) [Shi, 1992]. It is similar to the finite element method for solving

deformation of the bodies, but it also accounts for interaction of the independent blocks along discontinuities in fractured and jointed rock mass. The interaction between the independent blocks is performed by contact algorithms. It is an attractive method for solving rock mechanics problems where the rock blocks interact and deform between each other.

Besides using the block systems in rock mechanics, the particle based DEM is an appropriate method for simulating the granular materials such as soil. The principle of solving tasks with granular materials is the same as for blocks, but with the simpler contact mechanisms due to rigid regular or irregular particles that do not deform. The regular particles include circular, elliptical and ellipsoidal shapes, while irregular ones can be polygonal or polyhedral. Some of the applications of particle based DEM in rock mechanics are rock fracturing and fragmentation due to rock blasting, tunnelling, hydraulic fracturing.

Another approach similar to DEM is the Discrete lattice network methods used to simulate rock fracture initiation and propagation [Ostoja-Starzewski, 2002]. The general idea is to have rigid particles covering the domain of interest, with springs acting as cohesive links and connecting the particles. The springs usually do not possess the mass and have the characteristic stiffness properties of material. The mass of the particles depend on the density of the material. During the simulation process, the springs deform until they are completely broken leaving the particles to move and interact with other particles. When the cracks propagate through the domain, cohesive links are usually removed and remeshing is performed to simulate the evolving discontinuities.

2.6 Discrete Fracture Network (DFN)

The DFN is a discrete model for simulating fluid flow and transport processes through the connected fractures [Tsang and Tsang, 1987, Cacas et al., 1990]. DFN also makes consistent use of a wide variety of disparate geological, geophysical and production data to generate the system of fractures, where latter are modelled through the combination of deterministic and stochastic models. A DFN model can be used for simulating the rock mass properties and large scale rock problems.

2.7 Hybrid methods

Many numerical methods that combine advantages of finite and discrete elements developed. One of the well-known methods which combine finite and discrete elements is Discrete Finite Element Method [Ghaboussi, 1988]. The main advantage of the method is a possibility to simulate interaction between the blocks, as well as the deformation of blocks. The higher order shape functions are used here for considering non-linear deforming of the blocks. The method uses implicit time integration and it is similar to Discontinuous Deformation Analysis (DDA). Another hybrid approach is Combined Finite Discrete Element Method (FEM/DEM) [Munjiza et al., 1995] which considers block deformation as well as the fragmentation processes. Contrary to Discrete Finite Element Method, the FEM/DEM uses explicit time integration scheme. The FEM/DEM method is

used in rock mechanics applications [Mahabadi et al., 2012] and stone blocks interactions [Smoljanovic et al., 2013]. There were some developments of the method considering the reinforcement between discrete elements with application in concrete, but which can be easily used to simulate the rock slopes or tunnel excavations with anchor reinforcements [Zivaljic et al., 2013].

3 Aims, scopes and methodology

The main scientific goal of this thesis is to provide the enhanced predictive models for localized failure in rock mechanics, by taking into account material heterogeneities and pre-existing defects. Localized failure represents the typical type of rock failure where full set of failure modes is needed: modes I and II in 2D setting and modes I, II and III in 3D setting. Mode I stands for tensile opening leading to development of macro-cracks, while modes II and III represent shear sliding along the cracks. However, the true rock failure consists of two dissipative mechanisms: fracture process zone with micro-cracks and localized failure mechanism with macro-cracks. The aim of the thesis is to combine these two mechanisms within the single model, which depends on fine scale heterogeneities. The novel approach is proposed here, by considering the rock material as a assembly of grains held together by cohesive forces. For this purpose, the discrete lattice model approach is chosen for rock representation, while cohesive links are enhanced with additional discontinuous properties. Such an enhancement is enabled through the embedded discontinuity framework (ED-FEM).

Another goal pertains to understanding the role of the fluid-flow to the development of micro-cracks and macro-cracks during the localized failure process. This leads to a complex multiphysics problem of volumetric fluid structure-interaction where all of the ingredients of the rock mechanics model need to be combined with micro-porosity of rock which allows for flow through the porous medium.

4 Outline

The outline of this thesis is as follows. Chapter 2 provides the full development and numerical examples of the novel discrete 2D rock mechanics model. In Chapter 3, the novel 3D model is presented, together with the numericaly obtained results that are compared to experimental ones. Numerical part of the research study on the role of rock specimen shape deviations on uniaxial compressive strength is given in Chapter 4. Chapter 5 brings the novel 2D model for simulating the failure of rocks under the influence of fluid flow through the porous medium. Finally, the conclusion summarizes all the main findings of the thesis and suggests the future perspective of the study on this topic, in Chapter 6.

Chapter 2

2D rock mechanics model: embedded discontinuity approach for representing mode I and mode II failure mechanisms

In this chapter, a discrete beam lattice model with embedded discontinuities capable of simulating rock failure as a result of propagating cracks through rock material is presented. The developed model is a 2D (plane strain) micro-scale representation of rocks as a two-phase heterogeneous material. Phase I is chosen for intact rock part, while phase II stands for pre-existing micro-cracks and other defects. The proposed model relies on Timoshenko beam elements enhanced with additional kinematics to describe localized failure mechanisms. The model can properly take into account the fracture process zone with pre-existing micro-cracks coalescence, along with localized failure modes, mode I of tensile opening and mode II of shear sliding. A novel numerical procedure for dealing with two modes failure within framework of method of incompatible modes is presented in detail and validated by a set of numerical examples.

Contents

1 Model description

Rock material is a highly heterogeneous material that contains numerous randomly oriented zones of initiation of potential failure. These zones can be various kinds of initial flaws, cracks, cavities, pores or other defects inside the rock. Not all defects exist from the beginning of loading. When a heterogeneous material is loaded, the new cracks initiate from existing defects, start to propagate and tend to form into larger macro-cracks. This processes of accumulation of cracks leads to complete failure, which is usually a brittle type failure characterized for large number of rock types. In this chapter, the first goal is to deal with the crack propagation, the main mechanism of brittle failure of rocks in 2D plane. The answer for second goal of representing a more ductile failure of rocks due to frictional sliding of cracks is provided as well.

Proper modelling of rock material behaviour thus demands different approach than continuum approach used in usual engineering tasks, where Finite Element Method (FEM) has been considered as the main tool for solving vast majority of applications [Zienkiewicz and Taylor, 2000, Bathe, 2006, Ibrahimbegovic, 2009]. In order to provide a reliable predictive model for failure of rock material, the discontinuous solutions should be found, where pre-existing cracks continue to form into new ones during the increased loading leading to failure. The evolution of crack patterns shows that localization is a key factor inducing brittle failure. Thus, the main challenge tackled here was to provide enhanced predictive models for localized failure by taking into account the material heterogeneities and pre-existing cracks. As already elaborated in overview of the numerical methods of Introduction, some enhanced methods derived from the standard framework of Finite Element Method (FEM) to deal with localization, i.e. cracks, discontinuities. The first one is the Finite Element Method with Embedded Discontinuities (ED-FEM), representing cracks truly in each element (e.g. see [Simo et al., 1993, Simo and Rifai, 1990, Ortiz et al., 1987]). The second one is Extended Finite Element Method (X-FEM) where cracks are represented globally [Moes et al., 1999, Fries and Belytschko, 2006], [Fries and Belytschko, 2010].

The experiments show that there are two main failure modes that forces a crack propagation [Stagg and Zienkiewicz, 1968]:

-Mode I - crack opening mode is related to tension where the crack propagates perpendicularly to the direction of loading

-Mode II - crack sliding mode is related to shear where the crack propagates parallel to the crack plane

Very active research on localized failure [Ibrahimbegovic, 2009] has led to currently dominant approach in representing localized failure by introducing strong discontinuities or discontinuities in displacement field [Ibrahimbegovic and Markovic, 2003], [Ibrahimbegovic and Melnyk, 2007]. However, most of these works are limited to single failure mechanism concentrated on mode I crack propagation [Benkemoun et al., 2010, Benkemoun et al., 2012]. For the purpose of rock mechanics, it is essential to have both mode I and mode II failure mechanisms. The novelty in presented model is also a possib-

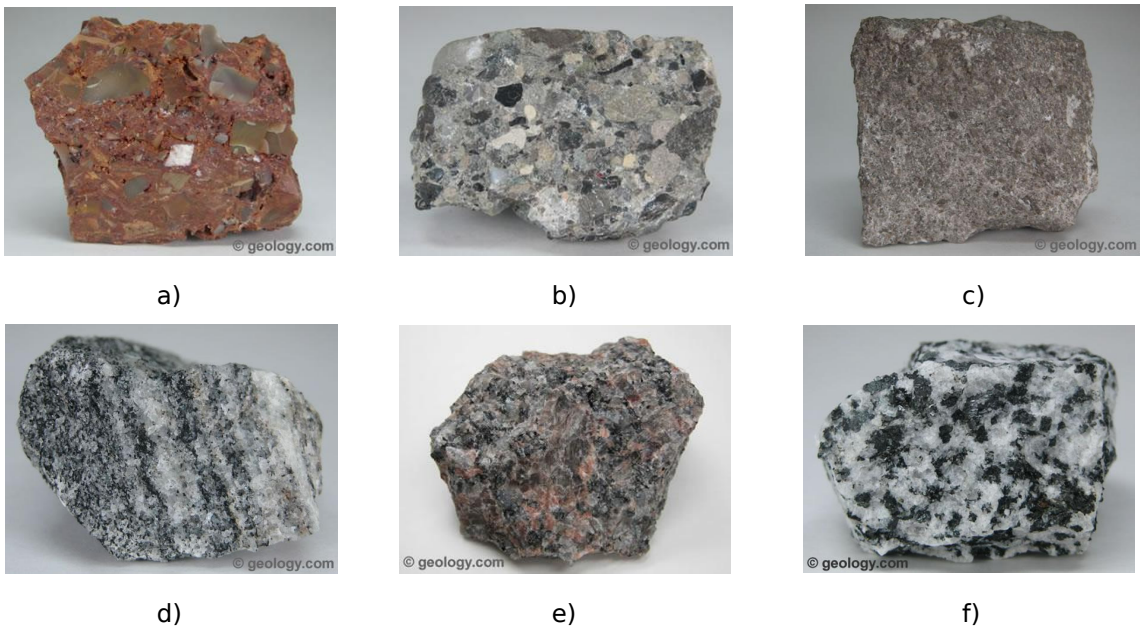

Figure 2.1: Grainy structure of different rocks: a) breccia (sedimentary), b) conglomerate (sedimentary), c) limestone (sedimentary), d) gneiss (metamorphic), e) granite (igneous), f) quartz-diorite (igneous). The size of all of the samples is approximately 5 cm. The photographs are taken from *http://geology.com/rocks/*

ility to handle these modes both simultaneously and separately.

This chapter presents a novel 2D plane strain model for the localized failure in rocks under the influence of heterogeneities and pre-existing defects also presented in [Nikolic et al., 2015a]. The class of discrete lattice models have been chosen here for general framework of the model. As elaborated in Introduction, such lattice models have been previously used in simulating the progressive failure of concrete and rocks, like shown in [Chang et al., 2002, Ostoja-Starzewski, 2002]. Namely, the basis of this framework is in representation of heterogeneous material which is considered as assembly of grains of material held together by cohesive links. This framework corresponds also to the geological formation of rocks, where many different groups of rocks possess a grainy structure which allows the grain recognition even with the bare eye (Figure 2.1). Here, the rock domain is discretized with the Voronoi cells as rock grains, where Timoshenko beams act as cohesive links between them (Figure 2.2). Several papers developed discrete lattice models, where the domain is discretized with the Voronoi cells: [Vassaux et al., 2015, Cusatis et al., 2006, Berton and Bolander, 2006].

Usually, the discrete lattice models simulate the progressive failure characterized by localization with re-meshing process [Karihaloo et al., 2003, Lilliu and van Mier, 2003, Liu et al., 2009]. Namely, the cohesive links are sequentially removed from the mesh when the discontinuity propagate between the grains. The main difference in the presented model, with respect to latter approach, concerns embedded discontinuities placed within the framework of ED-FEM, where Timoshenko beam elements are equipped with

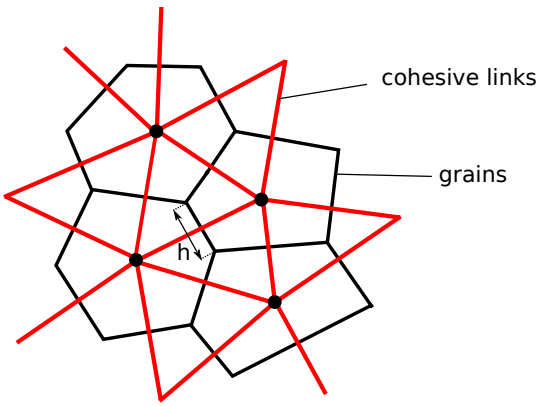

Figure 2.2: The basis of the proposed discrete model relies on the lattice of Timoshenko beams which represent the cohesive links keeping the rock grains (Voronoi cells) together.

enhanced kinematics capable of capturing the localization effects, like shown in [Pham et al., 2013, Jukic et al., 2013, Bui et al., 2014]. Namely, the embedded discontinuities are placed in the middle of each Timoshenko beam. This corresponds to the Voronoi cell network, where each cohesive link is cut by half by the edge between two neighbouring Voronoi cells. The embedded discontinuity in the longitudinal local direction enable the grain dilation due to mode I or tensile failure mode. However, Timoshenko beams also allow to account for pronounced shear effects in both elastic and plastic phase which is used here for representing the failure in mode II (shear sliding along the grains) adding the corresponding displacement or strong discontinuity in the transversal local direction. This leads to novel idea, where re-meshing is avoided, and localized solutions (i.e. discontinuity propagations) are enabled like shown in Figure 2.3. The latter approach is also used in the following chapters that enhanced this work towards 3D space and fluid-rock interaction, as the basis for the mechanics model of rocks.

Heterogeneities are considered here through two different phases representing the initial state of the specimen; the intact rock material and the initial weaker material that stands for pre-existing defects. The macroscopic response of the system is largely influenced by the distribution and position of the phases. The intact rock material, which is unlikely to fail, is represented by the Timoshenko cohesive links with linear elastic behaviour and no possibility of de-bonding. Thus, the discontinuity is not supposed to propagate through the intact. However, the weaker material is presented with the cohesive beam elements which are enhanced with additional kinematics, and also capable of handling localization through mode I and mode II, as explained above. Failure of the material can occur in both modes separately, as well as in their combination.

Discontinuity propagation is followed by softening phase if macro response is monitored. First possibility of the model is with separated softening, where modes are independent of each other, and plasticity-like softening is coupled together with fracture process zone represented by plasticity hardening, which precedes to localization. Second possibility implies the multisurface damage-like criterion where fracture limits in mode I

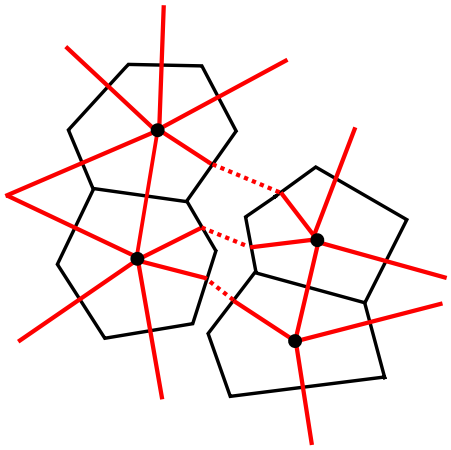

Figure 2.3: The strong discontinuity propagation between the Voronoi cells invokes the enhanced kinematics activation

and mode II are made so that the full stress reduction can be done simultaneously. The latter possibility is suitable for tension applied area of the rock material, while the first one accounts for compression applied areas, where most dominant failure is achieved through mode II and compression force may increase and influence the shear failure in Mohr-Coulomb way.

The softening is subjected to the problem of mesh dependency, when dealing with standard finite element formulations. The approach presented here is based upon Incompatible Mode Method [Simo and Rifai, 1990, Ibrahimbegovic and Wilson, 1991] and embedded discontinuities, leading to no mesh dependency when cracking occurs inside finite elements. Here, the fracture energy parameters play the key role defining the brittleness of the failure.

2 2D model formulation

The presented model is based on Timoshenko beam elements connecting the grains of material in terms of Voronoi cells. This section provides the enhanced formulation for Timoshenko beam, resulting with embedded discontinuities in local longitudinal direction for mode I failure, and in transversal direction for mode II failure. Two ways for dealing with failure modes are possible. First way is to handle these modes separately, where shear loading invokes mode II failure and at the same time compression force influences the shear failure threshold in terms of Mohr-Coulomb law. Second way is for dealing with tension, where simultaneous softening for both modes is enabled through the criteria presented at the end of this section. The developed model relies on thermodynamics principles. The localized failure is presented by a softening regime in a global macro-response, where the heterogeneous displacement field is used in order to obtain a mesh-independent response. The formulation for fracture process zone with micro-cracks is also presented here through the hardening regime with standard plasticity.

2.1 Enhanced kinematics

The localization implies heterogeneous displacement field which no longer remains regular, even for smooth stress field. Thus, the displacement field ought to be introduced and written as the sum of a sufficiently smooth, regular part and a discontinuous part. Furthermore, the axial and transversal displacement fields need to be calculated independently.

A straight finite element with two nodes of length l^e and cross section A is considered (Figure 2.4). The degrees of freedom at each node $i \in [1,2]$ are axial displacement u_i, transversal displacement v_i and rotation θ_i. The strain measures for standard Timoshenko element are given

$$\begin{aligned} \varepsilon(x) &= \frac{du(x)}{dx} \\ \gamma(x) &= \frac{dv(x)}{dx} - \theta(x) \\ \kappa(x) &= \frac{d\theta(x)}{dx}. \end{aligned} \tag{2.1}$$

For this element, standard linear interpolation functions are used for regular displacement approximation

$$\mathbf{N} = \left\{ N_1(x) = 1 - \frac{x}{l^e};\ N_2(x) = \frac{x}{l^e} \right\}. \tag{2.2}$$

The interpolation for standard beam displacements can thus be written as

$$\begin{aligned} u(x) &= \textstyle\sum_{a=1}^{2} N_a(x) u_a = \mathbf{N}\mathbf{u} \\ v(x) &= \textstyle\sum_{a=1}^{2} N_a(x) v_a = \mathbf{N}\mathbf{v} \\ \theta(x) &= \textstyle\sum_{a=1}^{2} N_a(x) \theta_a = \mathbf{N}\boldsymbol{\theta}, \end{aligned} \tag{2.3}$$

where $\mathbf{u}$, $\mathbf{v}$ and $\boldsymbol{\theta}$ represent nodal displacement vectors.

The discontinuous displacement fields need to be separated into regular and singular parts, where latter can be represented as a product of Heaviside function and displacement jump. The enhanced displacement fields can thus be written as

$$\begin{aligned} u(x) &= \overline{u}(x) + \alpha^{(u)} H_{x_c} \\ v(x) &= \overline{v}(x) + \alpha^{(v)} H_{x_c}, \end{aligned} \tag{2.4}$$

where $\alpha^{(u)}$ and $\alpha^{(v)}$ represent incompatible mode parameters which denote the displacement jumps in axial and transversal direction (Figure 2.4). H_{x_c} is the Heaviside function being equal to one if $x > x_c$, and zero otherwise, while x_c is the position of the discontinuity. The presented model assumes the position of discontinuity to be in the middle of the beam. This is the case when each cohesive link is cut in half by the two neighbouring Voronoi cells. Furthermore, the $N_2(x)$ is added and subtracted from previous equations (2.4), which leads to refined formulation of embedded discontinuity

$$\begin{aligned} u(x) &= \overline{u}(x) + \alpha^{(u)} N_2(x) + \alpha^{(u)} (H_{x_c} - N_2(x)) \\ v(x) &= \overline{v}(x) + \alpha^{(v)} N_2(x) + \alpha^{(v)} (H_{x_c} - N_2(x)), \end{aligned} \tag{2.5}$$

where second parts of these equations denote the discontinuity contribution. Namely, the additional interpolation function $M(x)$ is derived from (2.5) and can be used alongside

standard interpolation functions to describe the heterogeneous displacement fields with activated discontinuity jump producing embedded discontinuity inside the finite element. The $M(x)$ is defined as

$$M(x) = \begin{cases} -\frac{x}{l^e}; x \in [0, x_c\rangle \\ 1 - \frac{x}{l^e}; x \in \langle x_c, l^e] \end{cases} . \tag{2.6}$$

This kind of formulation cancels the contribution of incompatible mode parameter on the element boundary leading to possibility of computing the discontinuity parameters locally, while the global equations remain with the nodal displacements as primal unknowns.

The deformation fields in terms of regular and singular parts results from (2.4) with

$$\begin{aligned} \varepsilon(x) &= \overline{\varepsilon}(x) + \alpha^{(u)}\delta_{x_c} \\ \gamma(x) &= \overline{\gamma}(x) + \alpha^{(v)}\delta_{x_c}, \end{aligned} \tag{2.7}$$

where $\overline{\varepsilon}$ and $\overline{\gamma}$ denote regular parts, and Dirac delta δ_{x_c} is the singular part representation of the deformation field. The Dirac delta function δ_{x_c} takes an infinite value at $x = x_c$ and remains equal to zero everywhere else. The enhanced finite element displacement interpolations written in terms of embedded discontinuity

$$\begin{aligned} u(x) &= \textstyle\sum_{a=1}^{2} N_a(x)u_a + M(x)\alpha^{(u)} \\ v(x) &= \textstyle\sum_{a=1}^{2} N_a(x)v_a + M(x)\alpha^{(v)} \\ \theta(x) &= \textstyle\sum_{a=1}^{2} N_a(x)\theta_a. \end{aligned} \tag{2.8}$$

The discrete approximation of deformation field can be obtained from the above displacement field resulting with

$$\begin{aligned} \varepsilon(x) &= \textstyle\sum_{a=1}^{2} B_a(x)u_a + G(x)\alpha^{(u)} \\ \gamma(x) &= \textstyle\sum_{a=1}^{2} (B_a(x)v_a - N_a(x)\theta_a) + G(x)\alpha^{(v)} \\ \kappa(x) &= \textstyle\sum_{a=1}^{2} B_a(x)\theta_a, \end{aligned} \tag{2.9}$$

where $G(x)$ represents the derivative of enhanced function $M(x)$, with respect to local coordinate direction x

$$\begin{aligned} G(x) =& \overline{G} + \delta_{x_c} \\ =& -\frac{1}{l^e} + \delta_{x_c}, \;\; x \in [0, l^e]. \end{aligned} \tag{2.10}$$

The derivatives B of linear interpolation functions are

$$\mathbf{B} = \left\{ B_1(x) = -\frac{1}{l^e}; \;\; B_2(x) = \frac{1}{l^e} \right\}. \tag{2.11}$$

Finally, the complete set of generalized strains can be obtained

$$\boldsymbol{\varepsilon} = (\varepsilon, \gamma, \kappa)^T = \mathbf{B}\mathbf{d} + G\boldsymbol{\alpha}, \tag{2.12}$$

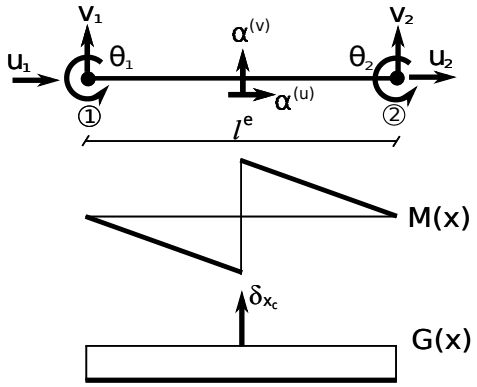

Figure 2.4: Timoshenko beam element with standard and enhanced d.o.f.; corresponding discontinuous shape functions

where

$$\mathbf{B} = \begin{bmatrix} B_1 & 0 & 0 & B_2 & 0 & 0 \\ 0 & B_1 & -N_1 & 0 & B_2 & -N_2 \\ 0 & 0 & B_1 & 0 & 0 & B_2 \end{bmatrix}, \ \mathbf{d} = (\mathbf{u}, \mathbf{v}, \boldsymbol{\theta})^T, \ \boldsymbol{\alpha} = (\alpha^{(u)}, \alpha^{(v)}, 0)^T. \tag{2.13}$$

The enhanced Timoshenko beam finite element, with its standard and enhanced degrees of freedom, is shown in Figure 2.4, along with the discontinuity functions M and G.

2.2 Equilibrium equations

The virtual deformations are interpolated in the same way as the real ones

$$\delta\boldsymbol{\varepsilon} = \mathbf{B}\delta\mathbf{d} + G\delta\boldsymbol{\alpha}, \tag{2.14}$$

with δ standing for prefix indicating the corresponding virtual field or variation. The virtual work of internal forces can be written as

$$\begin{aligned} G^{int} &= \int_0^{l^e} \delta\varepsilon N dx + \int_0^{l^e} \delta\gamma T dx + \int_0^{l^e} \delta\kappa M dx = \\ &= \int_0^{l^e} (\mathbf{B}\delta\mathbf{d})^T \boldsymbol{\sigma} dx + \int_0^{l^e} \delta\boldsymbol{\alpha}^T (\overline{G} + \delta_{x_c}) \boldsymbol{\sigma} dx, \end{aligned} \tag{2.15}$$

where

$$\delta\mathbf{d} = (\delta\mathbf{u}, \delta\mathbf{v}, \delta\boldsymbol{\theta})^T, \ \delta\boldsymbol{\alpha} = (\delta\alpha^{(u)}, \delta\alpha^{(v)}, 0)^T, \ \boldsymbol{\sigma} = (N, T, M)^T. \tag{2.16}$$

$\boldsymbol{\sigma}$ denotes the vector of beam stress resultants. The G^{int} is now separated into classical virtual work of internal forces and additional part that comes from the enhanced kinematics when discontinuity is activated. The internal force vector and the finite element residual vector due to discontinuity are given:

$$\begin{aligned} \mathbf{f}^{int} &= \textstyle\int_0^{l^e} \mathbf{B}^T \boldsymbol{\sigma} dx, \\ \mathbf{h}^{(e)} &= \textstyle\int_0^{l^e} (\overline{G} + \delta_{x_c}) \boldsymbol{\sigma} dx. \end{aligned} \tag{2.17}$$

From the condition of residual equation being equal to zero, the internal forces at the discontinuity ought to be calculated

$$\begin{aligned}\mathbf{h}^{(e)} &= \int_0^{l^e} (\overline{G} + \delta_{x_c})\boldsymbol{\sigma} dx = \\ &= \int_0^{l^e} \overline{G}\boldsymbol{\sigma} dx + \mathbf{t}.\end{aligned} \tag{2.18}$$

Vector $\mathbf{t}$ represents the internal forces at discontinuity, which are in relation with the forces from the bulk

$$\begin{aligned}\mathbf{t} = -\int_0^{l^e} \overline{G}\boldsymbol{\sigma} dx, \;\; \mathbf{t} = (t^{(u)}, t^{(v)}, 0)^T, \\ \mathbf{h}^{(e)} = (h_u^{(e)}, h_v^{(e)}, 0)^T.\end{aligned} \tag{2.19}$$

The enhanced finite element virtual work can be obtained from the previous equations as

$$G^{int} - G^{ext} = \delta\mathbf{d}^T(\mathbf{f}^{int} - \mathbf{f}^{ext}) + \delta\boldsymbol{\alpha}^T\mathbf{h}^{(e)}. \tag{2.20}$$

2.3 Constitutive model

The brittle rock failure has been a topic of many research studies [Bieniawski, 1967, Wawersik and Fairhurst, 1970, Lajtai and Lajtai, 1974, Martin and Chandler, 1994]. During the previous studies, it has been concluded that representative behaviour of rock material, including the post-peak behaviour, can be separated into five different stages based upon stress-strain characteristics. These stages were primarily defined as: crack closure, linear elastic deformation, crack initiation and stable crack growth, critical energy release and unstable crack growth, failure and post-peak behaviour. Figure 2.5 shows typical stress-strain curve of the brittle rock under the compression test and its failure stages.

Stage I is associated to microcrack closure and the initial flaws in the material which continues with stage II, a linear elastic stage. The inelastic behaviour starts at the beginning of stage III and until the end of stage, the hardening response accompanied by fracture process zone with microcrack initiation, can be observed. With an increase of a loading program, stage IV is activated. The stress value at the beginning of this stage (point C) can vary between 50-90% of ultimate strength, while the rest of the stage is characterized by the nonlinear behaviour and more rapid increase of lateral deformation. At the point D, the ultimate strength of specimen is reached and the larger macro-cracks start to propagate through the sample leading to softening of the specimen. At this point, the volumetric strain starts to reverse from a compressive to dilatation behaviour.

The constitutive relations need to be defined outside and at the discontinuity. The constitutive models are constructed within the framework of thermodynamics for a stress resultant beam formulation.

The beam longitudinal and transversal directions are enhanced with additional kinematics, representing modes I and II characterizing softening behaviour, while the rotations keep their standard elastic form. The first two stages of rock failure (up to point B) are kept elastic, with respect to stage I being finished soon after the loading is applied. The

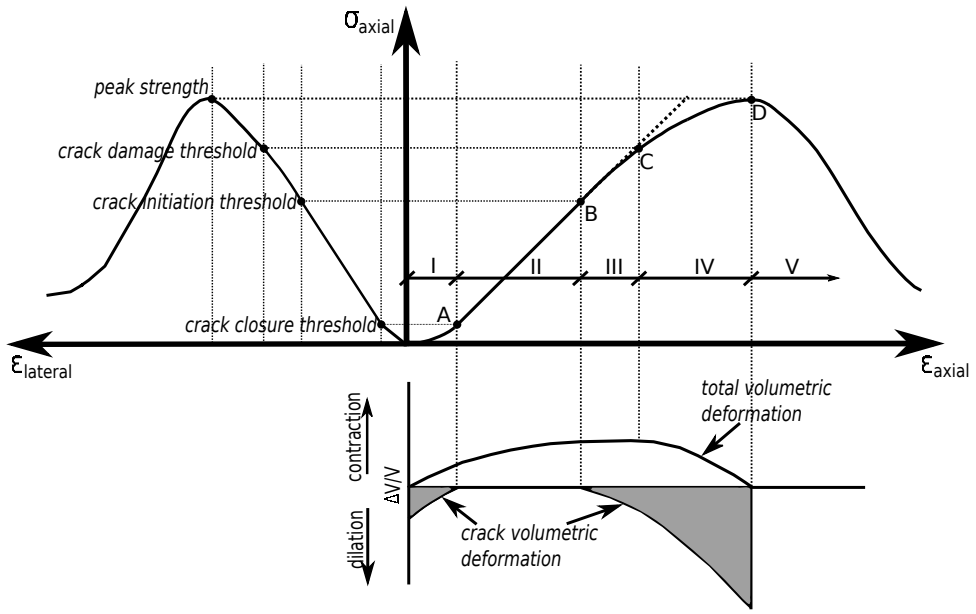

Figure 2.5: Stress-strain curve showing the elements of crack development

linear elastic behaviour is finished when the point B is reached, continuing with hardening. When stage III is activated, significant damage caused by micro-crack propagation starts to occur in the specimen and increases until the highest peak point (point D). The constitutive model for latter stages, which represents a fracture process zone, is chosen as classical plasticity model with isotropic hardening. When the critical point is reached, the complete failure of the specimen is enabled through the exponential softening law. This invokes the enhanced kinematics activation and occurrence of the displacement jumps. The carrying capacity of element reduces with increase in the displacement jump.

In the following equations, the development for the failure of the beam in modes I and II is presented. When the loading starts and softening has not formed yet, the classical elasto-plastic model is considered. The total strains can be additively decomposed into elastic and plastic components

$$\begin{aligned} \varepsilon &= \overline{\varepsilon}^e + \overline{\varepsilon}^p \\ \gamma &= \overline{\gamma}^e + \overline{\gamma}^p. \end{aligned} \tag{2.21}$$

Strain energy functions depend upon elastic strains and hardening variables, $\overline{\xi}^{(u)}$, $\overline{\xi}^{(v)}$:

$$\begin{aligned} \psi_u\left(\varepsilon, \overline{\varepsilon}^p, \overline{\xi}^{(u)}\right) &= \frac{1}{2} EA\left(\varepsilon - \overline{\varepsilon}^p\right)^2 + \frac{1}{2}\overline{\xi}^{(u),2}\overline{K}^{(u)} \\ \psi_v\left(\gamma, \overline{\gamma}^p, \overline{\xi}^{(v)}\right) &= \frac{1}{2} GA\left(\gamma - \overline{\gamma}^p\right)^2 + \frac{1}{2}\overline{\xi}^{(v),2}\overline{K}^{(v)}, \end{aligned} \tag{2.22}$$

where $\overline{K}^{(u)}$ and $\overline{K}^{(v)}$ denote isotropic hardening modulus for longitudinal and transversal

direction. The yield criterion is defined as

$$\begin{aligned}\overline{\Phi}^{(u)}\left(N,\overline{q}^{(u)}\right) &= N-\left(N_y-\overline{q}^{(u)}\right)\leq 0\\ \overline{\Phi}^{(v)}\left(T,\overline{q}^{(v)}\right) &= |T|-\left(T_y-\overline{q}^{(v)}\right)\leq 0,\end{aligned} \tag{2.23}$$

where $\overline{q}^{(u)}=-\overline{K}^{(u)}\overline{\xi}^{(u)}$ and $\overline{q}^{(v)}=-\overline{K}^{(v)}\overline{\xi}^{(v)}$ denote stress-like hardening variables, while N_y and T_y are the forces at yielding point. The state equations are

$$\begin{aligned}N &= EA\left(\varepsilon-\overline{\varepsilon}^{p}\right)\\ T &= GA(\gamma-\overline{\gamma}^{p}).\end{aligned} \tag{2.24}$$

The plastic multiplier parameters $\overline{\gamma}^{(u)}$ and $\overline{\gamma}^{(v)}$ that participate in evolution equations obtained from Kuhn-Tucker optimality conditions [Ibrahimbegovic, 2009] should be introduced. The evolution of internal variables is described in detail in the next section.

Once the ultimate failure point is reached, enhanced kinematics needs to be activated. All further plastic deformation will be accumulated at the discontinuity section, that once passed the peak resistance. The corresponding strain fields containing regular and singular components are obtained:

$$\begin{aligned}\varepsilon &= \overline{\varepsilon}+\overline{\overline{\varepsilon}}=\overline{\varepsilon}^{e}+\overline{\varepsilon}^{p}+\overline{\overline{\varepsilon}}\\ \gamma &= \overline{\gamma}+\overline{\overline{\gamma}}=\overline{\gamma}^{e}+\overline{\gamma}^{p}+\overline{\overline{\gamma}}.\end{aligned} \tag{2.25}$$

The failure criteria for mode I and mode II failure are defined as

$$\begin{aligned}\overline{\overline{\Phi}}^{(u)}\left(t^{(u)},\overline{\overline{q}}^{(u)}\right) &= t^{(u)}-\left(N_u-\overline{\overline{q}}^{(u)}\right)\leq 0\\ \overline{\overline{\Phi}}^{(v)}\left(t^{(v)},\overline{\overline{q}}^{(v)}\right) &= \left|t^{(v)}\right|-\left(T_u-\overline{\overline{q}}^{(v)}\right)\leq 0,\end{aligned} \tag{2.26}$$

where N_u, T_u are the ultimate capacity forces and $\overline{\overline{q}}^{(u)}$, $\overline{\overline{q}}^{(v)}$ are stress-like softening variables which increase exponentially as

$$\begin{aligned}\overline{\overline{q}}^{(u)} &= N_u\left(1-exp\left(-\overline{\overline{\xi}}^{(u)}\frac{N_u}{G_f^{(u)}}\right)\right)\\ \overline{\overline{q}}^{(v)} &= T_u\left(1-exp\left(-\overline{\overline{\xi}}^{(v)}\frac{T_u}{G_f^{(v)}}\right)\right),\end{aligned} \tag{2.27}$$

and $t^{(u)}$, $t^{(v)}$ are traction forces at the discontinuity obtained from equilibrium equations (2.19).

2.4 Computational procedure

In this section the operator split solution procedure for finding the solution for a given problem is presented. The solution will be computed at discrete pseudo-time values $0,t_1,t_2...t$ by means of incremental iterative scheme. The local phase will be treated separately from global phase:

a) The local (element) computation should provide the values of internal variables at the end of time step guaranteeing the plastic admissibility of the stress field. Implicit scheme will be taken for integration of evolution equations. The local computation starts with a best given iterative value of displacements $d_{n+1}^{(u)}$, $d_{n+1}^{(v)}$.

Given: $d_{n+1}^{(u)}, d_{n+1}^{(v)}, \bar{\varepsilon}_n^p, \bar{\gamma}_n^p, \bar{\xi}_n^{(u)}, \bar{\xi}_n^{(v)}, \alpha_n^{(u)}, \alpha_n^{(v)}, \bar{\bar{\xi}}_n^{(u)}, \bar{\bar{\xi}}_n^{(v)}, \Delta t = t_{n+1} - t_n$

Find: $\bar{\varepsilon}_{n+1}^p, \bar{\gamma}_{n+1}^p, \bar{\xi}_{n+1}^{(u)}, \bar{\xi}_{n+1}^{(v)}, \alpha_{n+1}^{(u)}, \alpha_{n+1}^{(v)}, \bar{\bar{\xi}}_{n+1}^{(u)}, \bar{\bar{\xi}}_{n+1}^{(v)}$

b) In the global phase, the current iterative values of nodal displacements are computed while keeping other variables fixed

Given: $d_{n+1}^{(u)}, d_{n+1}^{(v)}, \alpha_{n+1}^{(u)}, \alpha_{n+1}^{(v)}$

Find: $d_{n+1}^{(u)} = d_n^{(u)} + \Delta d_{n+1}^{(u)}, d_{n+1}^{(v)} = d_n^{(v)} + \Delta d_{n+1}^{(v)}$

The subscript n denotes the values of variables at the discrete pseudo time t_n. In the rest of the section, the procedure for calculating internal variables of hardening and softening will be described in details. First, the elastoplastic part of the task needs to be solved, and when the ultimate point is reached, localized failure with softening is triggered. From the previous iterative step, a value of total deformation field is obtained

$$\begin{aligned} \varepsilon_{n+1} &= \textstyle\sum_{a=1}^{2} B_a d_{a,n+1}^{(u)} + \overline{G}\alpha_{n+1}^{(u)} \\ \gamma_{n+1} &= \textstyle\sum_{a=1}^{2} B_a d_{a,n+1}^{(v)} + \overline{G}\alpha_{n+1}^{(v)}. \end{aligned} \tag{2.28}$$

The trial value of stress in the Gauss integration point of element (1 Gaus integration point) is provided

$$\begin{aligned} N_{n+1}^{trial} &= EA(\varepsilon_{n+1} - \bar{\varepsilon}_n^p) \\ V_{n+1}^{trial} &= GA(\gamma_{n+1} - \bar{\gamma}_n^p). \end{aligned} \tag{2.29}$$

Further on, the trial value of yield functions are defined as

$$\begin{aligned} \overline{\Phi}_{n+1}^{(u),trial} &= N_{n+1}^{trial} - \left(N_y - \overline{q}_n^{(u)}\right) \\ \overline{\Phi}_{n+1}^{(v),trial} &= \left|V_{n+1}^{trial}\right| - \left(T_y - \overline{q}_n^{(v)}\right), \end{aligned} \tag{2.30}$$

where

$$\begin{aligned} \overline{q}_n^{(u)} &= -\overline{K}^{(u)}\bar{\xi}_n^{(u)} \\ \overline{q}_n^{(v)} &= -\overline{K}^{(v)}\bar{\xi}_n^{(v)}. \end{aligned} \tag{2.31}$$

If the trial value of the yield function is negative or zero, the elastic trial step is accepted as final and the internal variables at time t_{n+1} remain the same as those already computed at time t_n

$$\begin{aligned} \bar{\varepsilon}_{n+1}^{p,trial} &= \bar{\varepsilon}_n^p, \;\; \bar{\gamma}_{n+1}^{p,trial} = \bar{\gamma}_n^p, \\ \bar{\xi}_{n+1}^{(u),trial} &= \bar{\xi}_n^{(u)}, \;\; \bar{\xi}_{n+1}^{(v),trial} = \bar{\xi}_n^{(v)}. \end{aligned} \tag{2.32}$$

The trial value of force is accepted as the real value, and the tangent modulus C takes the corresponding elastic values

$$\begin{aligned} N_{n+1} &= N_{n+1}^{trial}, \;\; V_{n+1} = V_{n+1}^{trial} \\ C_{n+1}^{(u)} &= EA, \;\; C_{n+1}^{(v)} = GA. \end{aligned} \tag{2.33}$$

However, if the trial value of yield function is positive, the current step is plastic and final values of the internal variables at time t_{n+1} are produced by the plastic flow. The positive value of the plastic multipliers $\overline{\gamma}_{n+1}^{(u)}$ and $\overline{\gamma}_{n+1}^{(v)}$ are firstly computed, followed by the corresponding evolution of the internal variables enforcing the conditions

$$\begin{aligned} \overline{\Phi}_{n+1}^{(u)} &= N_{n+1} - \left(N_y - \overline{q}_{n+1}^{(u)}\right) = 0 \\ \overline{\Phi}_{n+1}^{(v)} &= |V_{n+1}| - \left(V_y - \overline{q}_{n+1}^{(v)}\right) = 0. \end{aligned} \tag{2.34}$$

For the linear hardening law, the positive value of the plastic multipliers is obtained for both longitudinal and transversal direction

$$\begin{aligned} \overline{\gamma}_{n+1}^{(u)} &= \frac{\overline{\Phi}_{n+1}^{(u),trial}}{EA+\overline{K}^{(u)}} \\ \overline{\gamma}_{n+1}^{(v)} &= \frac{\overline{\Phi}_{n+1}^{(v),trial}}{GA+\overline{K}^{(v)}}. \end{aligned} \tag{2.35}$$

Once the plastic multipliers are computed, the rest of the internal variables are updated

$$\begin{aligned} \overline{\varepsilon}_{n+1}^{p} &= \overline{\varepsilon}_{n}^{p} + \overline{\gamma}_{n+1}^{(u)} sign(N_{n+1}^{trial}) \\ \overline{\gamma}_{n+1}^{p} &= \overline{\gamma}_{n}^{p} + \overline{\gamma}_{n+1}^{(v)} sign(V_{n+1}^{trial}) \end{aligned} \tag{2.36}$$

and

$$\begin{aligned} \overline{\xi}_{n+1}^{(u)} &= \overline{\xi}_{n}^{(u)} + \overline{\gamma}_{n+1}^{(u)}, \\ \overline{\xi}_{n+1}^{(v)} &= \overline{\xi}_{n}^{(v)} + \overline{\gamma}_{n+1}^{(v)}. \end{aligned} \tag{2.37}$$

Finally the stress value for the plastic step can be calculated and the tangent modulus C set for the next plastic step

$$\begin{aligned} N_{n+1} = EA(\varepsilon_{n+1} - \overline{\varepsilon}_{n+1}^{p}),\ V_{n+1} = GA(\gamma_{n+1} - \overline{\gamma}_{n+1}^{p}) \\ C_{n+1}^{(u)} = \frac{EA\overline{K}^{(u)}}{EA+\overline{K}^{(u)}},\ C_{n+1}^{(v)} = \frac{GA\overline{K}^{(v)}}{GA+\overline{K}^{(v)}}. \end{aligned} \tag{2.38}$$

When the ultimate stress is reached, the softening part of the task is invoked. From the equation (2.18), a traction forces acting at the discontinuity are obtained. The trial values of traction forces are computed as

$$\begin{aligned} t_{n+1}^{(u),trial} &= EA\left(\varepsilon_{n+1} - \overline{\varepsilon}^{p} + \overline{G}\alpha_{n}^{(u)}\right) \\ t_{n+1}^{(v),trial} &= GA\left(\gamma_{n+1} - \overline{\gamma}^{p} + \overline{G}\alpha_{n}^{(v)}\right), \end{aligned} \tag{2.39}$$

where $\overline{\varepsilon}^{p}$ and $\overline{\gamma}^{p}$ are the final values of plastic deformation obtained from previous steps in hardening part, which remains fixed for the following calculations, and $\alpha_{n}^{(u)}$, $\alpha_{n}^{(v)}$ are

the incompatible mode parameters for softening plastic deformation. The trial values of yield functions are given as

$$\begin{aligned} \overline{\overline{\Phi}}_{n+1}^{(u),trial} &= t_{n+1}^{(u),trial} - \left(N_u - \overline{\overline{q}}_n^{(u)}\right) \\ \overline{\overline{\Phi}}_{n+1}^{(v),trial} &= \left|t_{n+1}^{(v),trial}\right| - \left(V_u - \overline{\overline{q}}_n^{(v)}\right), \end{aligned} \tag{2.40}$$

where

$$\begin{aligned} \overline{\overline{q}}_n^{(u)} &= N_u \left(1 - exp\left(-\overline{\overline{\xi}}_n^{(u)} \frac{N_u}{G_f^{(u)}}\right)\right) \\ \overline{\overline{q}}_n^{(v)} &= V_u \left(1 - exp\left(-\overline{\overline{\xi}}_n^{(v)} \frac{V_u}{G_f^{(v)}}\right)\right). \end{aligned} \tag{2.41}$$

Identically to the hardening part, if the trial value of the yield functions are negative or zero, the elastic trial step is accepted for final, with no modification of the plastic strain from the previous time step.

$$\begin{aligned} \alpha_{n+1}^{(u)} = \alpha_n^{(u)}, \;\; \overline{\overline{\xi}}_{n+1}^{(u)} = \overline{\overline{\xi}}_n^{(u)} \\ \alpha_{n+1}^{(v)} = \alpha_n^{(v)}, \;\; \overline{\overline{\xi}}_{n+1}^{(v)} = \overline{\overline{\xi}}_n^{(v)}. \end{aligned} \tag{2.42}$$

The incompatible mode parameter will remain intact, while the traction force will be changed due to displacement increment.

If the trial values of yield functions are positive, the current step is in the softening plasticity and there is a need to modify the elastic strain and incompatible mode parameters $\alpha_n^{(u)}$, $\alpha_n^{(v)}$ in order to re-establish the plastic admissibility at discontinuity. The internal softening plasticity variables are updated by using evolution equations

$$\begin{aligned} \alpha_{n+1}^{(u)} &= \alpha_n^{(u)} + \overline{\overline{\gamma}}_{n+1}^{(u)} sign\left(t_{n+1}^{(u),trial}\right) \\ \alpha_{n+1}^{(v)} &= \alpha_n^{(v)} + \overline{\overline{\gamma}}_{n+1}^{(v)} sign\left(t_{n+1}^{(v),trial}\right) \end{aligned} \tag{2.43}$$

and

$$\begin{aligned} \overline{\overline{\xi}}_{n+1}^{(u)} &= \overline{\overline{\xi}}_n^{(u)} + \overline{\overline{\gamma}}_{n+1}^{(u)} \\ \overline{\overline{\xi}}_{n+1}^{(v)} &= \overline{\overline{\xi}}_n^{(v)} + \overline{\overline{\gamma}}_{n+1}^{(v)}, \end{aligned} \tag{2.44}$$

where $\overline{\overline{\gamma}}_{n+1}^{(u)}$ and $\overline{\overline{\gamma}}_{n+1}^{(v)}$ denote softening plastic multipliers. The values of the plastic multiplier are determined from the conditions

$$\begin{aligned} \overline{\overline{\Phi}}_{n+1}^{(u)} &= t_{n+1}^{(u)} - \left(N_u - \overline{\overline{q}}_{n+1}^{(u)}\right) < tol \\ \overline{\overline{\Phi}}_{n+1}^{(v)} &= \left|t_{n+1}^{(v)}\right| - \left(V_u - \overline{\overline{q}}_{n+1}^{(v)}\right) < tol \end{aligned} \tag{2.45}$$

while the solutions are found iteratively from two nonlinear equations using the Newton-Raphson method

$$\begin{aligned} \overline{\overline{\Phi}}_{n+1}^{(u)} &= \overline{\overline{\Phi}}_{n+1}^{(u),trial} + \left(\overline{\overline{q}}_{n+1}^{(u)} - \overline{\overline{q}}_n^{(u)}\right) + EA\overline{\overline{G}}\overline{\overline{\gamma}}_{n+1}^{(u)} < tol \\ \overline{\overline{\Phi}}_{n+1}^{(v)} &= \overline{\overline{\Phi}}_{n+1}^{(v),trial} + \left(\overline{\overline{q}}_{n+1}^{(v)} - \overline{\overline{q}}_n^{(v)}\right) + GA\overline{\overline{G}}\overline{\overline{\gamma}}_{n+1}^{(v)} < tol. \end{aligned} \tag{2.46}$$

In the plastic softening step, the traction forces are produced by a change of incompatible mode parameters $\alpha^{(u)}$ and $\alpha^{(v)}$.

After the local computation is finished and the values of internal variables are obtained, the global phase is summoned in order to provide new iterative values of nodal displacements. The set of global equilibrium equations is checked with previously computed internal forces

$$\left\| A_{e=1}^{n_{el}} (f^{int,e,(i)} - f^{ext,e}) < tol \right\|. \tag{2.47}$$

If the convergence is satisfied, new pseudo-time incremental step is performed. If the system still hasn't converged, the new iterative sweep is performed. From the incremental-iterative finite element procedure the new values of nodal displacement are obtained. Contribution of one single element can be stated as

$$\begin{bmatrix} K^{(e)} & F^{(e)} \\ F^{(e),T} & H^{(e)} \end{bmatrix}_{n+1}^{(i)} \begin{pmatrix} \Delta \mathbf{d}_{n+1}^{(e),(i)} \\ \Delta \boldsymbol{\alpha}_{n+1}^{(e),(i)} \end{pmatrix} = \begin{pmatrix} \mathbf{f}_{n+1}^{ext,(e)} - \mathbf{f}_{n+1}^{int,(e),(i)} \\ \mathbf{h}_{n+1}^{(e),(i)} \end{pmatrix}. \tag{2.48}$$

The parts of element stiffness matrix are

$$\begin{aligned} K_{n+1}^{(e),(i)} &= \left(\frac{\partial \mathbf{f}^{int,(e)}}{\partial \mathbf{d}^{(e)}} \right)_{n+1}^{(i)} = \int_0^{l^e} \mathbf{B}^T \mathbf{C}_{n+1} \mathbf{B} dx, \\ F_{n+1}^{(e),(i)} &= \left(\frac{\partial \mathbf{f}^{int,(e)}}{\partial \boldsymbol{\alpha}^{(e)}} \right)_{n+1}^{(i)} = \int_0^{l^e} \mathbf{B}^T \mathbf{C}_{n+1} \overline{\mathbf{G}} dx, \\ H_{n+1}^{(e),(i)} &= \left(\frac{\partial \mathbf{h}^{(e)}}{\partial \boldsymbol{\alpha}^{(e)}} \right)_{n+1}^{(i)} = \int_0^{l^e} \overline{\mathbf{G}}^T \mathbf{C}_{n+1} \overline{\mathbf{G}} dx + \mathbf{K}_s \end{aligned} \tag{2.49}$$

where

$$\mathbf{C}_{n+1} = \begin{bmatrix} C_{n+1}^{(u)} & 0 & 0 \\ 0 & C_{n+1}^{(v)} & 0 \\ 0 & 0 & EI \end{bmatrix}, \quad \overline{\mathbf{G}} = \begin{bmatrix} \overline{G} & 0 & 0 \\ 0 & \overline{G} & 0 \\ 0 & 0 & 0 \end{bmatrix}^T \tag{2.50}$$

Here, the superscript (i) denotes iteration counter.

The static condensation of matrix allows to form the final stiffness matrix for element contribution to FE assembly

$$A_{e=1}^{n_{el}} \left(\widehat{K}_{n+1}^{(e),(i)} \Delta \mathbf{d}_{n+1}^{(e),(i)} \right) = A_{e=1}^{n_{el}} \left(\mathbf{f}^{ext,(e)} - \mathbf{f}^{int,(e),(i)} \right) \tag{2.51}$$

where

$$\widehat{K}_{n+1}^{(e),(i)} = K_{n+1}^{(e),(i)} - F_{n+1}^{(e),(i)} \left(H_{n+1}^{(e),(i)} \right)^{-1} F_{n+1}^{(e),(i),T}. \tag{2.52}$$

Solution of (2.48) provides the value of iterative update $\Delta \mathbf{d}_{n+1}^{(e),(i)}$ and the new iteration can be performed.

2.5 Anisotropic model with multisurface criterion

The main difference in anisotropic model with multisurface criterion [Brancherie and Ibrahimbegovic, 2009, Kucerova et al., 2009, Govindjee et al., 1995] is in providing the full stress reduction simultaneously, where only one softening variable exist $\bar{\bar{q}}$. The latter is present in both of the failure surfaces, controlling the evolution of fracture with following failure surfaces

$$\begin{aligned} \bar{\bar{\Phi}}^{(u)}_{n+1} &= t^{(u)}_{n+1} - \left(N_u - \bar{\bar{q}}_{n+1}\right) \\ \bar{\bar{\Phi}}^{(v)}_{n+1} &= \left|t^{(v)}_{n+1}\right| - \left(T_u - \tfrac{T_u}{N_u}\bar{\bar{q}}_{n+1}\right), \end{aligned} \tag{2.53}$$

where

$$\bar{\bar{q}}_n = N_u \left(1 - exp\left(-\bar{\bar{\xi}}_n \frac{N_u}{G_f^{(u)}}\right)\right). \tag{2.54}$$

Such criterion is suitable for tension case where simultaneous failure regarding two modes is enabled. The solution of the problem is computed by the operator split solution procedure as described in previous section, with the difference in evolution of internal variables

$$\bar{\bar{\xi}}_{n+1} = \bar{\bar{\xi}}_n + \bar{\bar{\gamma}}^{(u)}_{n+1} + \bar{\bar{\gamma}}^{(v)}_{n+1}\frac{T_u}{N_u}. \tag{2.55}$$

This leads to a set of two nonlinear equations with two unknowns

$$\begin{aligned} \bar{\bar{\Phi}}^{(u)}_{n+1} &= \bar{\bar{\Phi}}^{(u),trial}_{n+1} + \left(\bar{\bar{q}}_{n+1} - \bar{\bar{q}}_n\right) + EA\overline{\bar{G}}\bar{\bar{\gamma}}^{(u)}_{n+1} < tol \\ \bar{\bar{\Phi}}^{(v)}_{n+1} &= \bar{\bar{\Phi}}^{(v),trial}_{n+1} + \left(\bar{\bar{q}}_{n+1} - \bar{\bar{q}}_n\right) + GA\overline{\bar{G}}\bar{\bar{\gamma}}^{(v)}_{n+1} sign\left(t^{(v),trial}_{n+1}\right) < tol. \end{aligned} \tag{2.56}$$

It can be noted that, unlike in case with separate failure surfaces, two unknowns are present in both equations. By setting $exp(-\bar{\bar{\xi}}_n \frac{N_u}{G_f^{(u)}}) = 0$, the initial starting value for iterative algorithm is obtained, as well as the advantage of three uncoupled equations.

3 Numerical results

In this section, the numerical results for several numerical tests are presented. First, the validation of the model is shown on simple cohesive link, i.e. beam. The uniaxial tension, compression and shear tests are then performed on heterogeneous 2D rock specimens. The influence of heterogeneity on macroscopic response and failure mechanisms is presented on the specimens with different distributions of phase I and II (strong and weak phase). Finally, the intact rock specimen without pre-existing cracks is put to compression test. The novel model formulations are implemented into the research version of the computer code FEAP, developed by R.L. Taylor [Taylor, 2011].

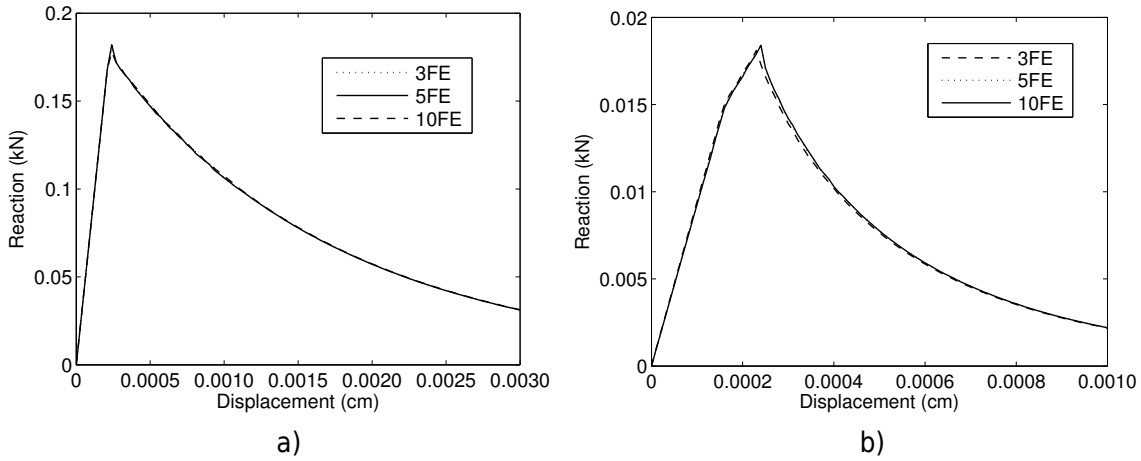

Figure 2.6: The computed beam response for: a) mode I failure and b) mode II failure

3.1 Validation test on beam with embedded discontinuities

The results for a validation test of a beam, fixed at the left end and subjected to tension and shear loading, first separately and then simultaneously, on the right end are presented next. The geometric and material properties of the beam are: $l = 1cm$ (length), $b = 1cm$, $h = 0.8cm$ (cross-section width and height), $E = 1000kN/cm^2$, $\nu = 0.2$, $\sigma_u = 2.2MPa$, $\tau_y = 0.22MPa$, $\tau_u = 0.26MPa$, $\overline{K}^{(u)} = 100kN/cm^2$, $\overline{K}^{(v)} = 100kN/cm^2$, $G_f^{(u)} = 15N/m$, $G_f^{(v)} = 2N/m$. As stated before, the main mechanisms of rock failure are related to mode I and mode II. Mode I failure takes place when a tension is applied to potential crack which continues to grow perpendicular to the direction of loading. Mode I also occurs as a result of movement on the shear plane, when interlocking of asperities result in the propagation of existing vertical cracks. Dealing with rocks, the most dominant failure occurs under shear movement along a plane that is inclined with respect to principal stress direction. This is a mode II failure. As a final possibility, failure can be a combination of these two modes. The clear insight on crack opening and propagating can be gained in this beam example. The beam is subjected to imposed displacements on the free end and the reactions on the fixed end are monitored.

Figure 2.6.a illustrates a beam response when tension is applied and crack opening in mode I occurs. Shear failure of the beam is presented in Figure 2.6.b. It can be seen from Figure 2.6.b. that for shear load, the fracture process zone starts when the first yielding point is reached. The further stress increase allows to reach the ultimate stress and to start softening phase. Exponential softening drives element to complete failure.

The response of the beams are mesh independent, but initial weakness need to be introduced in one element, so that the plastic deformation localizes inside only weaker element, while the rest of the elements elastically unload.

The failure of the beam, which is a combined result of both modes, is shown in Figure 2.7. More precisely, Figure 2.7.a represents a model response where failure hap-

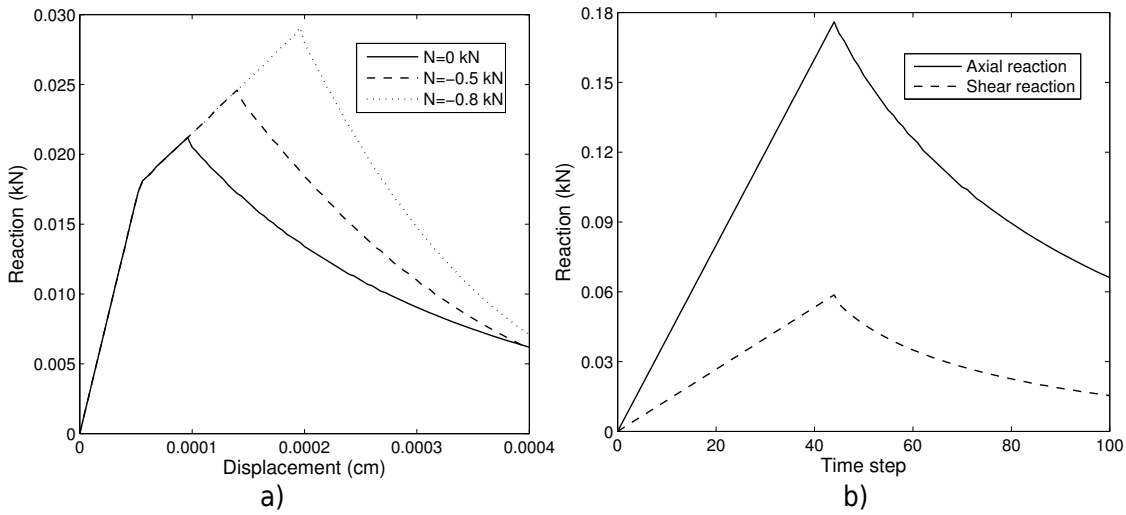

Figure 2.7: The computed beam response: a) shear resistance under different levels of compression force and b) simultaneous softening in mode I and mode II when subjected to tension

pens in mode II under the influence of compression force. The result confirms that the shear strength of soil and rock materials corresponds to the one usually defined by Mohr-Coulomb criterion

$$\tau_f = \tau_u + \sigma_n tg\phi \tag{2.57}$$

where τ_u is cohesion, σ_n is normal stress and $tg\phi$ is angle of friction. The cohesion ($\tau_u = 0.26MPa$) is chosen for a limestone which has a pre-existing cracks lower than 1 mm filled with clay. The simultaneous failure of the beam in both modes is shown in Figure 2.7.b. Once the tension failure criteria is reached, softening in shear happens immediately afterwards.

3.2 Preparation of 2D plain strain rock specimens

2D plane strain rock specimens are constructed next. The specimens are of dimensions 10x10 cm (with unit thickness) and are meshed with triangles by means of Delaunay algorithm. The mesh generation is carried out with a GMSH [Geuzaine and Remacle, 2009]. The specimen has 253 nodes and 704 elements (Figure 2.8). Timoshenko beam elements are positioned on each edge of every triangle in the specimen. Their geometric properties represent the corresponding part in specimen volume. The main hypothesis in constructing the lattice model is that the cells connected by cohesive links (beams) correspond to the representative part of the specimen which have homogeneous properties, while the heterogeneities are introduced through the cohesive links. Thus, the Voronoi cells are derived from Delaunay triangulation and the beam cross sections are computed from the length of the common size of the neighbouring cells (Figure 2.9). The material parameters are taken the same as in the equivalent standard continuum.

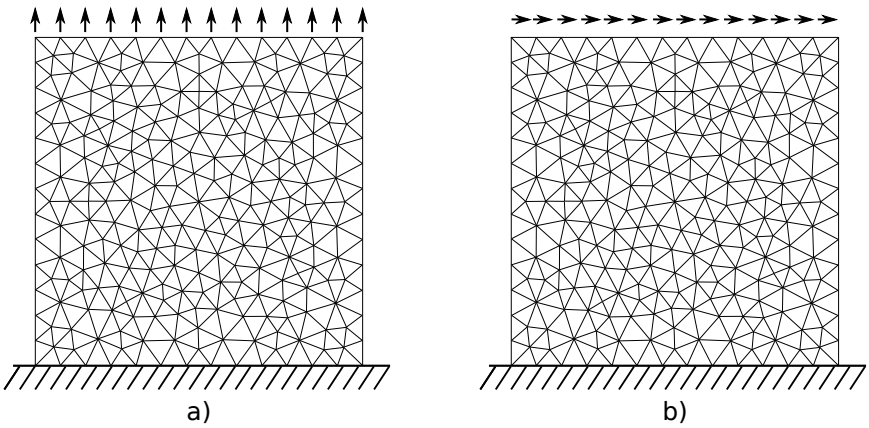

Figure 2.8: A homogeneous 2D plain strain specimen is constructed. Uniaxial tension (a) and shear test (b) are performed in linear elastic regime to validate the model

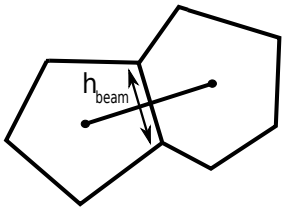

Figure 2.9: Beam cross sections are computed from the length of the common size of the neighbouring cells.

This kind of calculating the lattice parameters has already been successfully used by [Ibrahimbegovic and Delaplace, 2003].

In order to validate the lattice model parameters, the tension and shear tests are conducted in the linear elastic regime on the proposed homogeneous specimen (shown in Figure 2.8) in two versions: lattice model and equivalent standard continuum model with triangular solid elements. The material parameters are the same for each test version: $E = 1000kN/cm^2$, $\nu = 0.2$. The results are presented in Figures 2.10.a and 2.10.b.

The equivalent standard continuum model operate only in linear elastic regime and its response matches with linear elastic regime of lattice models before the failure phase, showing that the proposed model is capable of reproducing classical linear elastic continuum with such computed lattice parameters.

3.3 Numerical tests on heterogeneous specimens

For further tests, heterogeneous specimens are introduced, where the phase II elements are initially weaker and have a lower value of modulus of elasticity, representing pre-existing micro-cracks and other defects. The distribution of phase II is spread across the specimen by a random distribution. The initiation of crack propagation starts when the loading is applied.

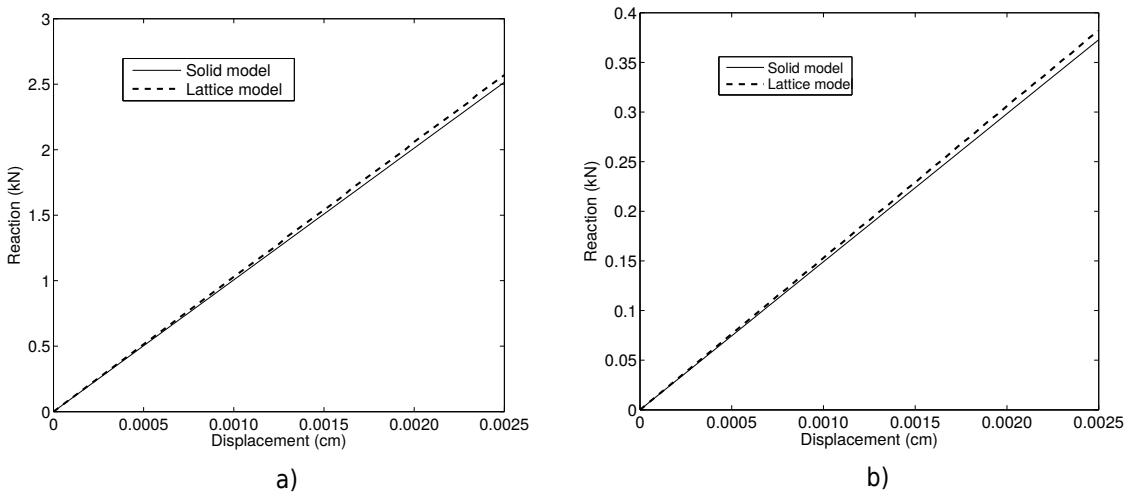

Figure 2.10: Response of homogeneous specimen in linear elastic regime for a) tension test and b) shear test in two versions: solid model with triangles and lattice model

Phase I	**Phase II**
	$E = 1000kN/cm^2$
$E = 7000kN/cm^2$	$\nu = 0.2$
$\nu = 0.2$	$\sigma_u = 2.2MPa, \tau_u = 1.15MPa$
	$G_f^{(u)}$=10 N/m, $G_f^{(v)}$=1.5 N/m
dimensions: 0.1 x 0.1 x 0.01 m; 40% phase II	

Table 2.1: Uniaxial tension test: mechanical and geometric characteristics

Specimens have been subjected to uniaxial tension, compression and shear tests. In each test, the global macro response and failure mechanisms have been monitored. Phase I, being the strong phase, is not likely to break. Micro-cracks will rather start to propagate through the weaker phase, phase II, passing around the strong phase, phase I, and forming the bigger macro-cracks which leads to brittle failure of specimen.

3.3.1 Tension test

The heterogeneous specimen with initially 40% of phase II material is subjected to the imposed displacement of 0.005 cm as shown in the Figure 2.11.a. The dashed lines represent random distribution of the phase II material. The loading program is completed through 50 time steps with the linear load increase. Table 2.1 summarizes the mechanical and geometric characteristics of the specimen used for this experiment. The macroscopic response, shown as sum of all reactions is shown in Figure 2.11.b.

From the obtained macroscopic results (Figure 2.11.b), it is obvious that the specimen is practically completely broken at the end of the loading program. The micro-cracks followed through the phase II material and formed the larger macro-crack that led to

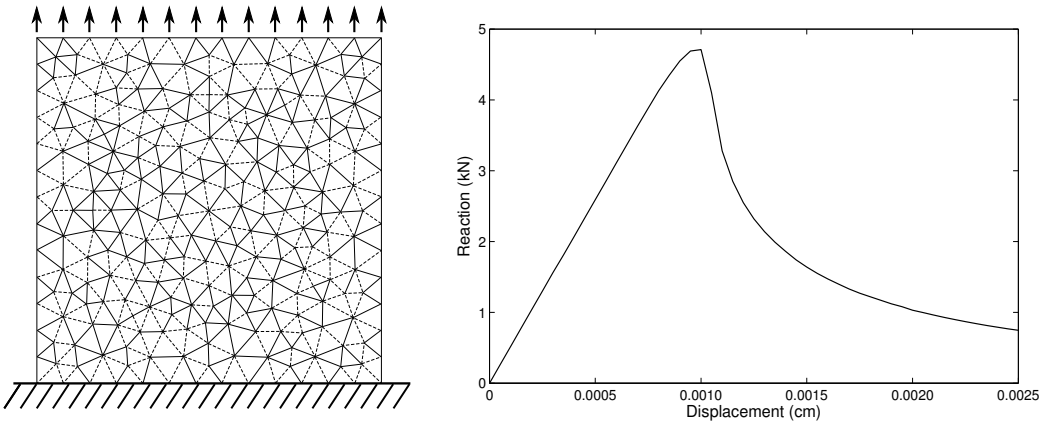

Figure 2.11: Uniaxial tension test: a) mesh and distribution of phase I and phase II (dashed line) b) the computed macroscopic response

complete failure of specimen (see Figure 2.15.a).

3.3.2 Compression test

The specimen with the same geometric properties (see Table 2.2 for mechanical and geometric characteristics used in this experiment) and distribution of phase I and phase II materials is subjected to the imposed displacement of a 0.05 cm, with the loading program of 100 equal load steps. The macroscopic response (Figure 2.12.b) suggest that the specimen is broken. The ductile phase of the response during creation of the fracture process zone is more pronounced here in compression test, than in tension test. Figure 2.13. reveals the overall tension-compression ratio where macroscopic load versus displacement curve is presented for the same specimen. Thus, not only the ductile part with fracture process zone creation is larger, but also the overall resistance to compression failure. The main reason for this is as follows. When the certain element is subjected to shear and compression simultaneously and crack propagates because of the shear, this leads to mode II failure. If the crack propagates in mode II, it is still possible to transfer the compression force through the specimen, assuming that two separated blocks formed during cracking in mode II, lean on each other. However, the compression force in this situation increases until the point where significant damage on the specimen is made, and until cracking is extensive enough that loading capacity starts to decrease. For that reasons, the compression force ought to decrease at certain point, but not momentarily in a sense of instant reduction to zero which would result in impossible global convergence. Thus the exponential softening is also added in compression mode, which leads to robust algorithm, guaranteed convergence and the speed of overall tests. The convergence in each time step is achieved in maximum of 5 iterations. (see Table 2.3 for convergence rate in a typical time step during softening regime). The mechanism described above allows to incorporate the Mohr-Coulomb law.

Phase I	Phase II
	$E = 1000kN/cm^2$
$E = 7000kN/cm^2$	$\nu = 0.2$
$\nu = 0.2$	$\sigma_y = 1.87MPa, \tau_y = 1.0MPa, \overline{K} = 100kN/cm^2$
	$\sigma_u = 2.2MPa, \tau_u = 1.15MPa$
	$G_f^{(u)}$=350 N/m, $G_f^{(v)}$=10 N/m
dimensions: 0.1 x 0.1 x 0.01 m; 40% phase II	

Table 2.2: Uniaxial compression test: mechanical and geometric characteristics

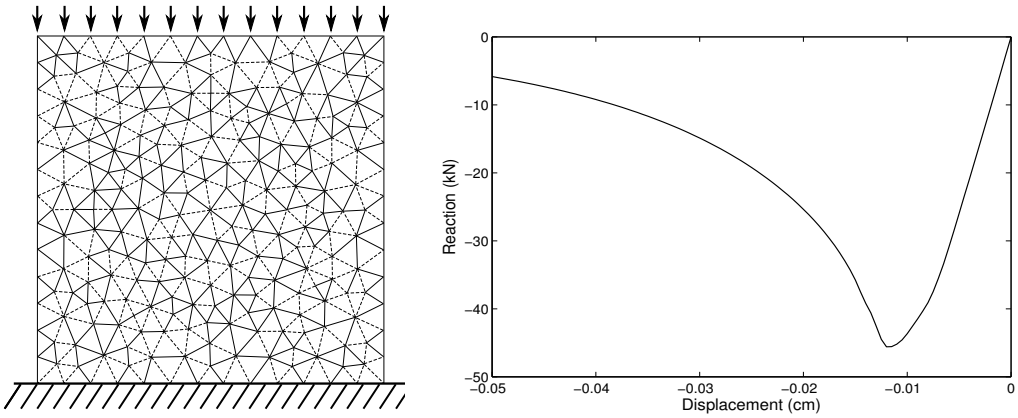

Figure 2.12: Uniaxial compression test: a) mesh and distribution of phase I and phase II (dashed line) b) the computed macroscopic response

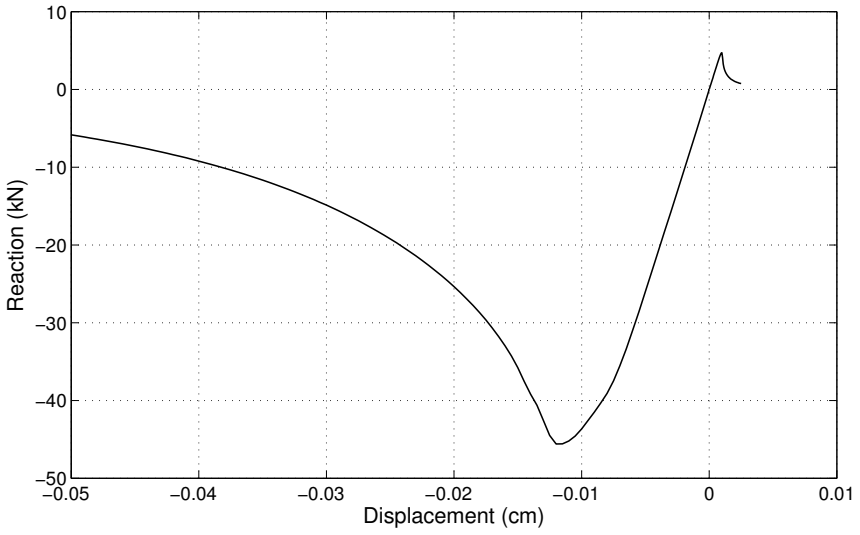

Figure 2.13: Complete macroscopic response for heterogeneous specimen with 40% of phase II

Load step: 33, Iterations: 4, Time increment: 0.01, CPU time(seconds): 1.34				
Iteration no.	1	2	3	4
Residual norm	1.5972276E+01	8.2697984E-03	8.2384402E-07	3.0994455E-14

Table 2.3: Convergence rate in a typical time step

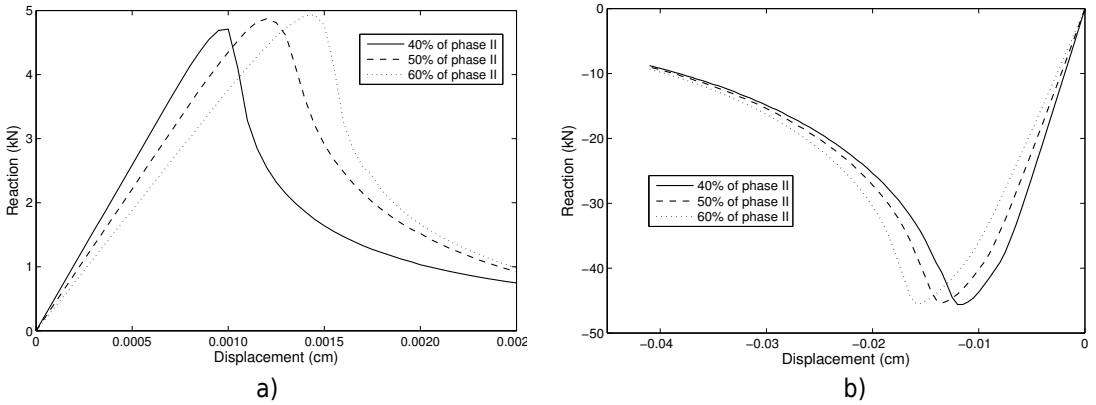

Figure 2.14: The computed macroscopic response with different levels of heterogeneity for: a) uniaxial tension test and b) uniaxial compression test

3.3.3 Influence of heterogeneity in tension and compression tests

In this example, the influence of heterogeneity on a global response is studied. Three different specimens with the same geometric properties (same specimen size), but different levels of heterogeneity are subjected to uniaxial tension and compression tests. The corresponding macroscopic results are shown in Figure 2.14.

The specimens are given different initial properties, specifically with 40, 50 and 60% of phase II material. With an increase of phase II material, the global modulus of elasticity decreases. This is the result of more elements of phase II representing initial weaker material, which makes the global response of specimen more ductile and also with a somewhat lower value of modulus of elasticity. However, it can also be seen from global exponential curve that, when a ratio of phase II material increases, the failure of the specimen becomes more ductile in fracture process zone creation, but also more brittle in the softening response phase, for when the fracture starts the complete failure happens faster. This is due to appearance of many more potential macro-cracks, which drives more quickly the stress to zero.

The failure patterns of three different heterogeneous specimens are shown in Figures 2.15. and 2.16. Figure 2.15. presents the final cracks at the end of tension test computations for the specimens with 40, 50 and 60% of phase II material. It is observed that one dominant macro-crack is present in all of the specimens inducing the final failure mechanism. However, in each specimen the macro-crack formed differently depending on the initial heterogeneity which decides the crack path. Failure due to mode I is more pronounced in tension test.

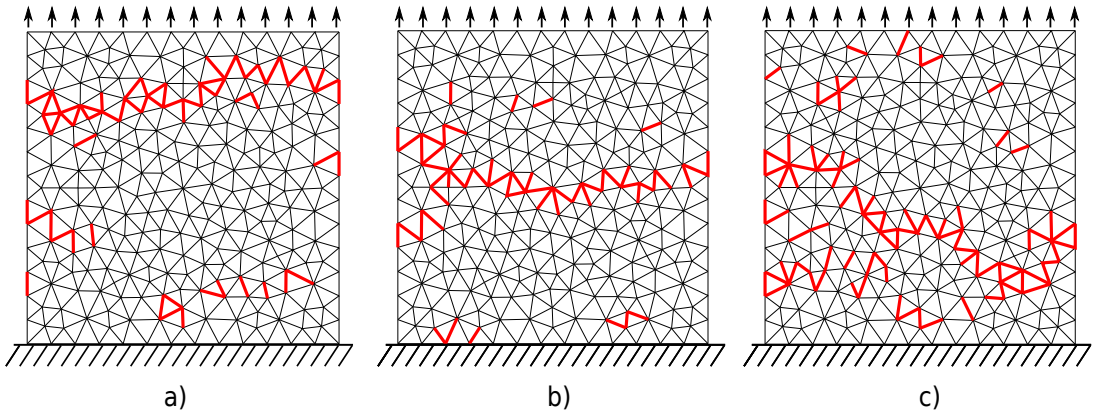

Figure 2.15: Final failure patterns created in tension test for specimens with: a) 40% of phase II, b) 50% of phase II and c) 60% of phase II (broken links are red coloured).

Figure 2.16 reveals the final cracks formed at the end of compression tests where not only one macro-crack is enough to break the specimens. Contrary to tension test crack patterns, in compression test much more macro-cracks are needed to drive the specimens to failure and these are influenced more by mode II mechanism, compared to tension test, which forms the final crack patterns together with mode I. It is important to note that red coloured links in Figures 2.15. and 2.16. represent the failed beam elements. However, the actual cracks are localized inside elements and enable the crack propagation between the Voronoi cells, which are dual to Dealunay triangulation.

In either tension or compression, the difference in reduction of the peak stresses in different specimens remains fairly mild. Having approximately the same peak resistance is quite realistic to expect for the similar failure pattern is created once the threshold is reached. However, the similar peak stresses in compression test leads to conclusion that despite the variations in heterogeneity, crack propagation patterns in each of the samples remain similar with similar failure mechanism present in all of them, which can be observed in Figure 2.16. Specifically, this means that more defects were present in the specimens with more phase II material which made the material softer, but at the same time these were not crucial for complete failure which was caused by similar macro-cracks in all specimens. This leads to conclusion that difference in heterogeneity, that was used here: 40, 50, 60% of phase II, is not as significant to lead to drastically different values of ultimate stresses. The similarity also comes from the same geometries and loading programs of the specimens.

3.3.4 Compression test on intact rock specimen

The intact rock specimen with no pre-existing weak material is put to compression test. Figure 2.17 presents numerically obtained results for intact rock specimen and specimen with 60% of pre-existing micro-cracks, for comparison. In intact rock specimen, there is no initial defects, and modulus of elasticity for all elements is the same (70 Gpa). In this

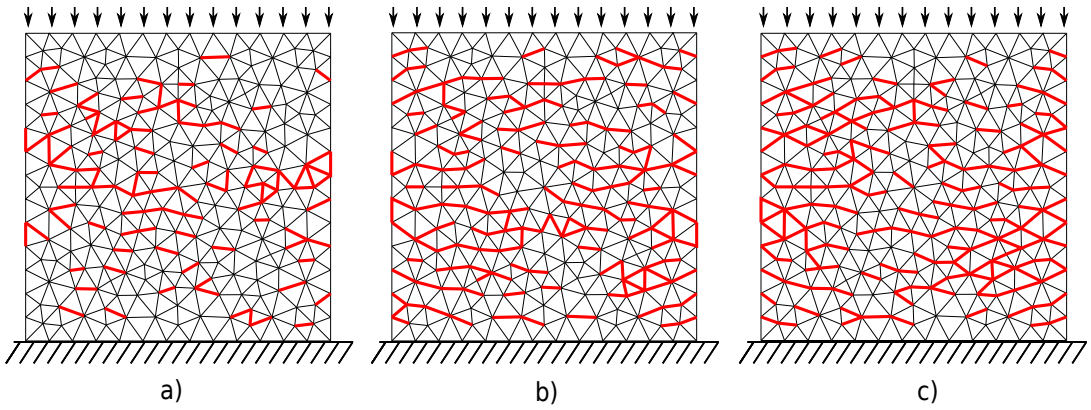

Figure 2.16: Final failure patterns created in compression test for specimens with: a) 40% of phase II, b) 50% of phase II and c) 60% of phase II (broken links are red coloured).

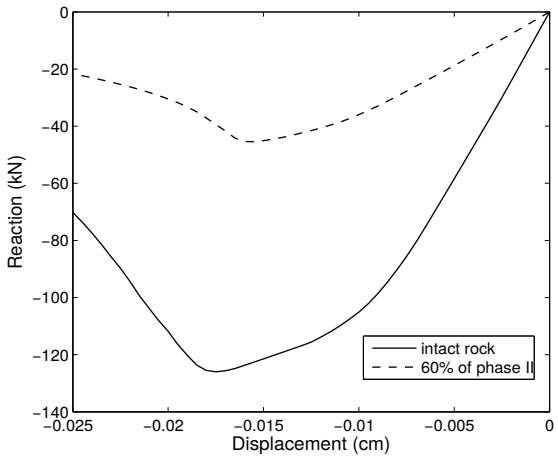

Figure 2.17: Compression test: intact rock vs 60% of phase II specimen

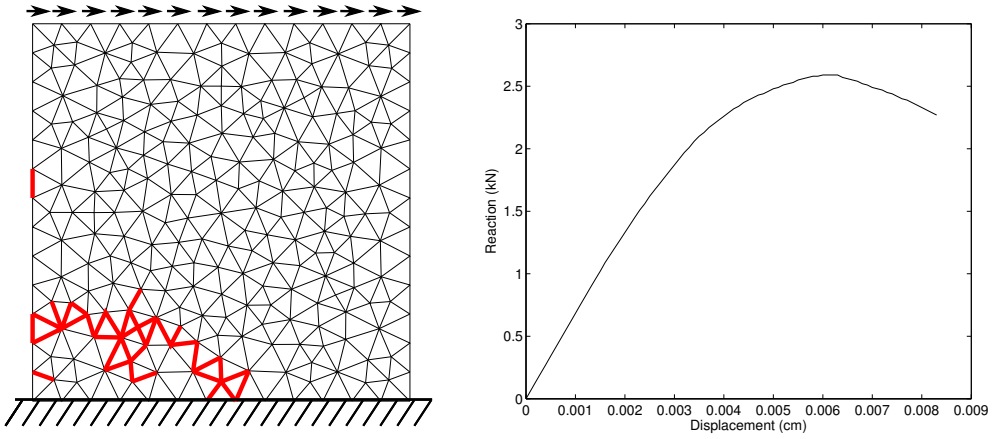

Figure 2.18: Shear test: a) macro-crack at the end of test, b) the computed macroscopic response

analysis the mechanism for failure is also added to intact rock cohesive links. However fracture limits for intact rock elements are higher ($\sigma_u = 6.25MPa, \tau_u = 4.37MPa$) than for previous test, where fracture limits corresponded to initial defects of rock mass. As expected, the global ultimate strength is higher for intact rock specimen, as well as starting global modulus of elasticity. The computational cost is somewhat higher with both phase I and phase II allowed to fail with respect for the one of the models used in previous examples, where the phase I remains elastic. Hence, one can make a judicious choice of these two models, where the most refined model (with both phase I and phase II equiped with failure modes) is only used in the last stage of the analysis.

3.3.5 Shear test

Shear test is performed on the specimen with 40% of pre-existing defects. Macro-crack formed in the lower left angle of the specimen (Figure 2.18.a). The reason that the macroscopic curve of the performed shear test (Figure 2.18.b) did not go all the way down is because the crack formed in the localized part of the specimen.

4 Final comments on the presented 2D rock mechanics model

In this chapter, numerical model suitable for describing failure phenomena in heterogeneous rocks that initially have some pre-existing cracks, defects, pores etc is presented. The behaviour of rock is influenced by heterogeneities, and failure mechanisms lead to displacement discontinuities; thus it is not suitable to represent failure mechanisms with

phenomenological models that are implemented into widely spread commercial codes. The continuum model needed to be abandoned in favour of localized failure mechanisms.

In the proposed discrete model, rock material is presented as assembly of material grains given as Voronoi cells, held together by Timoshenko beams as cohesive links. It is the convenient way for constructing the discrete model since the Voronoi cells are dual to Delaunay triangulation. Two phases are used to describe the heterogeneous properties. Namely, phase I represents the strong phase or intact rock, and phase II stands for pre-existing defects and weak zones.

The most important ingredients of proposed model for rock failure are the representation of failure modes and their implementation. In agreement with experiments, there are two main failure modes, tensile opening and shear sliding mode. The kinematics of Timoshenko elements is enhanced with discontinuity in displacement field, which is related to strong discontinuity. Such approach allows for cracks to propagate between the Voronoi cells (rock grains), which are geometric dual to Delaunay triangulation. Whenever localized failure is initiated through the given criteria, strong discontinuity becomes active.

Another important feature pertains to combining the two failure modes. The plasticity-like model where fracture process zone is presented with isotropic hardening plasticity is presented first, followed by exponential softening. Each of the failure modes in this case is handled separately. Moreover, when mode II is active, compression force can still increase and influence the ultimate shear strength in Mohr-Coulomb way. On the other hand, damage-like multisurface softening is chosen for tension tests when once ultimate strength of either of modes is reached, softening for both modes starts leading to complete failure of element.

As expected, material in compression test was much more resistant than in tension. This is due to Mohr-Coulomb shear strength law, where shear resistance is increased alongside compression force. Obviously, the spatial distribution of the cracks will influence the mechanism of fracture initiation and propagation and it is considered essential to investigate the aspect of forming cracks to fully understand the failure phenomena.

Different types of rock specimens were tested. The rock specimens with 40, 50 and 60% of pre-existing micro-cracks and one intact rock specimen were put to uniaxial tension, compression and shear tests. In order to complete macroscopic failure of specimen, larger macro-crack needs to form from smaller micro-cracks.

The presented model possesses a precisely developed algorithm explained in detail which achieves a desirable convergence for large simulations where a lot of different phenomena happens at the same time. The combination of two failure modes in the right way is crucial to obtain a good converging algorithm, as well as realistic results. This model can be used for different heterogeneous materials where localized discontinuities largely affect the behaviour of material, and where the shear effects and sliding along discontinuities represent important failure cause alongside tension fracture.

Chapter 3

3D rock mechanics model: full set of 3D failure mechanisms

In this chapter a full 3D model capable of representing cracks propagating through the rock until complete localized failure is presented. The model is based upon the discrete lattice of Timoshenko beams that can capture failure modes by using the embedded strong discontinuities. The model can also capture the pre-existing cracks and induced initial heterogeneities with corresponding variability of model parameters. The main advantage of the proposed failure model is in successful representation of full set of 3D failure modes, along with progressive development starting from micro-crack initiation to their coalescence into larger macro-cracks. The complete set of 3D failure modes is included with: mode I of tensile crack-mouth opening, mode II of in-plane shear sliding and mode III of out-of-plane shear sliding, along with the mixed-mode fracture propagation that is often the dominant mechanism in rock failure. Several numerical examples are provided to illustrate the proposed model performance showing the influence of pre-existing cracks and other defects upon the final failure mechanism. The comparison against experimental results is provided for complete model validation.

Contents

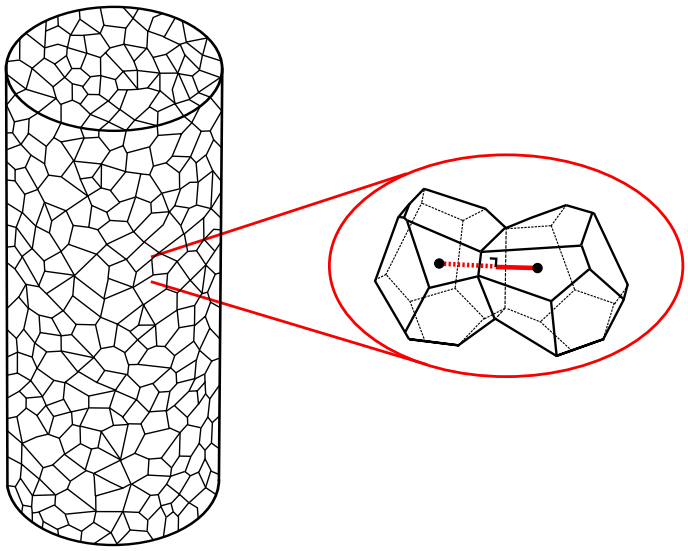

Figure 3.1: Rock material is presented as the assembly of mineral grains (3D Voronoi cells) held together by cohesive links (Timoshenko beams)

1 Model description

The goal of this chapter is to investigate the failure of brittle rocks and to simulate the 3D propagation of discontinuities through the rock taking into consideration the material heterogeneities and pre-existing defects.

Since the FEM method has restrictions in efficient application of the failure analysis, cracking and damage induced discontinuities or singularities, like shown in [Ibrahimbegovic, 2009], the novel approach is adopted. Namely, the discrete lattice approach presented in the previous section for 2D rock mechanics model has been extended here to 3D space.

The geological formation of rocks and their grainy structure (Figure 2.1) allow to construct the discrete lattice model, where the grains are kept together by cohesive forces forming the rock material. A 3D beam lattice model which corresponds to the rock geological structure is provided. Namely, the rock domain is discretized with the 3D Voronoi cells, while the Timoshenko beams act as cohesive links between them (Figure 3.1).

Two papers developed lattice models [Cusatis et al., 2006, Berton and Bolander, 2006], where the 3D domain is discretized with the Voronoi cells. The main difference in the proposed model with respect to those works concerns embedded discontinuities placed within the framework of ED-FEM, where Timoshenko beam elements are equipped with enhanced kinematics capable of capturing the localization effects [Pham et al., 2013], [Jukic et al., 2013, Bui et al., 2014].

Thus, the enhanced kinematics in the strain and displacement fields of cohesive links provide the possibility of discontinuity propagation between the rock grains. This approach corresponds also to the method of incompatible modes that uses mixed variational principle where localization inside finite element happen without any mesh dependency

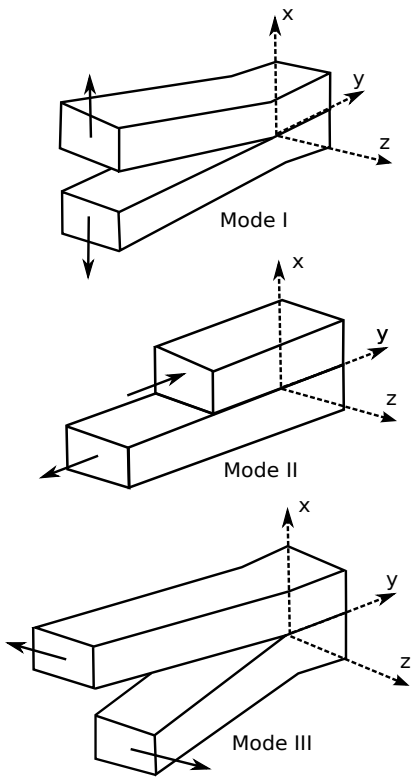

Figure 3.2: Crack opening in modes I, II and III

[Simo et al., 1993, Simo and Rifai, 1990, Ibrahimbegovic and Wilson, 1991]. The robust operator split solution procedure pertaining to 3D space is presented taking into account the displacement, or strong discontinuity, at the level of local computation.

In the presented 3D model, three failure modes are introduced through the kinematic enhancements: mode I representing tensile crack-mouth opening, mode II as shear sliding along cracks mouth and mode III representing a tearing of material as a result of out-of-plane shear stress (see Figure 3.2). More precisely, enrichments in the displacement and strain fields are provided for translational directions x, y and z of the local coordinate system.

3D Timoshenko beams are chosen as cohesive links because of their ability to account for pronounced shear effects in both elastic and plastic phase, occurring in thick beams. The shear contribution can be used to represent failure in modes II and III adding the corresponding displacement discontinuities. Thus, a set of complex failure patterns representing a real complex crack evolution in 3D case is provided. Even though a rock may be subjected to a pure mode I, mode II, or mode III failure, due to the complexity of the geometry and heterogeneities in rock, the crack growth mostly occurs in mixed mode [Stagg and Zienkiewicz, 1968]. Thus, in order to understand the failure behaviour of rock materials, it is necessary to study crack growth under mixed modes I, II and III in the presence of heterogeneities.

The heterogeneities play a crucial role in making the computational iterative proced-

ure more robust by eliminating the academic case of localized failure of homogeneous material under homogeneous stress field. The computational model presented herein is thus leading to more robust iterative procedure. Moreover, the proposed model is suitable for describing any particular microstructure grain size observed in the rock. The main difficulty is in the best probability distribution of the induced heterogeneities in the rock in a priori manner; the latter is in sharp contrast with the concrete, or 'man-made' rock, where the initial distribution can successfully be made in accordance with respect to the concrete granulometry, both for 2D case [Ibrahimbegovic and Delaplace, 2003] or 3D case [Hautefeuille et al., 2009].

The 3D rock mechanics model, presented in this Chapter, is also presented in [Nikolic and Ibrahimbegovic, 2015].

2 3D model formulation

In this section, the 3D Timoshenko beam model is presented, taking into account the additional kinematics for representing the failure modes.

2.1 Kinematics of strong disontinuity

The 3D Timoshenko beams are enhanced with additional kinematics which are capable of simulating displacement or strong discontinuities to model localized failure. The localization implies heterogeneous displacement and strain fields which no longer remain regular even for smooth stress field. The total displacement field $\mathbf{u}$ is written as the sum of smooth regular part $\overline{\mathbf{u}}$ and the localized discontinuous part which is represented as a product between the standard Heaviside function H_{x_d} and the displacement jump $\tilde{\mathbf{u}}$

$$\mathbf{u}(x) = \overline{\mathbf{u}}(x) + \tilde{\mathbf{u}}(x) H_{x_d}(x), \tag{3.1}$$

where

$$H_{x_d}(x) = \begin{cases} 1; & x > x_d \\ 0; & x \leq x_d, \end{cases} \tag{3.2}$$

while x_d is the position of discontinuity. The corresponding deformation field that is produced by such a displacement field can be written as

$$\boldsymbol{\varepsilon}(x) = \frac{d}{dx}\overline{\mathbf{u}}(x) + \tilde{\mathbf{u}}(x)\delta_{x_d}(x), \tag{3.3}$$

where $\frac{d}{dx}$ is a derivative with respect to x and

$$\delta_{x_d}(x) = \begin{cases} \infty; & x = x_d \\ 0; & otherwise. \end{cases} \tag{3.4}$$

The theoretical framework suitable for this kind of enhancement is provided by method of incompatible modes and Hu-Washizu mixed variational formulation [Washizu, 1982, Simo et al., 1993] where displacement field is separated from strain and stress virtual fields.

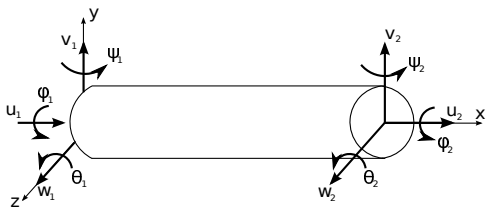

Figure 3.3: A 3D 2-node Timoshenko beam

2.2 The finite element approximation

To model the cohesive links, the Timoshenko beam elements are used. Let us consider one beam element e with length l^e. All further equations will be expressed in local coordinate system, where the local level will be denoted with superscript e. At the end the standard local-global transformation will be performed. The standard kinematics for 3D Timoshenko element (see [Luo, 2008]) when beam cross-sections are symmetrical, or the element local coordinate axes are selected to pass through the cross-section shear centre are

$$\begin{aligned}
\varepsilon(x) &= \frac{du(x)}{dx} \\
\gamma_y(x) &= \frac{dv(x)}{dx} - \theta(x) \\
\gamma_z(x) &= \frac{dw(x)}{dx} + \psi(x) \\
\kappa_x(x) &= \frac{d\varphi(x)}{dx} \\
\kappa_y(x) &= \frac{d\psi(x)}{dx} \\
\kappa_z(x) &= \frac{d\theta(x)}{dx},
\end{aligned} \tag{3.5}$$

where the standard beam strain vector is $\overline{\epsilon} = \begin{bmatrix} \varepsilon & \gamma_y & \gamma_z & \kappa_x & \kappa_y & \kappa_z \end{bmatrix}^T$. The chosen Timoshenko beam element has 2-node interpolation and a single Gauss point integration, which makes all deformation values constant. The standard displacement field is interpolated as

$$\overline{\mathbf{u}} = \mathbf{N}\overline{\mathbf{u}}_a, \tag{3.6}$$

where vector $\overline{\mathbf{u}} = \begin{bmatrix} u & v & w & \varphi & \psi & \theta \end{bmatrix}^T$ represent the beam displacements as shown in Figure 3.3, $\overline{\mathbf{u}}_a = \begin{bmatrix} \overline{\mathbf{u}}_1 & \overline{\mathbf{u}}_2 \end{bmatrix}^T$ is the nodal displacement vector and $\mathbf{N}^e$ is element shape function matrix

$$\mathbf{N} = \begin{bmatrix}
N_1 & 0 & 0 & 0 & 0 & 0 & N_2 & 0 & 0 & 0 & 0 & 0 \\
0 & N_1 & 0 & 0 & 0 & 0 & 0 & N_2 & 0 & 0 & 0 & 0 \\
0 & 0 & N_1 & 0 & 0 & 0 & 0 & 0 & N_2 & 0 & 0 & 0 \\
0 & 0 & 0 & N_1 & 0 & 0 & 0 & 0 & 0 & N_2 & 0 & 0 \\
0 & 0 & 0 & 0 & N_1 & 0 & 0 & 0 & 0 & 0 & N_2 & 0 \\
0 & 0 & 0 & 0 & 0 & N_1 & 0 & 0 & 0 & 0 & 0 & N_2
\end{bmatrix} \tag{3.7}$$

with $N_1(x) = 1 - \frac{x}{l^e}$, $N_2(x) = \frac{x}{l^e}$.

The matrix form of beam strain-displacement relation from eq. (3.5) can be written as

$$\overline{\epsilon} = \mathbf{B}\overline{\mathbf{u}}_a, \tag{3.8}$$

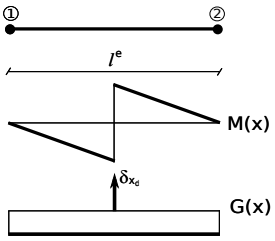

Figure 3.4: The additional shape functions for displacement jump

where **B** is the beam strain-displacement matrix

$$\mathbf{B} = \begin{bmatrix} B_1 & 0 & 0 & 0 & 0 & 0 & B_2 & 0 & 0 & 0 & 0 & 0 \\ 0 & B_1 & 0 & 0 & 0 & -N_1 & 0 & B_2 & 0 & 0 & 0 & -N_2 \\ 0 & 0 & B_1 & 0 & N_1 & 0 & 0 & 0 & B_2 & 0 & N_2 & 0 \\ 0 & 0 & 0 & B_1 & 0 & 0 & 0 & 0 & 0 & B_2 & 0 & 0 \\ 0 & 0 & 0 & 0 & B_1 & 0 & 0 & 0 & 0 & 0 & B_2 & 0 \\ 0 & 0 & 0 & 0 & 0 & B_1 & 0 & 0 & 0 & 0 & 0 & B_2 \end{bmatrix} \tag{3.9}$$

and $B_1(x) = -\frac{1}{l^e}, B_2(x) = \frac{1}{l^e}$. The beam displacement field ought to be enhanced as shown in eq. (3.1) and appropriate FE approximation should be performed. First, the eq. (3.1) can be rewritten by using the N_2 shape function as shown in [Pham et al., 2013].

$$\mathbf{u}(x) = \underbrace{\overline{\mathbf{u}}(x) + \tilde{\mathbf{u}} N_2(x)}_{\text{regular part of total displacement field}} + \underbrace{\tilde{\mathbf{u}} \underbrace{(H_{x_d} - N_2(x))}_{\text{M(x)}}}_{\text{localized part}} \tag{3.10}$$

which results with $M(x)$ function that cancels the contribution of displacement jump $\tilde{\mathbf{u}}$ on the boundary of the element (Figure 3.4). The $G(x)$ is a first derivative of $M(x)$.

$$M(x) = \begin{cases} -\frac{x}{l^e}; x \in [0, x_d\rangle \\ 1 - \frac{x}{l^e}; x \in \langle x_d, l^e] \end{cases}, \quad G(x) = -\frac{1}{l^e} + \delta_{x_d} \tag{3.11}$$

Such a formulation leads to local contribution of discontinuity. The displacement field from eq. (3.10) leads to the enhanced strain field corresponding to eq. (3.3). Local function $M(x)$ introduces the discontinuity enhancement in the middle of the beam. This corresponds to the Voronoi cell network, where each beam is cut in half by the two neighbouring Voronoi cells.

The kinematics is enhanced here so that the failure modes I,II and III can be simulated, resulting with displacement jumps in the directions x,y and z of local coordinate frame. The first part in eq. (3.10) keeps the same boundary values as the total displacement field, which can now be interpolated as

$$\mathbf{u} = \mathbf{N}\overline{\mathbf{u}}_a + \mathbf{M}\tilde{\mathbf{u}}. \tag{3.12}$$

The interpolated enhanced displacement field (3.12) produces the following interpolated enhanced deformation field:

$$\boldsymbol{\epsilon} = \mathbf{B}\overline{\mathbf{u}}_a + \mathbf{G}\tilde{\mathbf{u}}, \tag{3.13}$$

where $\mathbf{M}$ and $\mathbf{G}$ are 6×6 matrices containing the additional functions $M(x)$ and their derivatives $G(x)$ at the positions of potential displacement jumps

$$\mathbf{M} = \begin{bmatrix} M & 0 & 0 & 0 & 0 & 0 \\ 0 & M & 0 & 0 & 0 & 0 \\ 0 & 0 & M & 0 & 0 & 0 \\ 0 & 0 & 0 & 0 & 0 & 0 \\ 0 & 0 & 0 & 0 & 0 & 0 \\ 0 & 0 & 0 & 0 & 0 & 0 \end{bmatrix}, \quad \mathbf{G} = \begin{bmatrix} G & 0 & 0 & 0 & 0 & 0 \\ 0 & G & 0 & 0 & 0 & 0 \\ 0 & 0 & G & 0 & 0 & 0 \\ 0 & 0 & 0 & 0 & 0 & 0 \\ 0 & 0 & 0 & 0 & 0 & 0 \\ 0 & 0 & 0 & 0 & 0 & 0 \end{bmatrix} \tag{3.14}$$

and $\tilde{\mathbf{u}} = \begin{bmatrix} \tilde{u} & \tilde{v} & \tilde{w} & 0 & 0 & 0 \end{bmatrix}^T$ is a vector of element displacement jumps in the direction of local axes.

2.3 Virtual work

The enhanced interpolation for deformation field obtained from (3.13) is used in the same way to obtain the virtual deformation field

$$\delta\boldsymbol{\epsilon} = \mathbf{B}\delta\overline{\mathbf{u}}_a + \mathbf{G}\delta\tilde{\mathbf{u}}, \tag{3.15}$$

where $\delta\boldsymbol{\epsilon}$, $\delta\overline{\mathbf{u}}_a$ and $\delta\tilde{\mathbf{u}}$ denote respectively the generalized virtual deformation field, regular part of total virtual displacement field and enhanced part of total virtual displacement field. The only difference in real and virtual deformation fields concerns the modified $\tilde{\mathbf{G}}$. It is necessary to enforce the orthogonality between the enhanced strain and constant stress within the element which fulfils the patch test [Ibrahimbegovic and Wilson, 1991].

$$\widetilde{\mathbf{G}} = \mathbf{G} - \frac{1}{l_e}\int_0^{l^e} \mathbf{G}dx. \tag{3.16}$$

When the interface is positioned in the middle of an element, condition (3.16) is automatically verified and $\widetilde{\mathbf{G}}$ remains the same as $\mathbf{G}$. The matrix $\mathbf{G}$ will further be decomposed into two matrices

$$\mathbf{G} = \overline{\mathbf{G}} + \boldsymbol{\delta}_{x_d}. \tag{3.17}$$

The matrix $\overline{\mathbf{G}}$ contains only the regular parts of function $G(x)$: $\overline{G}(x) = -\frac{1}{l^e}$. The $(\boldsymbol{\delta}_{x_d})_{ij} = \delta_{ij}\delta_{x_d}$, where δ_{ij} is the Kronecker delta in Cartesian coordinates, and δ_{x_d} is the Dirac delta function in 1D centred at x_d. The virtual work equation is written at element level $G^{int,(e)} - G^{ext,(e)} = 0$ where

$$G^{int,(e)} = \int_0^{l^e} (\delta\boldsymbol{\epsilon})^T \boldsymbol{\sigma} dx = \underbrace{\int_0^{l^e} (\mathbf{B}\delta\overline{\mathbf{u}}_a)^T \boldsymbol{\sigma} dx}_{\text{standard}} + \underbrace{\int_0^{l^e} \delta\tilde{\mathbf{u}}^T (\overline{\mathbf{G}} + \boldsymbol{\delta}_{x_d})\boldsymbol{\sigma} dx}_{\text{enhanced}} \tag{3.18}$$

and $\boldsymbol{\sigma} = \begin{bmatrix} N & V & W & M_x & M_y & M_z \end{bmatrix}^T$ represents element stress resultant vector. The standard internal force vector $\mathbf{f}^{int,(e)}$ is obtained from the standard part of internal virtual work, while the enhanced part produces the element residual $\mathbf{h}^{(e)}$ at discontinuity

$$\mathbf{f}^{int,(e)} = \int_0^{l^e} \mathbf{B}^T \boldsymbol{\sigma} dx, \;\; \mathbf{h}^{(e)} = \int_0^{l^e} (\overline{\mathbf{G}} + \boldsymbol{\delta}_{x_d}) \boldsymbol{\sigma}^e dx. \tag{3.19}$$

In order to have the smooth stress field, the condition $\mathbf{h}^{(e)} = 0$ needs to be enforced which leads to traction vector $\mathbf{t} = \int_0^{l^e} \boldsymbol{\delta}_{x_d} \boldsymbol{\sigma} dx$ at the discontinuity

$$\mathbf{t} = -\int_0^{l^e} \overline{\mathbf{G}} \boldsymbol{\sigma} dx \tag{3.20}$$

The traction vector at discontinuity is in relation with the forces in the bulk and

$$\boldsymbol{\sigma} = \mathbf{C} \overline{\boldsymbol{\epsilon}} \tag{3.21}$$

where $\mathbf{C}$ is material matrix of Timoshenko beam

$$\mathbf{C} = \begin{bmatrix} EA & 0 & 0 & 0 & 0 & 0 \\ 0 & GA\xi & 0 & 0 & 0 & 0 \\ 0 & 0 & GA\xi & 0 & 0 & 0 \\ 0 & 0 & 0 & GI_{pol} & 0 & 0 \\ 0 & 0 & 0 & 0 & EI_{11} & 0 \\ 0 & 0 & 0 & 0 & 0 & EI_{22} \end{bmatrix} \tag{3.22}$$

Here, E and G are the modulus of elasticity and shear modulus, A, I_{pol}, I_{11}, I_{22} and ξ are the beam cross section properties, respectively cross-section area, polar moment of inertia, two mass moments of inertia and shear factor.

2.4 Constitutive model

The behaviour of the material is considered linear elastic up to the beam cross-section failure point $\boldsymbol{\sigma}_u = \begin{bmatrix} N_u & V_u & W_u & 0 & 0 & 0 \end{bmatrix}^T$. The cross section failure happens at the weakest beam point and activates the discontinuity which is positioned in the middle of the beam at the Gauss integration point. All further plastic deformation will be accumulated at the position of discontinuity and will thus contain regular and singular components as shown in eqs. (3.3) and (3.13). It has been shown by [Simo et al., 1993] that, in the presence of discontinuous field (3.1), the failure functions can be written similarly to standard plasticity model yield functions. However, the only difference with respect to standard plasticity is that the softening failure functions now concern the stress resultants that are localized at the discontinuity x_d

$$\begin{aligned} &\Phi_{\tilde{u}}(N, q_{\tilde{u}}(\tilde{u}))|_{x=x_d} = [N - (N_u - q_{\tilde{u}}(\tilde{u}))]_{x=x_d} \\ &\Phi_{\tilde{v}}(V, q_{\tilde{v}}(\tilde{v}))|_{x=x_d} = [|V| - (V_u - q_{\tilde{v}}(\tilde{v}))]_{x=x_d} \\ &\Phi_{\tilde{w}}(W, q_{\tilde{w}}(\tilde{w}))|_{x=x_d} = [|W| - (W_u - q_{\tilde{w}}(\tilde{w}))]_{x=x_d}, \end{aligned} \tag{3.23}$$

where individual failure functions $\Phi_{\tilde{u}}$, $\Phi_{\tilde{v}}$ and $\Phi_{\tilde{w}}$ are presented for normal direction and two shear directions; $q_{\tilde{u}}$, $q_{\tilde{v}}$ and $q_{\tilde{w}}$ are individual stress-like softening variables, which follow exponential softening law and need to be localized as well

$$\begin{aligned} q_{\tilde{u}}(\tilde{u})|_{x=x_d} &= \left[N_u\left(1-exp\left(-\tfrac{N_u}{G_{f,\tilde{u}}}|\tilde{u}|\right)\right)\right]_{x=x_d} \\ q_{\tilde{v}}(\tilde{v})|_{x=x_d} &= \left[V_u\left(1-exp\left(-\tfrac{V_u}{G_{f,\tilde{v}}}|\tilde{v}|\right)\right)\right]_{x=x_d} \\ q_{\tilde{w}}(\tilde{w})|_{x=x_d} &= \left[W_u\left(1-exp\left(-\tfrac{W_u}{G_{f,\tilde{w}}}|\tilde{w}|\right)\right)\right]_{x=x_d}. \end{aligned} \tag{3.24}$$

Here $G_{f,\tilde{u}}$, $G_{f,\tilde{v}}$ and $G_{f,\tilde{w}}$ are the fracture energies, which are computed as

$$\begin{aligned} G_{f,\tilde{u}} &= \int_0^\infty N_u exp\left(-\tfrac{N_u}{G_{f,\tilde{u}}}|\tilde{u}|\right)d\tilde{u} \\ G_{f,\tilde{v}} &= \int_0^\infty V_u exp\left(-\tfrac{V_u}{G_{f,\tilde{v}}}|\tilde{v}|\right)d\tilde{v} \\ G_{f,\tilde{w}} &= \int_0^\infty W_u exp\left(-\tfrac{W_u}{G_{f,\tilde{w}}}|\tilde{w}|\right)d\tilde{w}. \end{aligned} \tag{3.25}$$

The softening moduli are obtained as the derivatives of the exponential softening laws from (3.24) with respect to the corresponding displacement jumps leading to their localized form

$$\begin{aligned} K_{s,\tilde{u}}|_{x=x_d} &= \left[\tfrac{dq_{\tilde{u}}(\tilde{u})}{d\tilde{u}}\right]_{x=x_d} \\ K_{s,\tilde{v}}|_{x=x_d} &= \left[\tfrac{dq_{\tilde{v}}(\tilde{v})}{d\tilde{v}}\right]_{x=x_d} \\ K_{s,\tilde{w}}|_{x=x_d} &= \left[\tfrac{dq_{\tilde{w}}(\tilde{w})}{d\tilde{w}}\right]_{x=x_d}. \end{aligned} \tag{3.26}$$

In order to continue with the embedded discontinuity representation towards computational development, additional internal plastic parameters will be introduced: α_* which can be treated as incompatible mode parameter [Simo and Rifai, 1990]; ξ_* such that $\xi_* \equiv |\alpha_*|$; and λ_* as the plastic multiplier. The $*$ stands for each of the directional components regarding local axes. The presence of discontinuous field causes the softening plastic strain variables to be localized at the discontinuity while the stress field remains smooth (for more details see [Simo et al., 1993]). With that in mind, the evolution of localized internal plastic variables is given as

$$\begin{aligned} \dot{\alpha}_{\tilde{u}} &= \left[\dot{\lambda}_{\tilde{u}} sign(t_{\tilde{u}})_{x=x_d}\right]\delta_{x_d},\ \ \dot{\xi}_{\tilde{u}} = \dot{\lambda}_{\tilde{u}}\delta_{x_d} \\ \dot{\alpha}_{\tilde{v}} &= \left[\dot{\lambda}_{\tilde{v}} sign(t_{\tilde{v}})_{x=x_d}\right]\delta_{x_d},\ \ \dot{\xi}_{\tilde{v}} = \dot{\lambda}_{\tilde{v}}\delta_{x_d} \\ \dot{\alpha}_{\tilde{w}} &= \left[\dot{\lambda}_{\tilde{w}} sign(t_{\tilde{w}})_{x=x_d}\right]\delta_{x_d},\ \ \dot{\xi}_{\tilde{w}} = \dot{\lambda}_{\tilde{w}}\delta_{x_d}. \end{aligned} \tag{3.27}$$

The loading and unloading conditions are

$$\begin{aligned} &\dot{\lambda}_{\tilde{u}} \geq 0,\ \ \Phi_{\tilde{u}} \leq 0,\ \ \left[\dot{\lambda}_{\tilde{u}}\Phi_{\tilde{u}}\right]_{x=x_d} = 0 \\ &\dot{\lambda}_{\tilde{v}} \geq 0,\ \ \Phi_{\tilde{v}} \leq 0,\ \ \left[\dot{\lambda}_{\tilde{v}}\Phi_{\tilde{v}}\right]_{x=x_d} = 0 \\ &\dot{\lambda}_{\tilde{w}} \geq 0,\ \ \Phi_{\tilde{w}} \leq 0,\ \ \left[\dot{\lambda}_{\tilde{w}}\Phi_{\tilde{w}}\right]_{x=x_d} = 0. \end{aligned} \tag{3.28}$$

2.5 Computational procedure

The local phase of the operator split procedure for finding the numerical solution at pseudo time t_{n+1} within the particular loading program is presented next. The operator split is performed for each directional component individually. The ultimate goal of the local operator split algorithm is to compute the internal variables and with the newly obtained values proceed to the global solution procedure. The local computation starts with previously calculated values $\alpha_{*,n}$, $\xi_{*,n}$, and the best guess for nodal displacements at next time u_{n+1}, v_{n+1} and w_{n+1}. The elastic trial state for all of the directional components can be obtained

$$\begin{aligned} \varepsilon_{n+1} &= \sum_{a=1}^{2} B_a u_{a,n+1} + \overline{G}\alpha_{\tilde{u},n} \\ \gamma_{y,n+1} &= \sum_{a=1}^{2} B_a v_{a,n+1} + \overline{G}\alpha_{\tilde{v},n} \\ \gamma_{z,n+1} &= \sum_{a=1}^{2} B_a w_{a,n+1} + \overline{G}\alpha_{\tilde{w},n} \end{aligned} \tag{3.29}$$

$$\begin{aligned} t^{trial}_{\tilde{u},n+1} &= \int_0^{l^e} \overline{G}EA\varepsilon_{n+1}dx \\ t^{trial}_{\tilde{v},n+1} &= \int_0^{l^e} \overline{G}GA\gamma_{y,n+1}dx \\ t^{trial}_{\tilde{w},n+1} &= \int_0^{l^e} \overline{G}GA\gamma_{z,n+1}dx \end{aligned} \tag{3.30}$$

$$\begin{aligned} \Phi^{trial}_{\tilde{u},n+1} &= t^{trial}_{\tilde{u},n+1} - (N_u - q_{\tilde{u},n}) \\ \Phi^{trial}_{\tilde{v},n+1} &= \left| t^{trial}_{\tilde{v},n+1} \right| - (V_u - q_{\tilde{v},n}) \\ \Phi^{trial}_{\tilde{w},n+1} &= \left| t^{trial}_{\tilde{w},n+1} \right| - (W_u - q_{\tilde{w},n}), \end{aligned} \tag{3.31}$$

where stress-like softening variables $q_{\tilde{u},n}$, $q_{\tilde{v},n}$, $q_{\tilde{w},n}$ are defined as shown in eq. (3.24). If any of the component trial failure functions $\Phi^{trial}_{*,n+1} \leq 0$, the elastic trial step is indeed the correct solution with

$$\alpha_{*,n+1} = \alpha_{*,n}, \;\; \xi_{*,n+1} = \xi_{*,n} \tag{3.32}$$

The $*$ denotes each directional component. In the opposite case when $\Phi^{trial}_{*,n+1} > 0$, the step is really plastic and the values of internal variables need to be corrected

$$\alpha_{*,n+1} = \alpha_{*,n} + \lambda_{*,n+1} sign\left(t^{trial}_{*,n+1}\right), \;\; \xi_{*,n+1} = \xi_{*,n} + \lambda_{*,n+1} \tag{3.33}$$

It still remains to compute the plastic multipliers $\lambda_{*,n+1}$. The corresponding value of the plastic multipliers ought to be determined from the condition $\Phi_{*,n+1} = 0$. The iteration is required to find the solution of a single nonlinear equation with $\lambda_{*,n+1}$ as unknown

$$\Phi_{*,n+1} = \Phi^{trial}_{*,n+1} + (q_{*,n+1} - q_{*,n}) + C_* \overline{G}\lambda_{*,n+1} < tol. \tag{3.34}$$

The Newton algorithm is used to solve the local nonlinear equations. It takes no more than 4 iterations to converge on a local level.

2.6 The global solution procedure

After the local computation is completed, the global phase is invoked in order to provide new iterative values of nodal displacements. The set of global equilibrium equations is

checked with previously computed internal forces

$$\|A_{e=1}^{n_{el}}(\mathbf{f}^{int,e,(i)}(\mathbf{u}_{n+1}^{(i)} - \boldsymbol{\alpha}_{n+1}) - \mathbf{f}^{ext,e})\| \leq tol, \tag{3.35}$$

where $A_{e=1}^{n_{el}}$ is standard finite element assembly operator and (i) is iteration counter. After the convergence is achieved, a new incremental step is performed. The finite element contribution of one element to linearised variational principle can be written in a matrix form

$$\begin{bmatrix} \mathbf{K}^e & \mathbf{F}^e \\ \mathbf{F}^{e,T} & \mathbf{H}^e \end{bmatrix}_{n+1}^{(i)} \begin{pmatrix} \Delta\mathbf{u}_{n+1}^e \\ \Delta\boldsymbol{\alpha}_{n+1}^e \end{pmatrix}^{(i)} = \begin{pmatrix} \mathbf{f}_{n+1}^{ext,e} - \mathbf{f}_{n+1}^{int,e,(i)} \\ \mathbf{h}_{n+1}^{e,(i)}(=0) \end{pmatrix} \tag{3.36}$$

with the matrices

$$\begin{aligned} \mathbf{K}_{n+1}^{e,(i)} &= \left(\frac{\partial \mathbf{f}^{int,e}}{\partial \mathbf{u}}\right)_{n+1}^{(i)} = \int_0^{l^e} \mathbf{B}^T \mathbf{C}_{n+1} \mathbf{B} dx, \\ \mathbf{F}_{n+1}^{e,(i)} &= \left(\frac{\partial \mathbf{f}^{int,e}}{\partial \boldsymbol{\alpha}}\right)_{n+1}^{(i)} = \int_0^{l^e} \mathbf{B}^T \mathbf{C}_{n+1} \overline{\mathbf{G}} dx, \\ \mathbf{H}_{n+1}^{e,(i)} &= \left(\frac{\partial \mathbf{h}^{e}}{\partial \boldsymbol{\alpha}}\right)_{n+1}^{(i)} = \int_0^{l^e} \overline{\mathbf{G}}^T \mathbf{C}_{n+1} \overline{\mathbf{G}} dx + \mathbf{K}_{\mathbf{s},n+1}^{(i)} \end{aligned} \tag{3.37}$$

where $\mathbf{K}_{\mathbf{s},n+1}$ is the $6x6$ matrix of consistent tangent stiffness components for the discontinuity (from eq. 3.26) where only first three diagonal members take non-zero values when the discontinuity is activated (see [Simo et al., 1993]). The static condensation (e.g. [Ibrahimbegovic and Wilson, 1991]) of system ought to be done in order to eliminate the incompatible mode parameters $\boldsymbol{\alpha}$ from global equations; this leads to the reduced size of stiffness matrix which is calculated as follows

$$\widehat{\mathbf{K}}_{n+1}^{e,(i)} = \mathbf{K}_{n+1}^{e,(i)} - \mathbf{F}_{n+1}^{e,(i),T} (\mathbf{H}_{n+1}^{e,(i)})^{-1} \mathbf{F}_{n+1}^{e,(i)}. \tag{3.38}$$

Such a reduced stiffness matrix can be sent to the standard finite element assembly procedure to provide global set of linearised equilibrium equations, compute incremental displacement $\Delta\mathbf{u}_{n+1}^{(i)}$ and perform corresponding displacement vector update

$$\begin{aligned} &A_{e=1}^{n_{el}} \widehat{\mathbf{K}}_{n+1}^{e} \Delta\mathbf{u}_{n+1}^{(i)} = A_{e=1}^{n_{el}} (\mathbf{f}^{ext,e} - \mathbf{f}^{int,e,(i)}) \\ &\Longrightarrow \mathbf{u}_{n+1}^{(i+1)} = \mathbf{u}_{n+1}^{(i)} + \Delta\mathbf{u}_{n+1}^{(i)}. \end{aligned} \tag{3.39}$$

2.7 The failure criteria

The 3D simulation of propagation of cracks subjected to shear and tensile stresses is a very challenging task in fracture mechanics of rocks with material heterogeneities. Failure of each element can occur in modes I, II or III, as well as in their combination. Namely, the combination of modes I, II and III occurs more frequently than any pure mode alone, when cracking process is active. First approach of the model is when full stress reduction is done with simultaneous softening, which is suitable for tension applied area of the

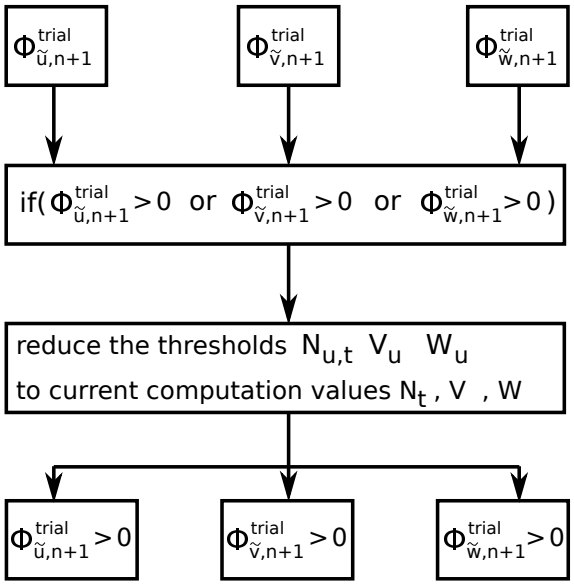

Figure 3.5: Tension failure flow chart

rock. The three trial failure surfaces regarding three directions of local frame are defined in order to activate softening behaviour in tension case

$$\begin{aligned} \Phi^{trial}_{\tilde{u},n+1} &= t^{trial}_{\tilde{u},n+1} - (N_{u,t} - q_{\tilde{u},n}) \\ \Phi^{trial}_{\tilde{v},n+1} &= \left| t^{trial}_{\tilde{v},n+1} \right| - (V_u - q_{\tilde{v},n}) \\ \Phi^{trial}_{\tilde{w},n+1} &= \left| t^{trial}_{\tilde{w},n+1} \right| - (W_u - q_{\tilde{w},n}) , \end{aligned} \tag{3.40}$$

where $N_{u,t}$, V_u and W_u are limit values. The trial failure surface is active if it takes greater than zero value and non-active if it takes less or equal to zero value. In tension case the first failure surface in (3.40) that becomes active simultaneously activates the other two surfaces, which leads to full stress reduction of the softening element. Namely, as soon as one failure surface becomes active, the threshold for other surfaces decrease to current values of local forces, and thus at the same time step all three failure surface becomes active (see Figure 3.5).

Second approach of the model is meant for compression case and includes separated softening case. Namely, the modes of failure are independent of each other and compression force can still increase if the shear sliding along the cracks is presently happening and embedded discontinuity for modes II or III is activated. Moreover, the compression force influences the failure threshold for shear sliding with Mohr-Coulomb friction law:

$$V_u = V_f + Ntan(\phi); \;\; W_u = W_f + Ntan(\phi) \tag{3.41}$$

and it magnifies the shear strength. The V_u and W_u represent ultimate shear forces corresponding to current compression force, and ϕ is the angle of friction. The V_f and W_f are the threshold values when compression force takes zero value. Such a representation allows to account for further dissipation in frictional sliding along activated crack.

As seen in eq. (3.41), the compression force increase influences the shear failure modes. However, the compression force increases until the significant damage is introduced to rock material and until sliding is already extensive enough that loading capacity of element starts to decrease. Thus, the significant damage of material activates the softening in compression mode as well:

$$\begin{aligned}\Phi^{trial}_{\tilde{u},n+1} &= \left|t^{trial}_{\tilde{u},n+1}\right| - (N_{u,c} - q_{\tilde{u},n}) \\ \Phi^{trial}_{\tilde{v},n+1} &= \left|t^{trial}_{\tilde{v},n+1}\right| - (V_u - q_{\tilde{v},n}) \\ \Phi^{trial}_{\tilde{w},n+1} &= \left|t^{trial}_{\tilde{w},n+1}\right| - (W_u - q_{\tilde{w},n})\end{aligned} \tag{3.42}$$

The $N_{u,c}$, V_u and W_u are elastic limit points in compression case. The number of activated failure surfaces from eq. (3.42) leads to two possible crack propagation mechanisms: either only one failure surface is activated which leads to cracking in only one pure mode; two or even three surfaces can be activated leading to mixed mode.

3 Numerical examples

In this section, the results of several numerical examples illustrating the performance of the model are presented. The series of beam failure tests in different modes are performed illustrating the capabilities of proposed beam with embedded discontinuities. Furthermore, standardized rock specimens are constructed as an assembly of Voronoi cells held together by beams and subjected to uniaxial tests and compared to the experiment. The novel model formulations are implemented into the research version of the computer code FEAP, developed by R.L. Taylor [Taylor, 2011].

3.1 Embedded discontinuity beam test

The beam of circular cross section is fixed at the one end, and subjected to imposed displacement on the other end. The chosen geometric properties of the beam are $l = 0.8cm$, $d = 0.55cm$, where d is diameter of cross section and other corresponding beam section properties are computed from diameter. The properties of the proposed beam material are: $E = 5000kN/cm^2$, $\nu = 0.2$, $\sigma_u = 17.2MPa$, $\tau_u = 28MPa$, $G_{f,u} = 45N/m$, $G_{f,v} = 1000N/m$. The σ_u and τ_u are the material ultimate stresses for tension and shear loading and $G_{f,u}$, $G_{f,v}$ are the fracture energies for pure mode I, and shear modes II and III. In order to avoid the ambiguity of the failure pattern under homogeneous stress applied to the beam elements, the slight imperfection is introduced into only one of them. This allows to avoid the academic case when the uniform load is applied to a series of homogeneous beam elements resulting in localized failure in different elements at the same time only decided by numerical round-off errors.

Figure 3.6. illustrates the response of the beam in pure shear and tension tests. It is observed that the model gives the mesh independent results when the imperfection is added to one of the beam finite elements and the exponential softening drives the beam

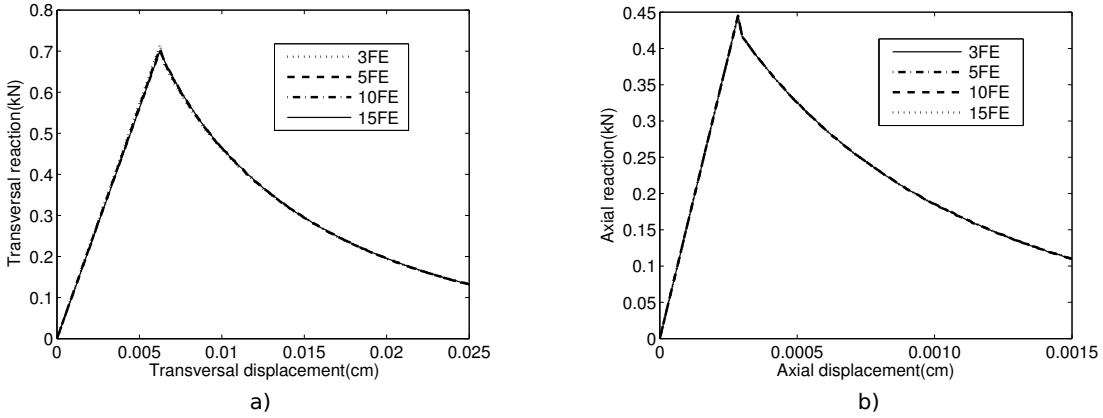

Figure 3.6: Beam under failure: a) pure shear test, b) pure tension test: imposed displacement vs. computed reaction

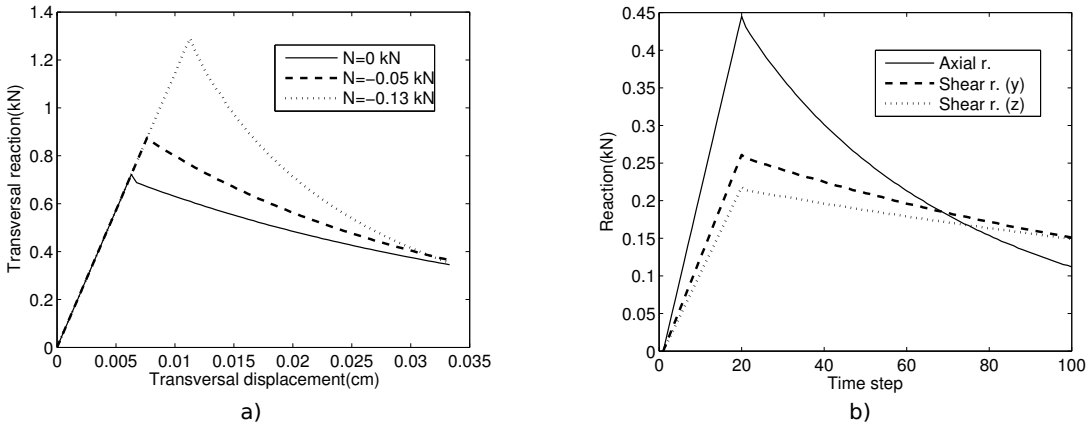

Figure 3.7: Beam under failure: a) Mohr-Coulomb law increasing the shear resistance under the compression force, b) simultaneous reduction of beam capacity under the tension force

to complete failure. Moreover, the proposed beam formulation can represent both ductile and brittle behaviour, depending on the chosen fracture energy.

Furthermore, the beam behaviour under the two different regimes explained in previous section is examined in the second numerical test on the beam. One regime is under the influence of compression force when the Mohr-Coulomb friction law is activated implying that the softening happens separately for each mode failure. The compression force increases the shear resistance threshold. Thus, although sliding along crack is taking place, the compression force can still increase and influence the sliding process. Figure 3.7.a shows the increase of shear resistance threshold under the different level of compression force.

The other failure regime is appropriate for tension tests, where softening happen simultaneously for all of the modes. The first failure surface from (3.40) activates the other

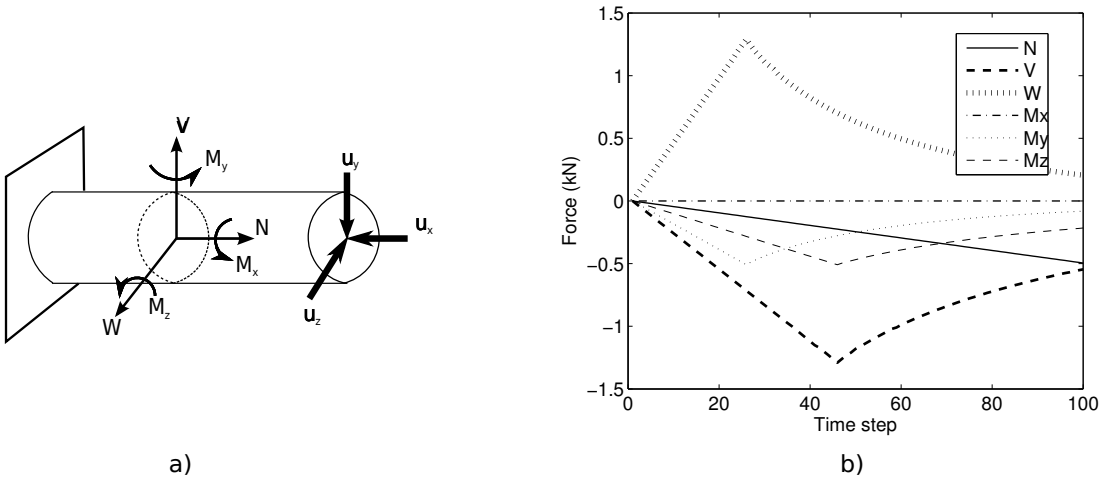

Figure 3.8: Beam under failure: a) displacement is imposed at the right end , b) internal beam forces with respect to time step

two failure surfaces as already elaborated in Section 3.7 and thus momentarily lead to complete failure of the element. This kind of regime happens in rocks under the ultimate tension force which is characterized by complete detaching of the blocks once the crack start to initiate. Figure 3.7.b presents the results of the test when axial tension force is dominant. It can be observed that as soon as tension force reaches its limit point, the ultimate shear resistance values take the current force values and softening starts at the same time (same time step) for all modes.

The third test is performed on a beam where the displacement is imposed at the free end in all three coordinate directions thus leading to activation of modes II and III under the compression force. The final values of imposed displacements in [cm] completed linearly through 100 time steps are: $u_x = -0.00032$, $u_y = 0.045$, $u_z = 0.025$. The internal forces of beam are then monitored and presented in Figure 3.8. The compression force increases through the whole loading program, while the activation of embedded discontinuities for shear failure happens in both modes. Moreover, the internal beam moments M_y and M_z reduce at the same time step when the corresponding shear force start to decrease, although the discontinuity is not embedded for rotations. The reduction of the values of internal moments are indirectly influenced by the embedded discontinuities in shear modes.

The proposed algorithm shows the quadratic convergence in the softening behaviour. Convergence in a typical nonlinear softening time step for the third beam example, where mixed mode failure happen under the influence of compression force and Mohr-Coulomb law, is presented in Table 3.1.

Iteration number	Relative residual norm
1	8.8590270E-01
2	3.4836009E-04
3	8.4321223E-09
4	1.3142199E-15

Table 3.1: Convergence of the Newton-Raphson procedure in a typical softening time step (t=55) for mixed mode beam failure

3.2 The construction of rock specimens

The cylindrical rock specimens are constructed as an assembly of Voronoi particles held together by beams with circular cross-sections. The specimen dimensions are: diameter 5.5 *cm* and the height 13 *cm*. The beams are generated by computing the 3D Delaunay triangulation which is performed by *Gmsh* [Geuzaine and Remacle, 2009] over the spatial domain of interest. The edges of the produced tetrahedral elements are converted into the beams whose diameters are computed from the corresponding Voronoi tessellation. Namely, the common area of the two neighboring Voronoi cells is used to compute the single beam diameter, from which the beam cross-section parameters are obtained. Such task is carried out by *Qhull* [Barber et al., 1996], the code that computes the convex hulls, Delaunay triangulations and Voronoi diagrams.

3.3 Rock specimen under uniaxial (unconfined) compression and tension test

In order to evaluate the numerical model against experimental result, the first specimen (intact specimen named *type A*) is subjected to uniaxial compression test with no lateral confinement. The friction at the load platens is not considered in the present numerical simulations. The three different meshes are constructed for *type A* specimen: coarse, fine and the finest (Figure 3.9). The experiment is conducted at the accredited Geotechnical laboratory of Institute IGH, Croatia [Stambuk-Cvitanovic, 2012], where the series of 43 intact limestone samples are examined in the uniaxial (unconfined) compression tests.

The investigation was focused on the mechanical properties of intact rock and the unavoidable, but insufficiently investigated effects on these properties that appear in testing and can significantly affect the results. Namely, within the 43 limestone samples which have been experimentally examined, the following mean values are obtained: elastic modulus $E = 50.3\ GPa$, Poisson's ratio $\nu = 0.25$, tensile strength $\sigma_{u,t} = 12.8 MPa$, compressive strength $\sigma_{u,c} = 127.8 MPa$, shear strength $\tau_u = 25.3 MPa$ and angle of friction is $\phi = 35^\circ$. The dispersal of the experimental results is well correlated with the Gaussian distribution with the standard deviation of 4% [Stambuk-Cvitanovic, 2012]. Thus, the variability of material parameters is also introduced into the numerical model through the Gaussian distribution. The same parameters obtained from the experiments are used for the model input values. Furthermore, the values of fracture energies have not been the topic of

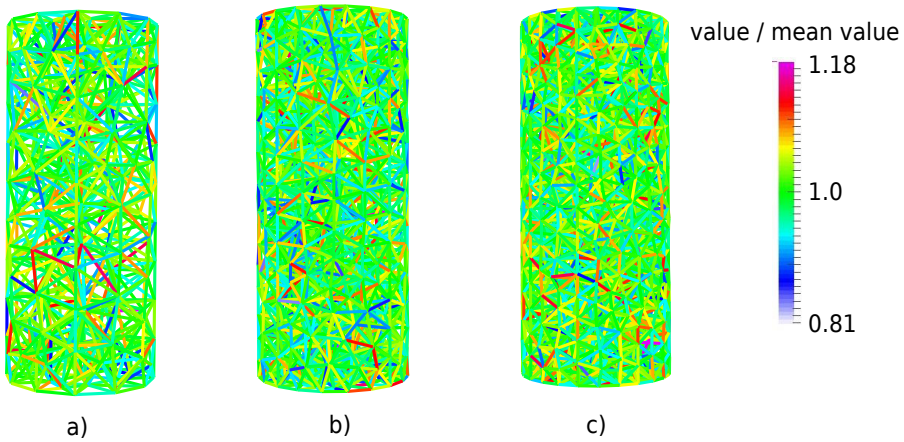

Figure 3.9: *type A* specimen in three different mesh versions: a) coarse (1407 beam elements), b) fine (4398 beam elements), c) finest (6508 beam elements). The different input parameter values across the mesh are shown.

interest in the experimental analysis. Thus, the following values have been used in this numerical tests: $G_{f,u} = 20N/m$, $G_{f,v,w} = 600N/m$, along with the corresponding variability. In order to evaluate the geometric parameters of specimen, as well as computed beam cross-section parameters, the proposed lattice model is also compared to corresponding solid model with tetrahedral elements with the same material properties. The results of the uniaxial compression test are shown in Figure 3.10.

The computed macroscopic response of numerical test for *type A* specimen matches with the experimentally obtained result. The numerical test is conducted with imposed displacement control, where the load is linearly increased. The post-peak behaviour is very brittle for the limestone material, which is also obtained with the numerical model. Furthermore, the numerically obtained result matches with the solid model in linear elastic regime showing that the beam lattice parameters are correctly taken into account. Very close macroscopic curves are also obtained for three different choices of the finite element mesh. However, the more brittle response is obtained for coarser meshes, where the slight difference is brought by the choice of initial heterogeneities in the rock specimens. In Figure 3.10.b, the crack opening is shown at the end of numerical test. It is observed that the lower part of specimen is mostly affected with cracking and that the cracks are irregular throughout the specimen, which is a result of heterogeneity introduced through the Gaussian distribution of material parameters. The amount of crack opening is large showing the significant damage on the examined specimen after the conducted numerical experiment.

The failure mechanism obtained with the numerical model also corresponds to the experiment (Figure 3.11.a), where the detachment of the material happens due to the dominant influence of the shear failure. Figures 3.11.a and 3.11.b reveal the two different specimens tested with the same equipment. It is clear that the failure mechanism depends on the heterogeneities in rock. Figure 3.10.c presents the distinction between the failed

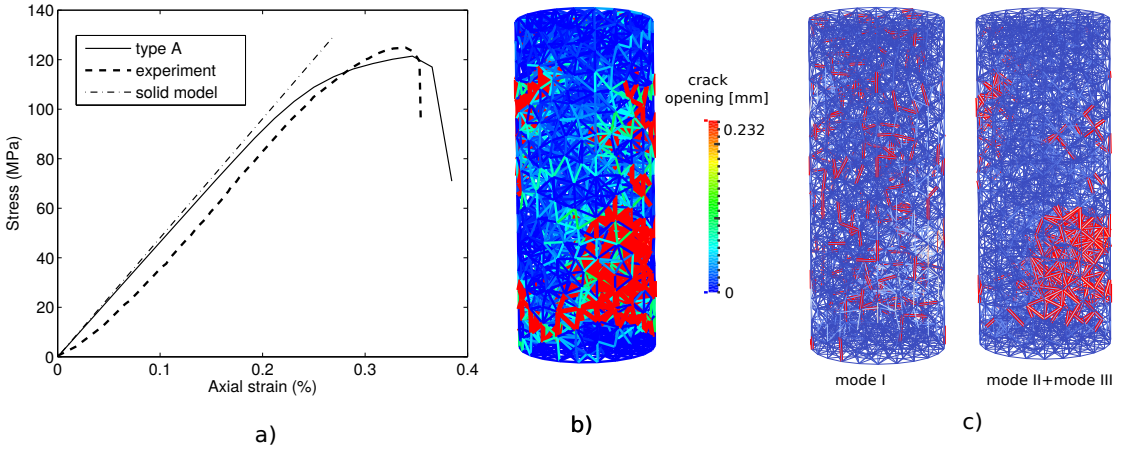

Figure 3.10: Uniaxial (unconfined) compression test: a) computed macroscopic response for *type A* specimen compared to solid model and experiment , b) crack opening (presented as euclidean norm of all three failure modes) at the end of numerical test for *type A* - finest, c) red marked elements are broken elements due to: mode I, modes II and III

elements in mode I, and failed elements in shear modes II and III. It can be seen that failure in unconfined compression test happen largely under the influence of shear failure, while the mode I failure is still significant. Large number of elements are also broken due to mixed mode failure and these overlap on the two pictures in Figure 3.10.c. It is interesting to note that the seeding of pre-existing heterogeneities makes the computational procedure more robust. Namely in the homogeneous state, any particular element can be the first to reach the ultimate stress state and enter the subsequent softening phase. The practical solution is to introduce the perturbation with the spatially distributed material heterogeneities, which also physically correspond to the rock structure.

Next, the *type A* specimen is numerically subjected to unconfined tension test and the macroscopic curve is shown in Figure 3.12.a. The material in compression test was much more resistant than in tension, due to the Mohr-Coulomb law inducing shear strength threshold, where shear resistance increases along the compression force increase. The crack pattern obtained in unconfined tension test is different than in unconfined compression, and the one dominant macro-crack propagated through the upper part of specimen.

3.4 Influence of pre-existing defects

Rock is a heterogeneous material containing many initial cracks, voids or other defects. When the external load is applied to such a material, the micro-cracks initiating from pre-existing flaws and their coalescence into macro-cracks, lead to total failure. To examine the influence of pre-existing cracks and defects, four new specimens are considered (see Figure 3.13).

The grey coloured elements in Figure 3.13. represent the pre-existing defects of the specimen. First two specimens from the Figure 3.13 (*type B* and *type C*) contain the loc-

a) b)

Figure 3.11: Failure mechanism for two specimens obtained within the experiment: a) the detachment of the material is noticed at the lower part of the specimen, b) the diagonal failure is pronounced

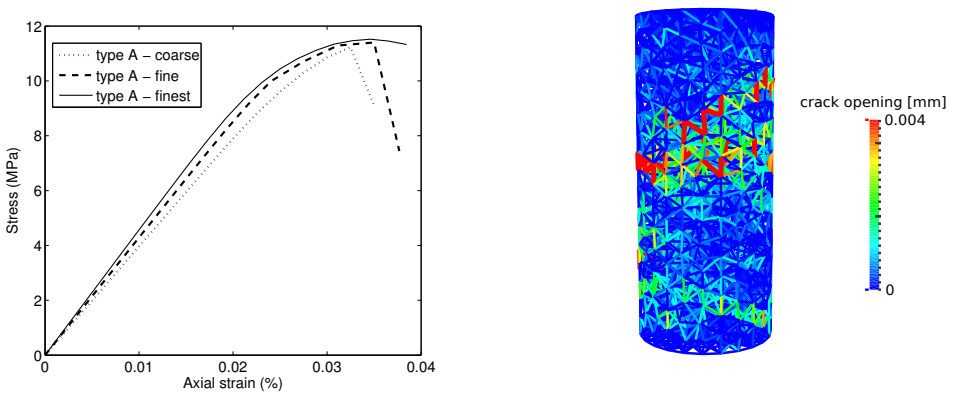

a) b)

Figure 3.12: Uniaxial (unconfined) tension test: a) computed macroscopic response for *type A* specimen, b) crack opening (presented as euclidean norm of all three failure modes) at the end of numerical test for *type A* - finest

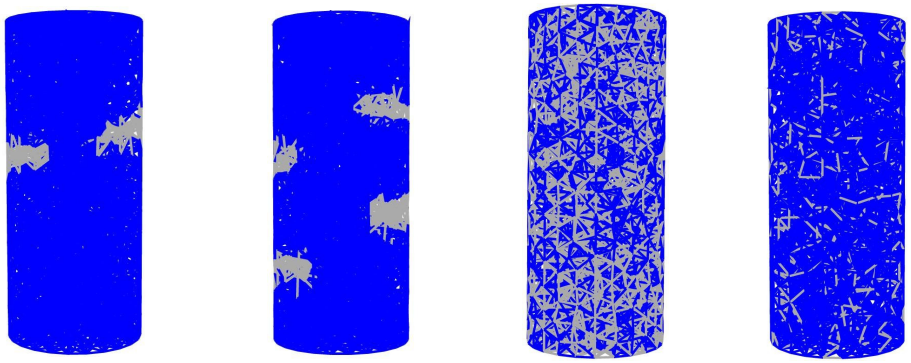

type B *type C* *type D* *type E*

Figure 3.13: Four heterogeneous specimens with initial pre-existing defects. The grey coloured elements represent the initial defects

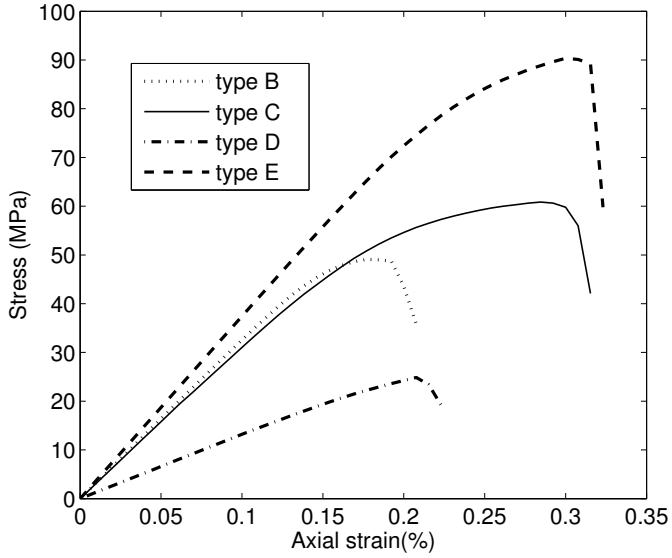

Figure 3.14: The computed macroscopic response for 4 different heterogeneous specimens under uniaxial compression test

alized defects that are manually positioned in the specific part of specimens. The *types D* and *E* contain the randomly distributed defects throughout the specimen. Such a choice lead to 2-phase specimens ([Ibrahimbegovic and Matthies, 2012, Feng et al., 2014]) where phase I elements represent the intact rock parts and the phase II pre-existing defects. Phase I elements keep the same material parameters as *type A* specimen, while the phase II have the negligible properties compared to phase I. Namely, the phase II material properties are: $E = 0.1\ GPa$, $\nu = 0.25$, $\sigma_{u,t} = 0.01MPa$, $\sigma_{u,c} = 0.1MPa$, $\tau_u = 0.01MPa$. All four specimens are subjected to unconfined compression test with the results presented in Figure 3.14.

It can be seen from Figure 3.14. that the overall global mechanic properties depend upon the position and the amount of pre-existing defects. Not only that the overall compression resistance changes, but also the global modulus of elasticity. All of the four specimens with pre-existing defects have the lower resistance than intact *type A* specimen without pre-existing defects. As soon as the defects are present, the resistance to compression decreases. *Type E* turns out to be the most resistant due to the lowest amount of pre-existing defects and its random distribution through the specimen. The least resistant specimen *Type D* is the specimen with most defects compared to others. *Type B* and *type C* specimens have somewhat lower resistance than *type E*. Similar number of phase II elements are present in *types B*, *C* and *E* but their distribution is different which allows for *types B* and *C* to develop instantly the cracks that lead the specimen to instant failure.

The unconfined compression test of *type C* specimen is performed with the displacement control within 40 time steps. This specimen is constructed with four pre-existing flaws positioned on the opposite sides. The crack evolution is monitored during the nu-

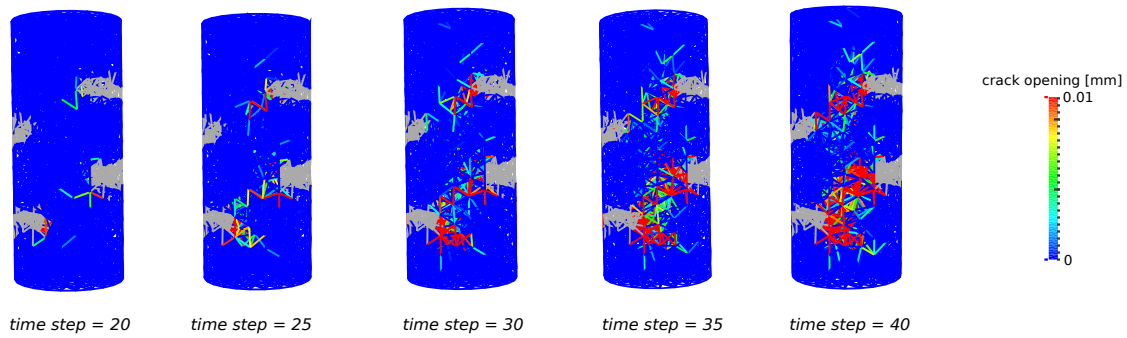

Figure 3.15: Uniaxial compression test - *type C*: progressive crack propagation shown through the different stage of numerical test

merical test and the state of the specimen throughout the test is presented in Figure 3.15. The cracks initiation from the pre-existing defects and coalescence into the final cracking through the specimen, leads to brittle failure.

4 Final comments on the presented 3D rock mechanics model

A novel three-dimensional beam lattice model is presented capable of representing the failure modes of brittle heterogeneous material like rock. Rock material is considered as an assembly of mineral grains represented by the 3D Voronoi cells, held together by cohesive forces represented by Timoshenko beams. The main feature of the model is that the 3D Timoshenko beams (with 6 dofs per node, 3 translations and 3 rotations) are embedded with strong discontinuities in local coordinate system directions which provides the capability to simulate the localized failure in modes I, II and III. The micro-crack propagation can happen in all three modes individually, but it can also progress in mixed-mode. The beam enhancements provide the possibility of simulating the spatial evolution of cracks in three-dimensional space, which is the main characteristic of brittle failure of rocks under external load. The failure criteria are different when tension or compression force is active. In compression applied area, the failure modes are handled separately. Moreover, the compression force can increase although the shear failure modes are active. The compression force influences the shear strength threshold in Mohr-Coulomb way. On the other hand, the tension force imply simultaneous softening for all modes as soon as one failure surface becomes active. Another feature of the model is that there is no need to introduce and predict the first cracks to break the specimen, but instead the Gaussian statistical variation is used for the mechanical properties of the each element. Thus, the model is able to capture the heterogeneous properties of rocks, which can influence the initial phase of crack evolution.

The series of uniaxial tests are performed on different rock specimens. Numerically simulated intact rock specimen under uniaxial (unconfined) compression test is in agree-

ment with experimentally obtained results. The simulated crack pattern at the end of test show significant damage on the rock specimen. It is also shown that this crack pattern developed as the consequence of all three modes. Moreover, the shear modes II and III were more pronounced in unconfined compression test. The same specimen is subjected to unconfined tension test. The resistance to tension is much lower than for compression and the failure pattern shows significant damage at the specimen contour. However, unlike in unconfined compression, unconfined tension test produces less profound macro-cracks. Here, one dominant macro-crack leads the specimen to failure.

Four specimens with pre-existing defects are further examined in the series of unconfined compression tests. It is shown the pre-existing defects and flaws largely influence the overall response. The specimen with specifically positioned flaws (on the opposite sides of specimen) is examined and internal crack evolution process is successfully simulated. The cracks initiate from the introduced defect areas and propagate towards other weak parts forming the global failure mechanism.

The proposed model takes into account many complex phenomena that happen under the failure of rocks. The algorithm for 3D embedded discontinuities is precisely developed and presented in detail. The model can also be used for other heterogeneous materials where localized discontinuities influence the behaviour of the material.

Chapter 4

Influence of specimen shape deviations on uniaxial compressive strength

In this chapter, the influence of intact rock core specimens shape deviations on uniaxial compressive strength is studied.

Contents

1 Research motivation

Conducted research presented in [Stambuk-Cvitanovic, 2012] discovered some surprising results within the aspects of rocks that have already been addressed and even included in the norms, but not truly examined in detail. Namely, the influence of initial test specimen shape deviations on the uniaxial compressive strength (UCS) of intact rock can be significant. Moreover, it was shown that the latter should be objectively evaluated and controlled in testing. Although this topics was already investigated, little data on this specific subject has been published since the 1970s.

Initial specimen shape deviations can be considered as inaccuracies that appear during the preparation of cylindrical specimens in the forms of 'micro' deviations from flatness, perpendicularity and parallelism. The latter typically influences the 'macro' properties, including the UCS. The effects of specimen side straightness, ends flatness, ends parallelism and perpendicularity to the specimen axis on UCS and stress-strain curve have been measured in several actual ways and examined on approximately 90 homogeneous specimens taken from limestone rock. This research refers to limestone and similar rocks with uniaxial compressive strength ranging from 100 to 150 MPa.

The observations and the results from [Stambuk-Cvitanovic, 2012] was further confirmed by a 3D numerical model which is presented in Chapter 3 of this thesis and in [Nikolic and Ibrahimbegovic, 2015]. The cumulative results were joined in a work with an aim to examine what is the true effect of specimens shape deviations in subsequent testing of UCS for the limestone and rocks of similar strength, and to answer the question how and to what extent (non-)flatness, (non-)parallelism and (non-)perpendicularity of cylindrical sample affect the change of UCS. The final goal is to achieve optimization and control over the influence of test specimens (their shape deviations and shape tolerances) in further testing.

This cumulative research has been published in [Stambuk-Cvitanovic et al., 2015], while the numerical aspects are covered in the next sections of this Chapter. This includes the methodology of how to deal with geometrical micro-deviations of the intact specimens and corresponding numerical results.

2 Preparation of specimens with targeted shape deviations

Special equipment was developed and implemented in the laboratory for the recording of surface profiles along chosen directions on side and ends of specimen (device for automatic recording and verification of specimens in rock mechanics, patent pending).

For investigation purposes the block of rock was selected (island of Brač, Croatia), with no visible cracks and structural phenomena of stratification, where ninety usable test specimens were drilled from these blocks.

To achieve and verify a target specimens shape deviations, specimens were distributed into groups shown schematically in Figure 4.1.

Samples of group ID ('ideal') were made without shape deviations, or formed with

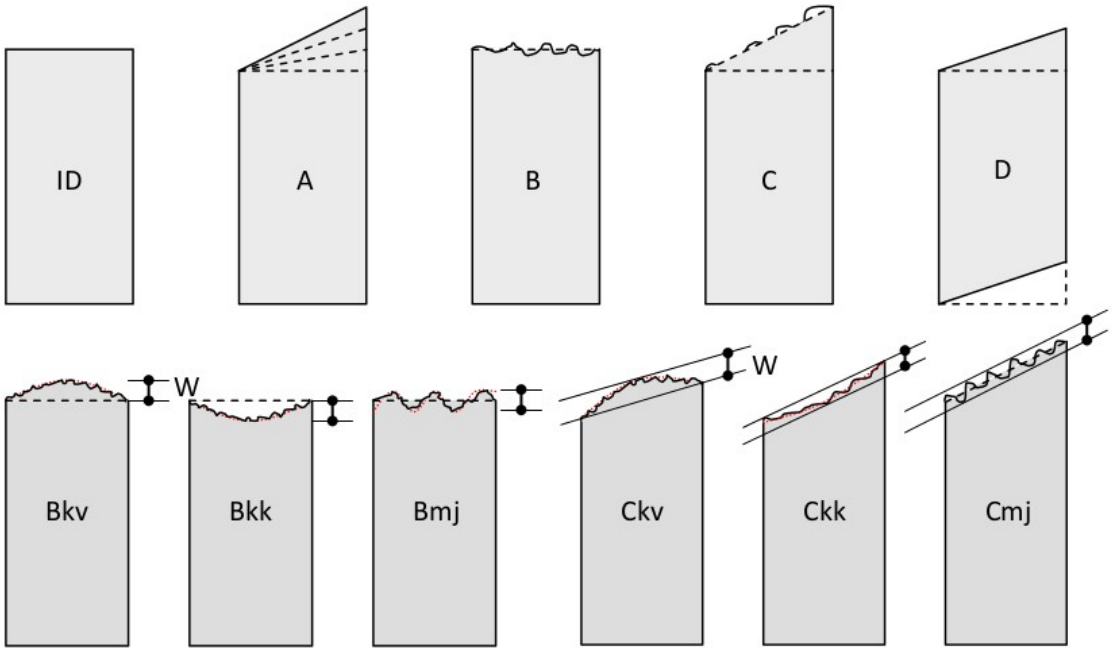

Figure 4.1: Groups of the specimens shape deviations

minimal irregularities which did not affect the mechanical properties.

Group A consisted of specimens that were intentionally made only with non-parallelism of upper end, while other types of deviations were kept at small values as ID. By increasing the upper end slope in the grinding phase, angular difference of the upper and lower end slopes was varied from 0.2°to 2°.

For samples produced for the B group, the only shape deviation was non-flatness of the upper end. Height of the surface profile W ranged from 0.03 mm to about 0.5 mm. In order to assess the impact of type of waviness, surface profiles were intentionally formed (by a combination of manual and machine treatment) and further separated as convex (Bkv), concave (Bkk) or mixed-wavelike (Bmj).

Samples from group C were made in such a way that first the upper end was grinded flat with a slope of 0.5°to more than 2°. Then, on the upper end so obtained, different profiles were formed as convex (Ckv), concave (Ckk) and mixed (Cmj), similar to group B. W ranged from 0.04 to about 0.3 mm.

Group D comprised specimens with perpendicularity deviation of the lower end to the axis of the specimen from 0.2°to over 2°. Ends were prepared as flat and parallel.

3 Numerical model

Numerical model used herein is the 3D rock mechanics model already presented in this thesis. However, In order to obtain the proper influence of these slight deviations to the

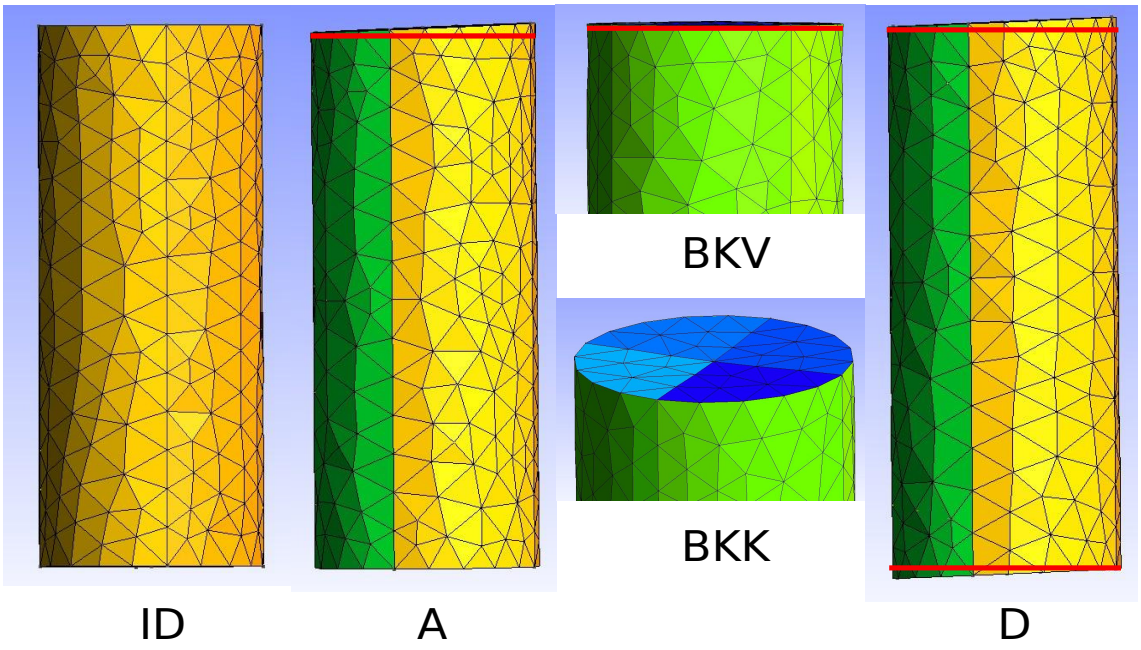

Figure 4.2: Numerically simulated groups of the specimens shape deviations

behaviour of the specimens, the penalty contact was added to the original presentation of the model.

Groups ID, A, Bkk, Bkv and D specimens are prepared (Figure 4.2). However, the roughness of the surface is not taken into account and the contact at the load platens is frictionless. Thus, only the geometry of deviations is considered. The penalty parameter is chosen to be the same in all of the conducted numerical tests: p=5000 GPa. Numerical analysis performed in [Zivaljic et al., 2014] showed that the value of penalty parameter chosen as $p = 100 \cdot E$ reduces the relative displacement error below 1%. The initial geometrical deviations of numerical specimens are constructed within the Gmsh mesh manipulation tool. The deviations for groups A and D are constructed such that the bases of the specimens are inclined by a desired angle. Group Bkk is also constructed completely by Gmsh and the curvature of the base is defined inside the mesh tool. For the group Bkv additional manual interference is needed. It has been observed that the macroscopic curve for latter group depends on the size of plateau that overlaps with the pressure platen at the beginning of the test. Since all of the deviations of experimental specimens are monitored, these data are used to reconstruct the numerical specimens shape deviation in the case of group Bkv.

All of the numerical tests are performed incrementally, while in each incremental time step iterative procedure is conducted. The loading program is increased linearly until the specimen is broken. The load, imposed displacement is applied at one end of the specimen, while the reaction is monitored on the other end.

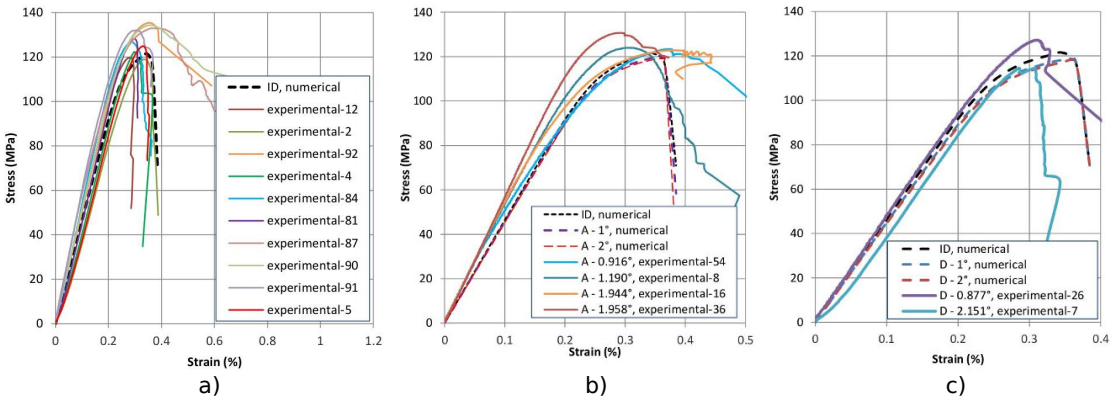

Figure 4.3: Results for the groups: a) ID, b) A, c) D

4 Numerical results

A control group consisted of 19 'ideal' shaped specimens (ID). Examples of stress-strain diagrams are given in Figure 4.3.a , where numerical result fits well among 10 experimental curves.

Effect of non-parallelism was observed within the group A. For the larger values of non-parallelism, deviation is so pronounced that it is visible to the naked eye. Even in such circumstances with the slope of upper specimen end of 2°, self-adjusting joint adjusts to the inclination of the upper end without difficulty and testing flow is generally quiet, with smooth curves. Numerical results for P=1°and P=2°(presented together with experimental results in Figure 4.3.b also show very similar UCS values and stress-strain curves to the ID numerical specimen with P=0°, and there is no greater loss of strength due to this kind of shape irregularity.

The effect of non-perpendicularity was observed within the samples of group D, which were made as flat specimens of parallel ends, with a growing slope of the lower end as the only present shape deviation. The resulting curves are given in Figure 4.3.c. Numerical results for non-perpendicularity of 1°and 2°fit to experimental results and ID numerical results, and there are no greater changes of UCS.

Impact of non-flatness was investigated through the group B. Failure in group B depends on waviness profile type: for Bkv type pushing of upper cone inside, vertical splitting outside, and local crushing of the remaining higher edge of the upper end is registered; for Bkk type local fracture in the form of chamfered edge. The results for this group are presented in Figure 4.4.

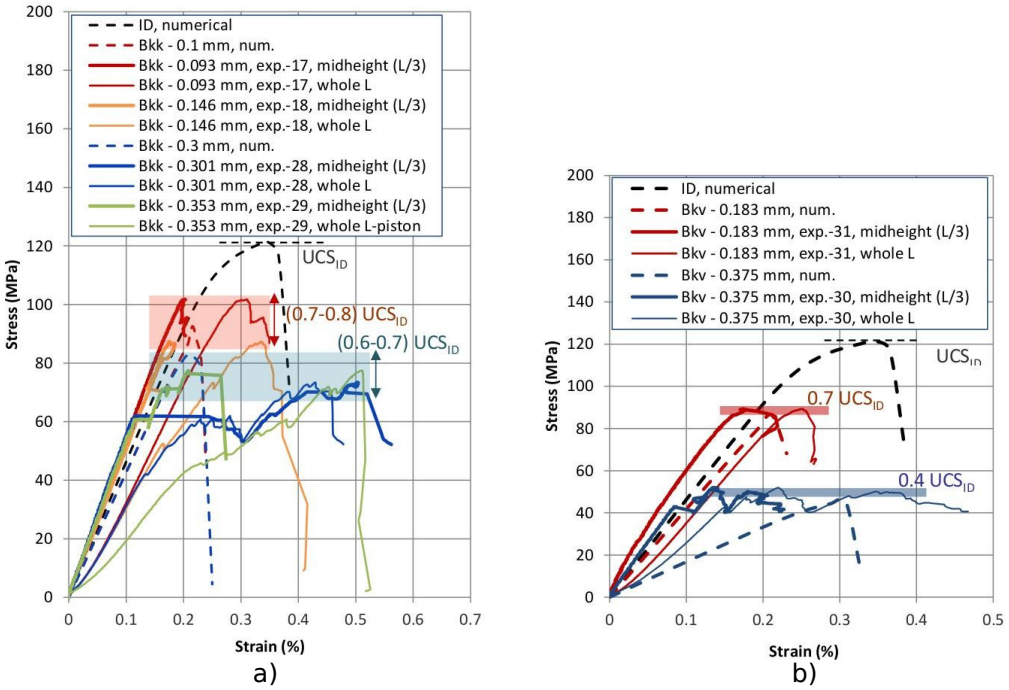

Figure 4.4: Results for the groups: a) Bkk, b) Bkv

5 Final comments on research of shape deviations influence to the UCS

The research program on 90 homogeneous specimens was conducted to examine what is the true effect of specimens shape deviations in subsequent testing of UCS for the limestone and rocks of similar strength.

Novel 3D rock mechanics model developed in this thesis, enhanced with penalty contact elements, was used to simulate and to examine the uniaxial compressive strength of intact rock core specimens with initial geometrical shape deviations.

The numerical results of conducted analysis are in agreement with experimental results. Moreover, it has been shown that unconfined compressive strength UCS does not depend on the angle shape deviations of parallelism and perpendicularity. Contrary, larger amounts of non-flatness significantly influence the UCS.

Full research on this topic can be found in [Stambuk-Cvitanovic et al., 2015].

Chapter 5

2D Rock mechanics model for the analysis of fluid-saturated fractured poro-plastic medium

In this chapter, a discrete beam lattice model capable of simulating localized failure in a heterogeneous fluid-saturated poro-plastic solid is presented. Coupling conditions between the solid and fluid phase are governed by the Biot's poro-elastic theory along with the fluid flow through cracks. The basis for development of discrete 2D (plane strain) model representation of heterogeneous material consisting of material grains, is an assembly of Voronoi cells that are kept together by cohesive links in terms of Timoshenko beams. Localized failure of saturated medium is enabled through embedded discontinuities positioned in cohesive links where Timoshenko beam's longitudinal and transversal directions posses enhanced kinematics resulting in failure modes I and II. The model can also properly take into account the fracture process zone with pre-existing microcracks coalescence prior to the localized failure, which is considered through the standard poro-plasticity formulation. Fluid flow is spread across the lattice network by Darcy's law in terms of continuous pore pressures, where special care is taken in computing the lattice permeability parameters. Several numerical simulations are given to illustrate the performance of the presented discrete model.

Contents

1 Model introduction

The flow of the fluid through the deformable porous medium, like rock or soil, modifies its mechanical properties and response with two coupling mechanisms playing a key role in this volumetric fluid-structure interaction problem. The first considers the change (increase) of pore pressure inducing the material dilation and the second considers the compression applied to such a material leading to an increase of a pore pressure if the overall conditions are undrained and also making the material less compliant than in the case of drained state. This topic has received a great attention in engineering sciences starting with the pioneering works of Terzaghi [Terzaghi, 1943] and Biot [Biot, 1965], and more recent overall contribution [Lewis and Schrefler, 1998] including numerical solution procedure for coupled thermo-hydro-mechanical problems in porous media.

The problem of interest in this paper involves the fluid-saturated porous solid and the potential development of the localized failure zones. The problems of this kind are many in civil engineering practice including the dam failures, collapse of foundations, the stability of excavations, slopes and tunnels, stabilizing the landslides, rock falls etc. Another applications where volumetric fluid-structure coupling plays an important role are oil and gas extraction by fracking, nuclear waste disposal, deep well injections of liquid or solid waste etc. The risk of localized failure that occurs in these engineering problems should be better understood in order to be prevented. However, for some applications, the localized failure of soil with macro-cracks needs to be induced. The latter is the case for oil and gas extraction with fracking or hydraulic fracturing [Secchi and Schrefler, 2014]. The simulations stand as significant tools for obtaining more insight into the full control of these applications.

Several recent attempt simulations of the behaviour of porous media with a discrete fractures and remeshing approach and automatic mesh refinement is used by Schrefler et al. [Schrefler et al., 2006]. This approach has been extended to 3D situation in [Secchi and Schrefler, 2012]. Extended finite element method (X-FEM) without the need for remeshing has been used in simulating hydraulic fracturing of fully-saturated [Rethore et al., 2007] and partially-saturated [Rethore et al., 2008] porous media with cohesive cracks, as well as in saturated shear band formations [de Borst et al., 2006]. Embedded discontinuity finite element method (ED-FEM) is an alternative approach to X-FEM, but with the main difference in the way of computing the unknowns related to discontinuity opening. Namely, the X-FEM solves them globally, together with the standard displacement unknowns. Contrary to X-FEM, ED-FEM uses the element-oriented local algorithm (operator split algorithm) for solution of discontinuity parameters, while at the global phase the remaining unknowns are nodal displacements. The fluid saturated poro-elastic and poro-plastic medium with localized failure zones have been simulated with ED-FEM in [Benkemoun et al., 2015, Callari and Armero, 2002], while the partially saturated medium can be found in [Callari et al., 2010].

In this chapter, a novel 2D model for localized failure in poro-plastic medium is presented. This model is also provided in [Nikolic et al., 2015b]. The proposed model is based upon discrete model for failure of rocks from previous chapters (without fluid

flow, further referred to as uncoupled model). The uncoupled model is based on discrete lattice approach where grains of rock are represented by Voronoi cells which are kept together by cohesive forces represented by Timoshenko beams. The latter are enhanced with additional kinematics modes that correspond to embedded strong discontinuities and enable the strain localization in the middle of the cohesive beam element, thus leading to discontinuity opening between the rock grains. The main strength of the proposed model is in representing the heterogeneous material properties which directly influence the formation of localized macro-cracks and make them geometrically irregular. The fracture process zone formation followed by micro-cracks coalescence precedes the localized failure. The fluid flow through the saturated porous domain with micro-cracks is governed by a diffusion equation incorporating the Darcy law. The coupled process between the deforming medium and fluid flow is governed by Biot's theory [Biot, 1965].

Since the uncoupled model relies on the lattice of beams, the special care must be taken for fluid flow that also needs to be spread throughout the lattice without loosing the precision compared to standard 2D flow. This is achieved by the computation of lattice permeability parameters which are in relation with given permeabilities. Moreover, the flow over the lattice is compared to the standard continuum flow simulated with CST elements within the numerical simulations.

2 The porous media formulation

In this section, the equations of the porous solid saturated with a fluid are presented. The flow conditions allows that convective terms and gravity acceleration be neglected in this problem. Standard equilibrium equation of two-phase medium is given by relation

$$\nabla \cdot \sigma = 0, \tag{5.1}$$

where the total stress is

$$\sigma = \sigma_s + \sigma_f = \sigma' - bp \tag{5.2}$$

and subscripts s and f denote the solid and the fluid part, respectively. The effective stress $\sigma_s = \sigma'$ measures the material properties of the solid skeleton under drained conditions, p is fluid pressure and b is Biot coefficient. The continuity equation for the fluid flow can be written as

$$\frac{\partial \zeta}{\partial t} + \nabla \cdot v_f = 0, \tag{5.3}$$

where ζ is the amount of fluid content which is defined as the variation of fluid volume per unit volume of porous material and v_f is the fluid flux. The fluid content reads

$$\zeta = \frac{1}{M} p + \alpha \nabla \cdot u_s, \tag{5.4}$$

where u_s represents the displacements of the solid and Biot's modulus M defined as

$$\frac{1}{M} = \frac{n_f}{K_f} + \frac{b - n_f}{K_s}, \tag{5.5}$$

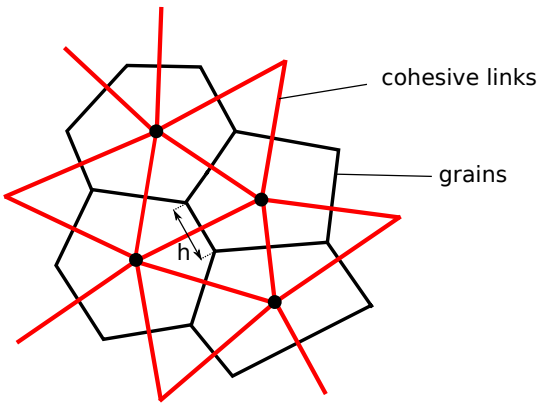

Figure 5.1: The basis of the proposed discrete model relies on the lattice of Timoshenko beams which represent the cohesive links keeping the rock grains (Voronoi cells) together.

where n_f denotes a porosity, K_f is the bulk modulus of the fluid, K_s is a bulk modulus of the solid and b is a Biot coefficient defined by

$$b = 1 - \frac{K_t}{K_s}. \tag{5.6}$$

The K_t is the overall bulk modulus of the porous medium. The inclusion of the fluid content (5.4) into the fluid continuity equation (5.3) results with

$$\frac{1}{M}\frac{\partial p}{\partial t} + b\nabla \cdot v_s + \nabla \cdot v_f = 0. \tag{5.7}$$

Vectors v_s and v_f represent the velocities of the solid and the fluid, respectively. The latter is defined by the Darcy law

$$v_f = -k_f \nabla p \tag{5.8}$$

where k_f is the permeability of the porous medium. The boundary conditions apply for both the solid and the fluid part of the coupled medium.

3 The discrete lattice model description

The main hypothesis in constructing the discrete lattice solid model, referred here by uncoupled model, is that the Voronoi cells which represent the rock grains connected by cohesive links taken as Timoshenko beams correspond to the representative part of the specimen (Figure 5.1).

The fluid flow equation is governed by the Darcy law in terms of continuous pore pressures across the discrete lattice domain (Figure 5.2). More precisely, the fluid flow is spread across the lattice of beams, where fluid pressure acts as additional degree of freedom of the beam. The uncoupled fluid flow across the lattice network is shown within numerical simulations section, as well as the choice of lattice permeability parameters.

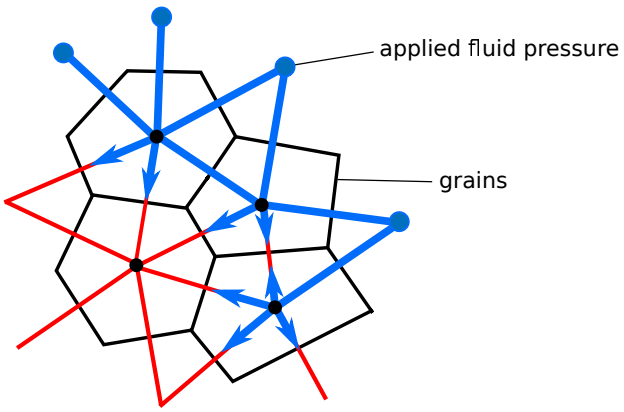

Figure 5.2: The fluid flow is dispersed across the lattice network of Timoshenko beams

3.1 The discrete lattice mechanical and fluid flow formulations

Let us consider the Timoshenko beam (cohesive link) of cross section area A and length l_e. The strong form equilibrium equation in (5.1) can be recast in terms of stress resultants

$$\begin{array}{l} \frac{dN}{dx} + f(x) = 0 \\ \frac{dT}{dx} + q(x) = 0 \\ \frac{dM}{dx} + T(x) + m(x) = 0 \end{array} \tag{5.9}$$

which also be expressed in terms of its weak form

$$\int_0^{l_e} \frac{d\mathbf{w}}{dx} \boldsymbol{\sigma} dx = \int_0^{l_e} \mathbf{w}\mathbf{f} dx + \mathbf{w}\mathbf{F}, \tag{5.10}$$

where $\boldsymbol{\sigma} = [N \;\; T \;\; M]^T$ represents the stress resultant vector, $\mathbf{f} = [f \;\; q \;\; m]^T$ is the distributed load vector and $\mathbf{F} = [F \;\; Q \;\; C]^T$ is the vector of concentrated forces. The right hand side in (5.10) provides the vector of external forces $\mathbf{F}^{ext}$ with the standard finite element manipulations. The vector $\mathbf{w}$ represents a virtual generalized displacements $\mathbb{V}_0 = \{\mathbf{w} : [0, l_e] \mapsto \mathbb{R} \;\; | \;\; [\mathbf{w}]_{\Gamma_u} = 0\}$, which ought to be differentiable and verify $\mathbf{w} \in \mathbb{V}_0$. The solid deformation is characterized by the Timoshenko beam strain displacements $\boldsymbol{\varepsilon}$ being a

$$\boldsymbol{\varepsilon}(x) = \begin{bmatrix} \varepsilon(x) = \frac{du}{dx} \\ \gamma(x) = \frac{dv}{dx} - \theta \\ \kappa(x) = \frac{d\theta}{dx} \end{bmatrix}, \tag{5.11}$$

where $\mathbf{d} = [u \;\; v \;\; \theta]^T$ is generalized displacement vector with its longitudinal displacement, transversal displacement and rotation. The constitutive relations for the saturated porous medium (5.2) are given in terms of total stresses, effective stresses and pore pressures $\boldsymbol{\sigma} = \boldsymbol{\sigma}' - b\mathbf{p}$. The total stress in terms of stress resultants can be decomposed into

$$\begin{bmatrix} N \\ T \\ M \end{bmatrix} = \begin{bmatrix} N' \\ T' \\ M' \end{bmatrix} - b \begin{bmatrix} pA \\ 0 \\ 0 \end{bmatrix}, \tag{5.12}$$

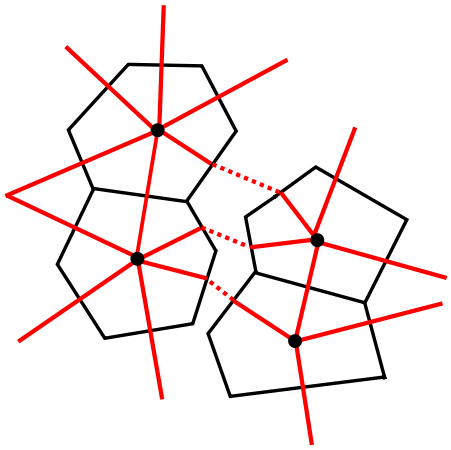

Figure 5.3: The strong discontinuity propagation between the Voronoi cells invokes the enhanced kinematics activation

where the effective stress resultant components can be obtained through the solid's skeleton 'drained' elasticities denoted with $\mathbf{D}_{sk}$

$$\begin{bmatrix} N' \\ T' \\ M' \end{bmatrix} = \underbrace{\begin{bmatrix} EA & 0 & 0 \\ 0 & GA & 0 \\ 0 & 0 & EI \end{bmatrix}}_{\mathbf{D}\text{sk}} \begin{bmatrix} \varepsilon \\ \gamma \\ \kappa \end{bmatrix}. \tag{5.13}$$

Note that E represents Young's modulus, G shear modulus and I moment of inertia of the beam.

Using the standard procedure of applying the integration by parts, using the external boundary conditions and applying the Darcy law for fluid velocities

$$v_f = k_f \frac{dp}{dx}, \tag{5.14}$$

the strong form equation from (5.7) takes the weak form for the discrete lattice representation of the domain

$$\begin{aligned} -\int_0^{l_e} \pi M^{-1} \frac{dp}{dt} dx + \int_0^{l_e} \frac{d\pi}{dx} \alpha \mathbf{v}_s dx + \\ + \int_0^{l_e} \frac{d\pi}{dx} k_f \frac{dp}{dx} dx = Q^{ext}, \end{aligned} \tag{5.15}$$

where π is the virtual pressure field that obeys the same regularity as the virtual displacement field.

3.2 The strong discontinuities in poro-elastoplastic solid

The discontinuous behaviour of the porous material is assumed through the activation of enhanced kinematics providing the displacement jumps inside the cohesive links shown in Figure 5.3.

In order to represent the mode I and mode II failure mechanisms between the Voronoi cells, the displacement discontinuity is added to the standard beam kinematics, resulting with displacement decomposition into regular and singular parts

$$\mathbf{u}(x) = \overline{\mathbf{u}}(x) + \boldsymbol{\alpha} H_{x_c} = \begin{bmatrix} \overline{u}(x) \\ \overline{v}(x) \\ \overline{\theta}(x) \end{bmatrix} + \begin{bmatrix} \alpha_u \\ \alpha_v \\ 0 \end{bmatrix} H_{x_c}, \tag{5.16}$$

where $\boldsymbol{\alpha} = [\alpha_u \;\; \alpha_v \;\; 0]$ represents the displacement jump at the discontinuity position (in the middle of the beam) and H_{x_c} is the Heaviside function defined by $H_{x_c}(x) = 0$ for $x \leq x_c$ and $H_{x_c}(x) = 1$ for $x > x_c$. The strain field is enhanced through the Dirac delta distribution resulting from a discontinuous displacement field

$$\boldsymbol{\varepsilon}(x) = \overline{\boldsymbol{\varepsilon}}(x) + \boldsymbol{\alpha}\delta_{x_c} = \begin{bmatrix} \overline{\varepsilon}(x) \\ \overline{\gamma}(x) \\ \overline{\kappa}(x) \end{bmatrix} + \begin{bmatrix} \alpha_u \\ \alpha_v \\ 0 \end{bmatrix} \delta_{x_c}. \tag{5.17}$$

The embedded strong discontinuities thus provide the discontinuous behaviour of the solid skeleton. The pore pressure field is assumed to remain continuous, apart the discontinuous gradients reflecting the localized fluid flow produced inside the crack representing the displacement discontinuity. The discontinuous flow gradients, affecting the fluid fluxes, pertain to the post-processing phase, while the computations include the continuous pore pressure field. Such an approach was adopted by [Callari and Armero, 2002, Callari et al., 2010] as well, with the motivation from the experimental tests which showed no 'pressure shocks' during the localization forming.

The constitutive relations of the elastoplastic solid skeleton including localization phase are presented next. Prior to the localized failure, formation of micro-cracks in the fracture process zone, is considered through the classical elastoplastic model. In seeking the compatibility between localized failure in modes I and II, the classical plasticity in fracture process zone is also introduced to the beam. In other words, the total regular strains can be additively decomposed into elastic and plastic components

$$\begin{aligned} \varepsilon &= \overline{\varepsilon}^e + \overline{\varepsilon}^p \\ \gamma &= \overline{\gamma}^e + \overline{\gamma}^p. \end{aligned} \tag{5.18}$$

Strain energy functions depend upon elastic strains and hardening variables, $\overline{\xi}_u$, $\overline{\xi}_v$

$$\begin{aligned} \psi_u\left(\varepsilon, \overline{\varepsilon}^p, \overline{\xi}_u\right) &= \frac{1}{2} EA\,(\varepsilon - \overline{\varepsilon}^p)^2 + \frac{1}{2}\overline{\xi}_u^2 \overline{K}_u \\ \psi_v\left(\gamma, \overline{\gamma}^p, \overline{\xi}_v\right) &= \frac{1}{2} GA\,(\gamma - \overline{\gamma}^p)^2 + \frac{1}{2}\overline{\xi}_v^2 \overline{K}_v, \end{aligned} \tag{5.19}$$

where $\overline{K}_u$ and $\overline{K}_v$ denote isotropic hardening moduli for longitudinal and transversal directions. The yield criteria for the same are defined as

$$\begin{aligned} \overline{\Phi}_u\,(N, \overline{q}_u) &= N - (N_y - \overline{q}_u) \leq 0 \\ \overline{\Phi}_v\,(T, \overline{q}_v) &= |T| - (T_y - \overline{q}_v) \leq 0, \end{aligned} \tag{5.20}$$

where N_y and T_y are the forces at yielding point and $\overline{q}_u$ and $\overline{q}_v$ represent stress-like hardening variables. The use of the second principle of thermodynamics for the elastic case provides the state equations

$$\begin{aligned} N &= EA\left(\varepsilon - \overline{\varepsilon}^p\right) \\ T &= GA(\gamma - \overline{\gamma}^p). \end{aligned} \tag{5.21}$$

and

$$\begin{aligned} \overline{q}_u &= -\overline{K}_u \overline{\xi}_u \\ \overline{q}_v &= -\overline{K}_v \overline{\xi}_v. \end{aligned} \tag{5.22}$$

For the inelastic case, the principle of maximum dissipation is considered, the evolution laws are obtained as

$$\begin{aligned} \dot{\overline{\varepsilon}}^p &= \dot{\overline{\lambda}}_u \frac{\partial \overline{\Phi}_u}{\partial N} = \dot{\overline{\lambda}}_u sign(N);\ \dot{\overline{\xi}}_u = \dot{\overline{\lambda}}_u \frac{\partial \overline{\Phi}_u}{\partial \overline{q}_u} = \dot{\overline{\lambda}}_u \\ \dot{\overline{\gamma}}^p &= \dot{\overline{\lambda}}_v \frac{\partial \overline{\Phi}_v}{\partial T} = \dot{\overline{\lambda}}_v sign(T);\ \dot{\overline{\xi}}_v = \dot{\overline{\lambda}}_v \frac{\partial \overline{\Phi}_v}{\partial \overline{q}_v} = \dot{\overline{\lambda}}_v, \end{aligned} \tag{5.23}$$

where the plastic multiplier parameters $\overline{\lambda}_u$ and $\overline{\lambda}_v$ have been introduced to participate in evolution equations obtained from Kuhn-Tucker optimality conditions [Ibrahimbegovic, 2009]. The constitutive equations for the elastoplastic case are

$$\dot{N} = \begin{cases} EA\dot{\varepsilon};\ \dot{\overline{\lambda}}_u = 0 \\ \frac{EA\overline{K}_u}{EA+\overline{K}_u}\dot{\varepsilon};\ \dot{\overline{\lambda}}_u > 0 \end{cases},\ \dot{T} = \begin{cases} GA\dot{\gamma};\ \dot{\overline{\lambda}}_v = 0 \\ \frac{GA\overline{K}_v}{GA+\overline{K}_v}\dot{\gamma};\ \dot{\overline{\lambda}}_v > 0. \end{cases} \tag{5.24}$$

Accompanying loading/unloading conditions and consistency condition obey $\dot{\lambda}\Phi = 0$, $\dot{\lambda} \geq 0$, $\Phi \leq 0$, $\dot{\lambda}\dot{\Phi} = 0$.

The behaviour at the discontinuity in the cohesive link is written in the framework of plasticity with softening. Once the softening phase is reached, continuum to discontinuous transition is triggered in the sense of localization of the plastic strain. Subsequently, increase in strain will lead to decrease in stress. All further plastic deformation will be accumulated in the section once passed the peak resistance. The corresponding strain fields which contain regular and singular components can be decomposed

$$\begin{aligned} \varepsilon &= \overline{\varepsilon} + \overline{\overline{\varepsilon}} \\ \gamma &= \overline{\gamma} + \overline{\overline{\gamma}}. \end{aligned} \tag{5.25}$$

The following failure functions are introduced to detect the softening behaviour

$$\begin{aligned} \overline{\overline{\Phi}}_u\left(t_u, \overline{\overline{q}}_u\right) &= t_u - \left(N_u - \overline{\overline{q}}_u\right) \leq 0 \\ \overline{\overline{\Phi}}_v\left(t_v, \overline{\overline{q}}_v\right) &= |t_v| - \left(T_u - \overline{\overline{q}}_v\right) \leq 0, \end{aligned} \tag{5.26}$$

where N_u, T_u are the ultimate capacity forces and $\overline{\overline{q}}_u$, $\overline{\overline{q}}_v$ as stress-like softening variables obeying the exponential law

$$\begin{aligned} \overline{\overline{q}}_u &= N_u\left(1 - exp\left(-\overline{\overline{\xi}}_u \frac{N_u}{G_{f,u}}\right)\right) \\ \overline{\overline{q}}_v &= V_u\left(1 - exp\left(-\overline{\overline{\xi}}_v \frac{V_u}{G_{f,v}}\right)\right). \end{aligned} \tag{5.27}$$

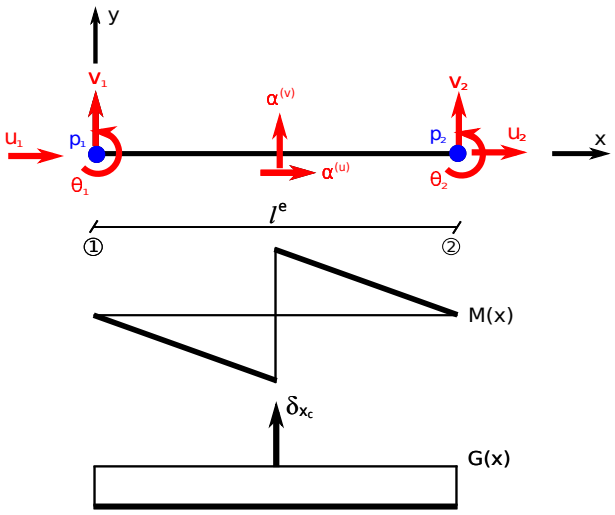

Figure 5.4: The enhanced finite element with it's degrees of freedom and discontinuous shape function $M(x)$ and it's derivative $G(x)$

Variables t_u, t_v are the traction forces at the discontinuity obtained from equilibrium equations. The evolution of internal variables in softening states

$$\begin{aligned} \dot{\alpha}_u &= \dot{\bar{\bar{\lambda}}}_u \frac{\partial \bar{\bar{\Phi}}_u}{\partial N} = \dot{\bar{\bar{\lambda}}}_u sign(N); \;\; \dot{\bar{\bar{\xi}}}_u = \dot{\bar{\bar{\lambda}}}_u \frac{\partial \bar{\bar{\Phi}}_u}{\partial \bar{\bar{q}}_u} = \dot{\bar{\bar{\lambda}}}_u \\ \dot{\alpha}_v &= \dot{\bar{\bar{\lambda}}}_v \frac{\partial \bar{\bar{\Phi}}_v}{\partial T} = \dot{\bar{\bar{\lambda}}}_v sign(T); \;\; \dot{\bar{\bar{\xi}}}_v = \dot{\bar{\bar{\lambda}}}_v \frac{\partial \bar{\bar{\Phi}}_v}{\partial \bar{\bar{q}}_v} = \dot{\bar{\bar{\lambda}}}_v, \end{aligned} \tag{5.28}$$

where $\bar{\bar{\lambda}}$ is the plastic multiplier associated with the softening behaviour and α is an equivalent to the accumulated plastic strain at the discontinuity.

4 The enhanced finite element formulation

4.1 The finite element interpolations

In this section, the enhanced finite element interpolations to solve the presented coupled poroplasticity problem with localized failure is presented. The displacements of the solid skeleton and it's cohesive links **d** are interpolated with the standard linear shape functions $\{N_1^d(x) = 1 - \frac{x}{l_e}, N_2^d(x) = \frac{x}{l_e}\}$, and their derivatives $\{B_1^d(x) = -\frac{1}{l_e}, B_2^d(x) = \frac{1}{l_e}\}$. Note that the superscript d denotes the variables related to displacements of the solid skeleton.

The discontinuous contribution brought by the Heaviside function can be recast in a format which is suitable for embedded discontinuity formulation and local character of discontinuity unknowns as shown in previous chapters. Such perturbation leads to the

additional discontinuity shape function $M(x)$ and its derivative $G(x)$, shown in Figure 5.4

$$\begin{aligned} M(x) &= \begin{cases} -\frac{x}{l^e}; x \in [0, x_c\rangle \\ 1 - \frac{x}{l^e}; x \in \langle x_c, l^e] \end{cases} \\ G(x) &= \overline{G} + \delta_{x_c} = -\frac{1}{l^e} + \delta_{x_c}. \end{aligned} \tag{5.29}$$

Thus the interpolation of the enhanced displacement field from (5.16) leads to

$$\begin{aligned} u(x) &= \textstyle\sum_{a=1}^{2} N_a^d(x) u_a + M(x)\alpha^{(u)} \\ v(x) &= \textstyle\sum_{a=1}^{2} N_a^d(x) v_a + M(x)\alpha^{(v)} \\ \theta(x) &= \textstyle\sum_{a=1}^{2} N_a^d(x)\theta_a. \end{aligned} \tag{5.30}$$

The corresponding enhanced strain field follows from the displacement field

$$\begin{aligned} \varepsilon(x) &= \textstyle\sum_{a=1}^{2} B_a^d(x) u_a + G(x)\alpha^{(u)} \\ \gamma(x) &= \textstyle\sum_{a=1}^{2} \left(B_a^d(x) v_a - N_a^d(x)\theta_a \right) + G(x)\alpha^{(v)} \\ \kappa(x) &= \textstyle\sum_{a=1}^{2} B_a^d(x)\theta_a. \end{aligned} \tag{5.31}$$

The fluid flow on top of lattice domain is governed by the non-steady diffusion equation which results from the fluid continuity equation introducing the Darcy law. Latter is achieved by adding the pressure degree of freedom on top of standard Timoshenko degrees of freedom leading to enhanced element, not only in terms of added pressures, but also in localized discontinuity contributions. The enhanced finite element with all degrees of freedom is shown in Figure 5.4.

The pressure field is interpolated with the linear shape functions that correspond to the ones of solid skeleton $\{N_1^p(x) = 1 - \frac{x}{l_e},\ \ N_2^p(x) = \frac{x}{l_e}\}$. The corresponding derivatives are $\{B_1^p(x) = -\frac{1}{l_e},\ \ B_2^p(x) = \frac{1}{l_e}\}$. However, the pressure interpolation functions are denoted with the superscript p for clearer presentation. Since the fluid flow problem is transient, the time parameter t is introduced and the discretization field for pressure follows

$$p(x,t) = \sum_{a=1}^{2} N_a^p(x) p_a(t). \tag{5.32}$$

The discretization of the pressure gradient is

$$\frac{\partial p}{\partial x}(x,t) = \sum_{a=1}^{2} B_a^p(x) p_a(t), \tag{5.33}$$

while its time derivative

$$\frac{\partial p}{\partial t}(x,t) = \sum_{a=1}^{2} N_a^p(x) \dot{p}_a(t). \tag{5.34}$$

The generalized nodal pressure field can be denoted with $\mathbf{p} = (p_1, p_2)^T$.

4.2 The enhanced weak form

The enhanced strain field from (5.31) can be written in its generalized form

$$\boldsymbol{\varepsilon} = \mathbf{B}^d \mathbf{d} + \mathbf{G}\boldsymbol{\alpha}, \tag{5.35}$$

while the virtual strains obey the same interpolations as the real strains

$$\delta\boldsymbol{\varepsilon} = \mathbf{B}^d \delta\mathbf{d} + \mathbf{G}\delta\boldsymbol{\alpha}. \tag{5.36}$$

The $\delta\mathbf{d}$ and $\delta\boldsymbol{\alpha}$ denote the nodal virtual generalized displacement and virtual displacement jumps. The only difference in real and virtual strain fields concerns the modified enhanced contribution $\tilde{\mathbf{G}}$. Namely, it is necessary to enforce the orthogonality between enhanced strain and constant stress within the element which will fulfil the patch test condition as already shown for the method of incompatible modes [Ibrahimbegovic and Wilson, 1991]

$$\tilde{\mathbf{G}} = \mathbf{G} - \frac{1}{l_e}\int_0^{l_e} \mathbf{G}dx. \tag{5.37}$$

When the interface is positioned in the middle of an element, condition (5.37) is automatically verified and $\tilde{\mathbf{G}}$ remains the same as $\mathbf{G}$. It should be noted that $\mathbf{G}$ contains the enhanced discontinuity function G which can be decomposed into regular part $\overline{G}$ and singular part holding the Dirac delta function δ_{x_c} like shown in (5.29). With such considerations and interpolations the weak form of the internal forces results with

$$G^{int} = \int_{l_e} (\mathbf{B}^d \delta\mathbf{d})^T \boldsymbol{\sigma} dx + \underbrace{\int_{l_e} \delta\boldsymbol{\alpha}^T (\overline{\mathbf{G}} + \delta_{x_c})\boldsymbol{\sigma} dx}_{\text{h(e)=0}}. \tag{5.38}$$

It follows that internal force vector and the finite element residual vector due to discontinuity are

$$\begin{aligned} \mathbf{F}^{int} &= \textstyle\int_0^{l_e} \mathbf{B}^{d,T}\boldsymbol{\sigma} dx \\ \mathbf{h}^{(e)} &= \textstyle\int_0^{l_e} (\overline{\mathbf{G}} + \delta_{x_c})\boldsymbol{\sigma} dx. \end{aligned} \tag{5.39}$$

Reducing the local residual to zero, the vector $\mathbf{t} = \int_0^{l_e} \delta_{x_c}\boldsymbol{\sigma} dx$ of the internal forces at the discontinuity can be obtained through the regular part of the enhanced local function

$$\mathbf{t} = -\int_0^{l_e} \overline{\mathbf{G}}\boldsymbol{\sigma} dx, \;\; \mathbf{t} = (t_u, t_v, 0)^T. \tag{5.40}$$

4.3 The finite element equations of a coupled poroplastic problem

In this section, the final finite element implementation aspects accounting for each single element contribution, further denoted with subscript e, are presented.

The weak form (5.38) leads to the element residual equation

$$\mathbf{r}_d = \mathbf{F}^{ext} - \mathbf{A}_{e=1}^{n_{el}} \int_0^{l_e} \mathbf{B}^{d,T}\boldsymbol{\sigma} dx, \tag{5.41}$$

where the total stress resultants $\boldsymbol{\sigma}$ are obtained in terms of effective stress resultants $\boldsymbol{\sigma}'$ and pore pressures $\mathbf{p}$ in (5.12). The symbol $\mathbf{A}_{e=1}^{n_{el}}$ denotes the finite element assembly operator for all element contributions. The effective stress resultants $\boldsymbol{\sigma}'$ are calculated in terms of regular parts of enhanced strain field (5.35). The enhanced strain parameters $\boldsymbol{\alpha}$, in each element where localization occurs, are obtained by solving the local equilibrium of the effective stresses

$$\mathbf{h}^{(e)} = \int_{l_e} \overline{\mathbf{G}}\boldsymbol{\sigma}' dx + \mathbf{t}', \tag{5.42}$$

where $\mathbf{t}'$ represent the corresponding effective tractions acting at the discontinuity. The local equilibrium equation in (5.42) offers the benefit of local computation of the enhanced parameters. Subsequent static condensation of these parameters allows to keep standard matrix at the global level. The local computation algorithm and numerical procedure are described in the next subsection.

Upon introducing the finite element interpolations, the coupled fluid equation (5.15) results with the finite element residual form

$$\begin{aligned} \mathbf{r}_p = \ \mathbf{Q}^{ext} - \mathbf{A}_{e=1}^{n_{el}} \Bigg[& \int_{l_e} \mathbf{N}^{p,T} M^{-1} \mathbf{N}^p dx \dot{\mathbf{p}}_e - \\ & - \int_{l_e} \mathbf{N}^{p,T} \boldsymbol{\alpha} \mathbf{B}^d dx \dot{\mathbf{d}}_e - \int_{l_e} \mathbf{B}^{p,T} k_f \mathbf{B}^p dx \mathbf{p}_e \Bigg], \end{aligned} \tag{5.43}$$

where $\mathbf{Q}^{ext}$ represent the external applied fluxes and imposed pressures. The consistent linearization of the equations (5.41) and (5.43) leads to a set of linear algebraic equations

$$\mathbf{r}_d^{(i)} - \mathbf{A}_{e=1}^{n_{el}} \Big[\mathbf{K}_e \Delta \mathbf{d}_e - \mathbf{L}_e \Delta \boldsymbol{\alpha}_e - \mathbf{Q}_e \Delta \mathbf{p}_e \Big] = 0 \tag{5.44}$$

and

$$\mathbf{r}_p^{(i)} - \mathbf{A}_{e=1}^{n_{el}} \left[\frac{1}{\Delta t} \mathbf{Q}_e^T \Delta \mathbf{d}_e + \left(\mathbf{H}_e + \frac{1}{\Delta t} \mathbf{S}_e \right) \Delta \mathbf{p}_e \right] = 0 \tag{5.45}$$

in the increments $\Delta t = t_{n+1}^{(i+1)} - t_{n+1}^{(i)}$, where (i) denotes iteration counter within the time interval $[t_n, t_{n+1}]$. The matrices are evaluated in the previous iteration (i) where all values are known. The element stiffness matrix $\mathbf{K}_e$ is defined as

$$\mathbf{K}_e = \int_0^{l_e} \mathbf{B}^{d,T} \mathbf{D}_{sk} \mathbf{B}^d dx \tag{5.46}$$

and the localized contribution matrix

$$\mathbf{L}_e = \int_0^{l_e} \mathbf{B}^{d,T} \mathbf{D}_{sk} \overline{\mathbf{G}} dx. \tag{5.47}$$

The compressibility matrix $\mathbf{S}_e$, the permeability matrix $\mathbf{H}_e$ and the coupling matrix $\mathbf{Q}_e$ are given by

$$\mathbf{S}_e = \int_0^{l_e} \mathbf{N}^{p,T} M^{-1} \mathbf{N}^p dx, \tag{5.48}$$

$$\mathbf{H}_e = \int_0^{l_e} \mathbf{B}^{p,T} k_f \mathbf{B}^p dx, \tag{5.49}$$

$$\mathbf{Q}_e = \int_0^{l_e} \mathbf{B}^{d,T} b \mathbf{N}^p dx. \tag{5.50}$$

The linearization of local equilibrium equation in (5.42) results with

$$\mathbf{h}_e^{(i)} - \mathbf{L}_e^T \Delta \mathbf{d}_e - \mathbf{F}_e \Delta \boldsymbol{\alpha}_e = 0, \tag{5.51}$$

where

$$\mathbf{F}_e = \int_0^{l_e} \overline{\mathbf{G}}^T \mathbf{D}_{sk} \overline{\mathbf{G}} + \mathbf{K}_{dis}. \tag{5.52}$$

Matrix $\mathbf{K}_{dis}$ contains consistent tangent stiffness components for the discontinuity obtained as a derivatives of the exponential softening laws from (5.27) with respect to the corresponding displacement jumps.

The enhanced strain parameters $\Delta\boldsymbol{\alpha}$ can be obtained by the local operator split solution procedure and return mapping algorithm presented in the next section. Finally, the static condensation strategy serves for local elimination of the enhanced strain parameters which leads to the final statically condensed equation

$$\mathbf{r}_d^{(i)} - \mathbf{A}_{e=1}^{n_{el}} \left[\left(\mathbf{K}_e - \mathbf{L}_e^T \mathbf{F}_e^{-1} \mathbf{L}_e \right) \Delta \mathbf{d}_e - \mathbf{Q}_e \Delta \mathbf{p}_e \right] = 0. \tag{5.53}$$

The final coupled problem in its linearized form can be written in the matrix format

$$\mathbf{R}^{(i)} = \mathbf{A}_{e=1}^{n_{el}} \begin{bmatrix} \widehat{\mathbf{K}}_e & \mathbf{Q}_e \\ \frac{1}{\Delta t} \mathbf{Q}_e^T & \mathbf{H}_e + \frac{1}{\Delta t} \mathbf{S}_e \end{bmatrix}_{n+1}^{(i)} \begin{pmatrix} \Delta \mathbf{d}_e \\ \Delta \mathbf{p}_e \end{pmatrix}^{(i+1)} \tag{5.54}$$

with modified stiffness matrix in its statically condensed form

$$\widehat{\mathbf{K}}_e = \mathbf{K}_e - \mathbf{L}_e^T \mathbf{F}_e^{-1} \mathbf{L}_e. \tag{5.55}$$

4.4 The operator split algorithm

The operator split is an element-wise algorithm performed for each directional component with its ultimate goal of computing the internal variables related to discontinuity. After computing the internal variables locally, the global solution procedure with Newton incremental/iterative procedure can be performed.

It is assumed that the best iterative value of displacements $u_{n+1}^{(i)}$ and $v_{n+1}^{(i)}$ for which the trial values of the traction forces are obtained

$$\begin{aligned} t_{u,n+1}^{trial} &= -\int_0^{l_e} \overline{G} \left[EA \left(\textstyle\sum_{a=1}^2 B_a^d u_{a,n+1}^{(i)} + \overline{G} \alpha_{u,n} \right) \right] \\ t_{v,n+1}^{trial} &= -\int_0^{l_e} \overline{G} \left[GA \left(\textstyle\sum_{a=1}^2 B_a^d v_{a,n+1}^{(i)} + \overline{G} \alpha_{v,n} \right) \right], \end{aligned} \tag{5.56}$$

where $\alpha_{u,n}$, $\alpha_{v,n}$ represent the discontinuity parameters at previous time for softening plastic deformation. Later on, the trial value of failure functions ought to be calculated

$$\begin{aligned} \overline{\overline{\Phi}}^{trial}_{u,n+1} &= t^{trial}_{u,n+1} - \left(N_u - \overline{\overline{q}}_{u,n}\right), \\ \overline{\overline{\Phi}}^{trial}_{v,n+1} &= \left|t^{trial}_{v,n+1}\right| - \left(V_u - \overline{\overline{q}}_{v,n}\right) \end{aligned} \tag{5.57}$$

with $\overline{\overline{q}}_{u,n}$ and $\overline{\overline{q}}_{v,n}$ defined in (5.27). If the trial values of the failure functions are negative or zero, the elastic trial step is accepted for final, with no modification of the plastic strain from the previous time step

$$\begin{aligned} \alpha_{u,n+1} &= \alpha_{u,n};\ \overline{\overline{\xi}}_{u,n+1} = \overline{\overline{\xi}}_{u,n}, \\ \alpha_{v,n+1} &= \alpha_{v,n};\ \overline{\overline{\xi}}_{v,n+1} = \overline{\overline{\xi}}_{v,n}. \end{aligned} \tag{5.58}$$

The plastic softening parameter will remain intact, while the traction force will be changed due to displacement increment.

On the other hand, if the trial values of failure functions are positive, the current step is in the softening plasticity and there is a need to modify the elastic strain and internal variables $\alpha_{u,n}$, $\alpha_{v,n}$ in order to re-establish the plastic admissibility at discontinuity. The internal softening plasticity variables ought to be updated by using evolution equations

$$\begin{aligned} \alpha_{u,n+1} &= \alpha_{u,n} + \overline{\overline{\lambda}}_{u,n+1} sign\left(t^{trial}_{u,n+1}\right) \\ \alpha_{v,n+1} &= \alpha_{v,n} + \overline{\overline{\lambda}}_{v,n+1} sign\left(t^{trial}_{v,n+1}\right) \end{aligned} \tag{5.59}$$

and

$$\begin{aligned} \overline{\overline{\xi}}_{u,n+1} &= \overline{\overline{\xi}}_{u,n} + \overline{\overline{\lambda}}_{u,n+1} \\ \overline{\overline{\xi}}_{v,n+1} &= \overline{\overline{\xi}}_{v,n} + \overline{\overline{\lambda}}_{v,n+1}, \end{aligned} \tag{5.60}$$

where $\overline{\overline{\lambda}}_{u,n+1}$, $\overline{\overline{\lambda}}_{v,n+1}$ are softening plastic multipliers. The value of the plastic multiplier is determined from the conditions $\overline{\overline{\Phi}}_{u,n+1} \leq tol$ and $\overline{\overline{\Phi}}_{v,n+1} \leq tol$ and the solutions of a nonlinear equations are obtained iteratively using the Newton-Raphson method

$$\begin{aligned} \overline{\overline{\Phi}}_{u,n+1} &= \overline{\overline{\Phi}}^{trial}_{u,n+1} + \left(\overline{\overline{q}}_{u,n+1} - \overline{\overline{q}}_{u,n}\right) + EA\overline{G}\overline{\overline{\lambda}}_{u,n+1} \leq tol \\ \overline{\overline{\Phi}}_{v,n+1} &= \overline{\overline{\Phi}}^{trial}_{v,n+1} + \left(\overline{\overline{q}}_{v,n+1} - \overline{\overline{q}}_{v,n}\right) + GA\overline{G}\overline{\overline{\lambda}}_{v,n+1} \leq tol. \end{aligned} \tag{5.61}$$

In the plastic softening step, the traction forces are produced by a change of discontinuity parameters α_u and α_v.

5 Numerical simulations

In this section, the results of several representative numerical simulations are presented. The novel model formulations are implemented into the research version of the computer code FEAP, developed by R.L. Taylor [Taylor, 2011]

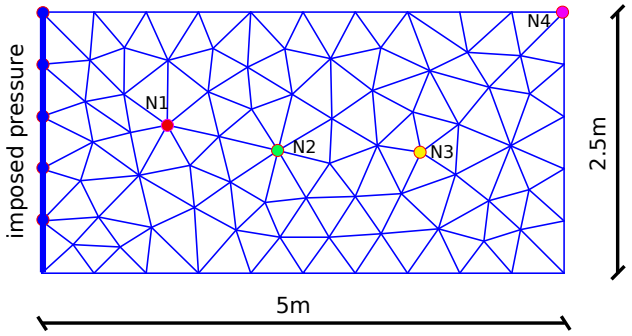

Figure 5.5: Configuration of the sample for the uncoupled fluid flow problem

5.1 Uncoupled fluid flow across the lattice

In this section, the uncoupled fluid flow across the domain represented by lattice network is presented. The geometry of the flow problem, along with its boundary conditions is shown in Figure 5.5. The solution of the problem is found through the solution of the uncoupled (Biot coefficient is set to $b = 0$) fluid flow equation (5.43). The fluid pressure of $1Pa$ is imposed at the left hand side and kept constant during the time of $t = 0.1s$ in which the flow is monitored. The Biot modulus is set to $M = 10Pa$ and permeability $K_f = 10m^2/(Pa \cdot s)$.

The application of the fluid flow through the domain represented by lattice model requires the computation of the lattice permeability parameters, in order to obtain the discrete flow model parameters. The latter ought to be able to compute the nodal pressures and fluid velocities which correspond to nodal values obtained with an underlying continuum flow. Considering in this example the uncoupled fluid flow, the comparison between the fluid flow across the lattice and corresponding continuum formulation is performed.

The connection between the lattice and given permeability may start with the final integrated form of permeability matrix $\mathbf{H}_e$ from (5.49) with

$$\mathbf{H}_e = \frac{k_f A_f}{l_e} \begin{bmatrix} 1 & -1 \\ -1 & 1 \end{bmatrix}, \tag{5.62}$$

where A_f is the cross section area disposable for the fluid flow. In (5.62) above, the permeability coefficient can be denoted with

$$K_f = \frac{k_f A_f}{l_e}. \tag{5.63}$$

Motivated by the Hammer quadrature rule [Zienkiewicz and Taylor, 2000] for numerical integration on a triangle with 3 integration points, which are placed in the center of each side of the triangle, the cross section area disposable for fluid flow is defined as the shortest distance between centroids h_f of the two neighbouring triangles multiplied by the thickness of 1 (see Figure 5.6). Associating K_f with given permeability and k_f with

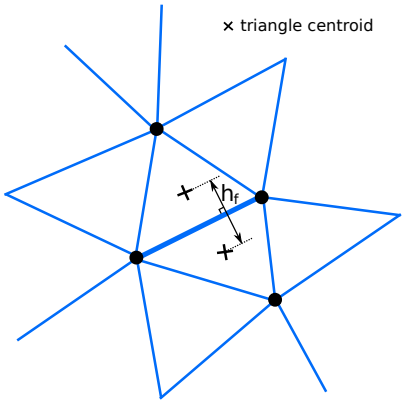

Figure 5.6: The fluid flow disposable cross section area computation

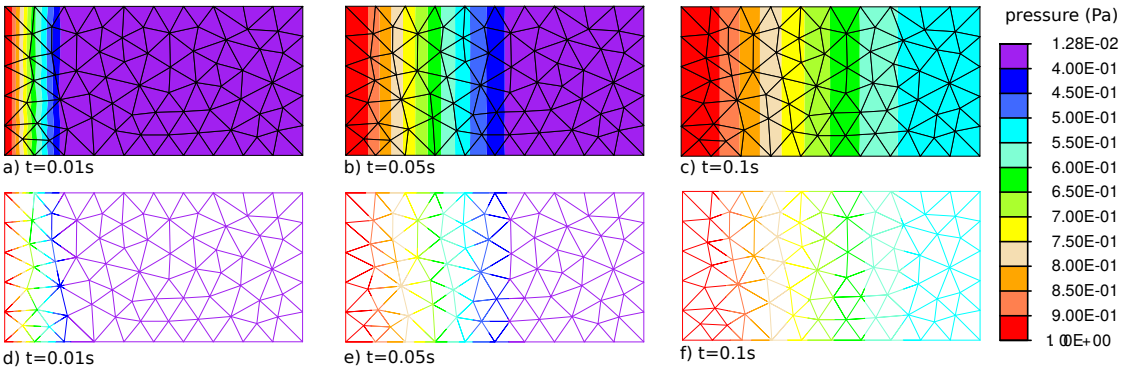

Figure 5.7: The comparison between the discrete lattice fluid flow and continuum fluid flow in terms of pore pressures.

lattice permeability, writing down $h_f = c \cdot l_e$ and $A_f = h_f(\cdot 1)$, the following expression is obtained

$$K_f = k_f \cdot c \quad \mapsto \quad k_f = \frac{K_f}{c}, \tag{5.64}$$

with c being the coefficient of modification of permeability for given lattice. Note that such coefficient differs for every element in the mesh. For the ideal case where two equilateral triangles share the same side, the value of coefficient $c = \sqrt{3}/3 \approx 0.577$.

With newly obtained lattice permeability parameters, the simulation of the fluid flow across the lattice may be conducted and further compared to the fluid flow obtained with an equivalent underlying continuum model. Comparison is done in terms of nodal fluid pressures across the discrete lattice versus continuum model. The results are presented in Figure 5.7 showing the pressure wave advancing in both cases equally, from the left hand side, where the pressure was imposed and kept constant, towards the right hand side.

In addition, the 4 nodes are distinguished from the mesh (Figure 5.5), and the pressure wave evolution in time is plotted in Figure 5.8, resulting with very close curves in both cases, continuum and discrete.

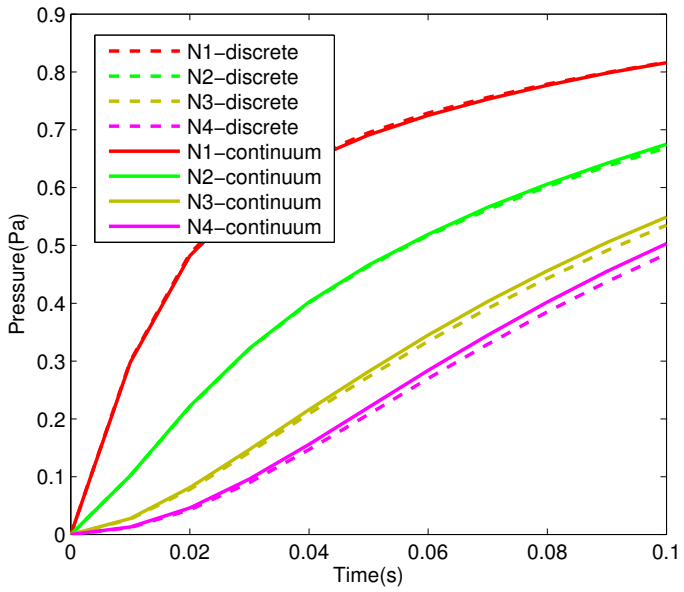

Figure 5.8: Pressure time evolution at 4 different nodes

This result allows us to adopt the presented discrete model approach for fluid flow and apply the same procedure for computing the lattice permeability parameters in the following examples, dealing with coupled case.

5.2 Uniaxial coupled poroelastic problem

The coupled problem given in this section can be considered as a poroelastic benchmark, which is proposed by [Zheng et al., 2003]. The uniform load of $4MPa$ is applied to the top of the oil-saturated porous sample as shown in Figure 5.9. The horizontal motions of its side boundaries are restricted, as well as the vertical displacement of the bottom boundary, all constrained to zero. The fluid is allowed to flow through the upper boundary, while the bottom and side boundaries remain impermeable. The material parameters of this sample are listed in Table 5.1.

The goal here is to compare the discrete model results against the result from literature [Zheng et al., 2003], obtained with the continuum poroelastic model. The proposed discrete model is employed here, in order to verify its reliability to simulate coupled poro-elastic problems. In this example the intrinsic permeability is given as a property of porous media only, not the fluid which flows through it. Thus, the intrinsic permeability needs to be divided by the dynamic viscosity μ of the fluid to get K_f/μ, where $\mu = \rho \cdot \nu$ with ν as the kinematic viscosity. The same procedure of computing the lattice permeability parameters with respect to given permeability from the numerical example in previous section is repeated. In the computations, the *GPa* are used for pressures and elasticity constants, and 10^9 kilogram for mass to avoid the ill-conditioning of the global matrix

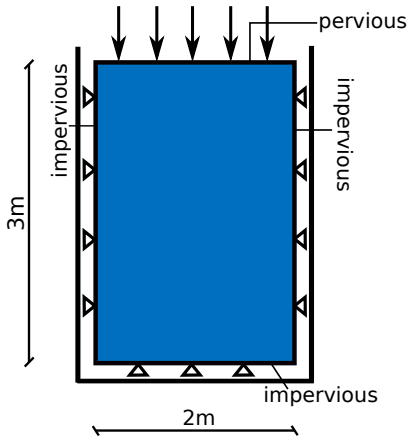

Figure 5.9: Configuration of the poro-elastic sample and it's boundary conditions

Table 5.1: Material parameters considered in the numerical simulations of poro-elastic sample

Drained Young modulus	$E_{sk} = 1.44 \cdot 10^4 \ MPa$
Drained Poisson ratio	$\nu_{sk} = 0.2$
Biot coefficient	$b = 0.79$
Biot modulus	$M = 1.23 \cdot 10^4 \ MPa$
Oil density	$\rho = 940 \ kg/m^3$
Porosity	$n_f = 0.2$
Intrinsic permeability	$K_f = 2 \cdot 10^{-13} \ m^2$
Kinematic viscosity	$\nu = 1.3 \cdot 10^{-4} \ m^2/s$

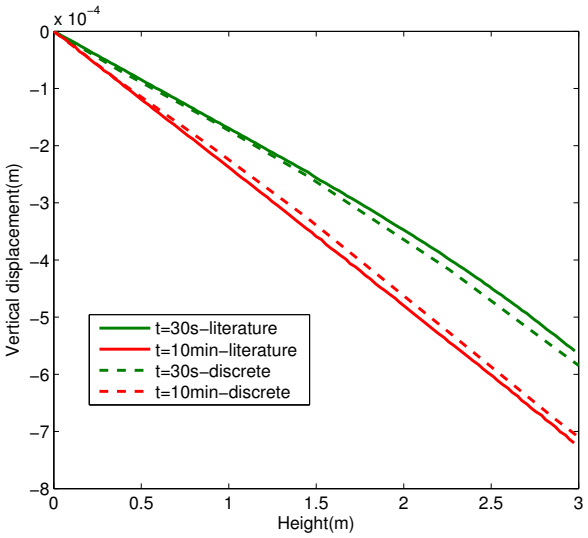

Figure 5.10: Vertical displacements of the sample after 30 seconds and 10 minutes; the sample is converging to the totally drained state.

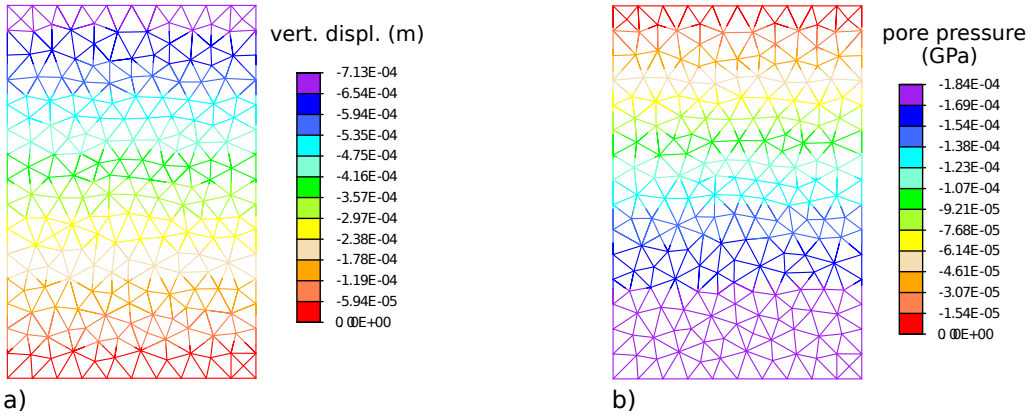

Figure 5.11: The 'drained' state of the specimen after 10 minutes: a) vertical displacements, b) pore pressures

that occurs if ISO units are used.

Keeping the external load constant at $4MPa$, the state of the sample through the time is monitored. In Figure 5.10., the vertical displacements of the sample are plotted after 30 seconds and 10 minutes, and compared against the literature results. A fairly matching is observed.

As time goes to infinity, the vertical displacements increase and the state of the porous sample settles down at the totally drained condition, with the pore pressure reduced to zero.

The state of the sample after 10 minutes is shown in Figure 5.11. The vertical displacement of the solid shows a linear variation along the height of the sample. The pore pressures are zero at the upper fully-drained boundary, while the rest of the sample shows the values of pressure at almost totally drained state.

5.3 Drained compression test of the poro-plastic sample with the localized failure

The fluid saturated rock sample under the compression test is considered in this section. The geometry of the sample and boundary conditions imposed on the displacement and pore pressure fields are shown in Figure 5.12. The external load is applied via constant velocity $v_0 = 5 \cdot 10^{-4} m/s$ imposed on the top base. With the aim of observing the coupling effects as well, the tests are then repeated with the imposed constant velocity $v_0 = 1.5 \cdot 10^{-3} m/s$. The chosen material parameters listed in Table 5.2 correspond to the limestone fully saturated with the water. The value of hydraulic permeability of the sample obtained from the parameters in the Table 5.2 is equal to $K_h = \rho_w g K_f = 1 \cdot 10^{-8}\ m/s$, where the procedure of computing lattice permeabilities is used again.

The ultimate shear strength of geomaterials is defined by the Mohr-Coulomb failure criterion which states

$$\tau_f = \tau_u + \sigma_c \cdot tan(\phi), \tag{5.65}$$

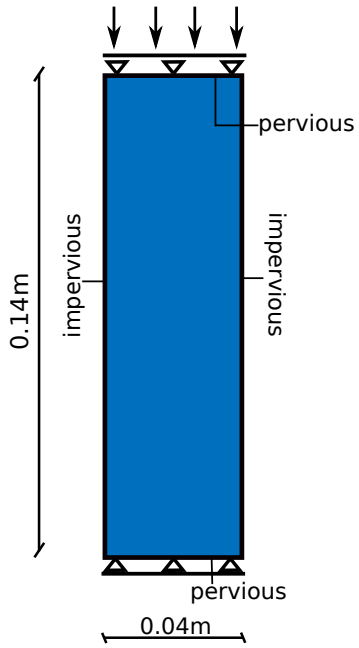

Figure 5.12: Geometry of the poroplastic sample and imposed boundary conditions

where τ_u represents cohesion-like value of ultimate shear force when compression force is equal to zero, σ_c represents the compression force and ϕ is internal angle of friction.

The final goal is to investigate the influence of heterogeneity upon the localized failure of the proposed sample. The presented discrete model formulation is capable of considering the influence of heterogeneity. It has already been shown that the localized failure with displacement discontinuities can be strongly influenced by the heterogeneity and initial defects. The latter might be included through the Gauss distribution of the material parameters as shown in Chapter 1, or through two or multi-phase representation of the material with different properties as shown in Chapter 2. Here, the two-phase representation is adopted, where the second phase takes the slightly weaker properties in terms of material strengths ($\sigma_{u,t} = 12\ \ MPa$; $\tau_u = 24\ \ MPa$). The two-phases are distributed randomly throughout the sample and each phase participates with equal number of elements. The differences in two samples are brought by the different distributions of the phases when the random sampling is performed two times in a row. Figures 5.13 and 5.14 show the displacements and pore pressures of the heterogeneous samples 1 and 2 plotted in the deformed mesh at the final time step of the simulation. These results are obtained with the imposed constant velocity of $v_0 = 5 \cdot 10^{-4} m/s$. It can be observed from the deformed meshes of both samples that the localized macro cracks propagate differently in two cases only because of the slight difference in initial heterogeneity distributions. Macro-cracks also formed the irregular geometries that propagated through the weaker parts of the material. The main strength of the presented discrete model is in simulating the heterogeneous materials where macro-cracks propagate through the material's weaker phases, avoid the stiffer ones and exhibit the irregular geometries. When it comes to the

Table 5.2: Material parameters considered in the numerical simulations of poro-plastic sample

Drained Young modulus	$E_{sk} = 50\ GPa$
Drained Poisson ratio	$\nu_{sk} = 0.25$
Tensile yield stress	$\sigma_{y,t} = 12\ MPa$
Shear yield stress	$\tau_y = 23\ MPa$
Hardening modulus	$\overline{K} = 5\ GPa$
Tensile strength	$\sigma_{u,t} = 13\ MPa$
Shear strength	$\tau_u = 25\ MPa$
Angle of friction	$\phi = 35^\circ$
Fracture energies	$G_{f,u} = 300N/m$; $G_{f,v} = 600N/m$
Biot coefficient	$b = 0.8$
Biot modulus	$M = 16.9\ GPa$
Porosity	$n_f = 0.1$
Permeability	$K_f = 1 \cdot 10^{-9}\ m^2/(kPa/s)$
Fluid density	$\rho_w = 1000\ kg/m^3$

pore pressures, they remain zero at the pervious sides and reach their highest values near the localized zone.

To investigate the coupling effects, the two heterogeneous samples are put under compression test with a different rate of imposed vertical displacement on the top base $v_0 = 1.5 \cdot 10^{-3} m/s$. The macroscopic curves including the cumulative vertical reaction and pore pressure in the centre of the sample in the close neighboured of the localized zone are presented in Figure 5.15, for two heterogeneous samples and different imposed velocities obtained within the compression tests.

The macroscopic vertical reactions indicate that higher rates of imposed displacement cause the samples to be more resistant (larger ultimate stress) and more ductile (larger displacement is needed to drive the samples to the failure). This is due to an increase of pore pressure which is brought by shorter time left for drainage at the sample centre (Figure 5.15.b).

The pronounced coupling effects are more obvious when it comes to the non-linear behaviour and formation of localization zone. In the beginning of the test, the vertical reaction is less influenced by higher pore pressure.

No coupling effect is observed in the geometry of the macro-crack for each sample when it comes to the localized zone formation. More precisely, the discontinuity still propagated through the same elements for different imposed velocities.

The differences with respect to heterogeneities seem to increase in the nonlinear zone with the higher imposed velocity. Namely, the increase of flow through cracks in localization zone, together with the 'faster' loading, induces the higher rates of pore pressures making the heterogeneities' influence even more profound.

As can be seen from Figure 5.16.a, where time history of the crack length is presented,

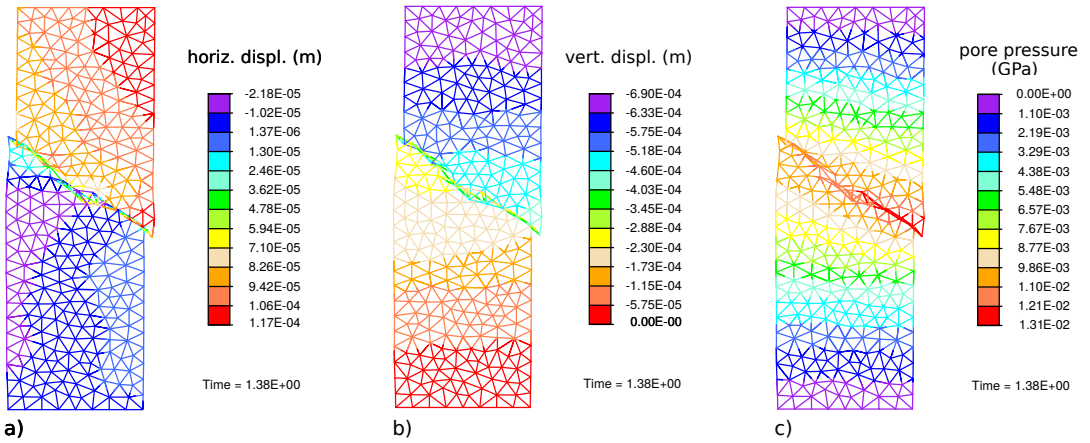

Figure 5.13: The state of the 1st heterogeneous sample after the compression test (imposed velocity $v_0 = 5 \cdot 10^{-4} m/s$): a) horizontal displacement b) vertical displacement c) pore pressure

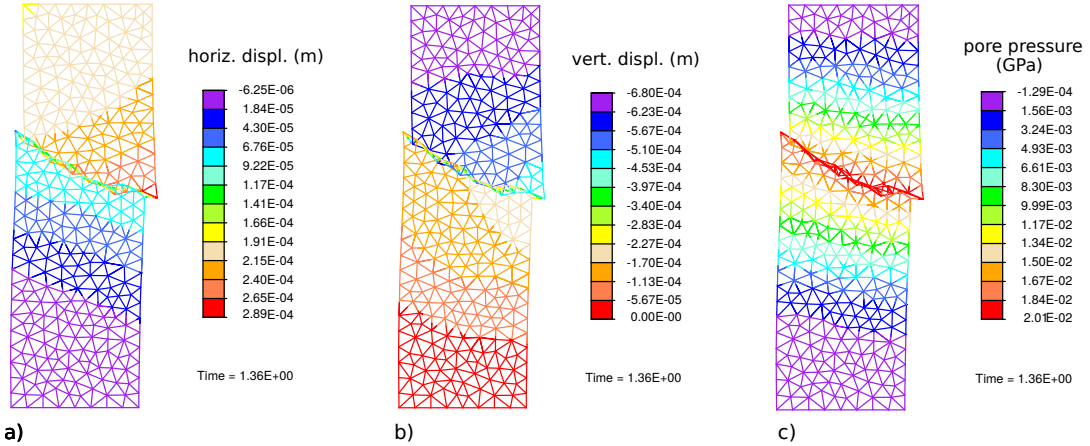

Figure 5.14: The state of the 2nd heterogeneous sample after the compression test (imposed velocity $v_0 = 5 \cdot 10^{-4} m/s$): a) horizontal displacement b) vertical displacement c) pore pressure

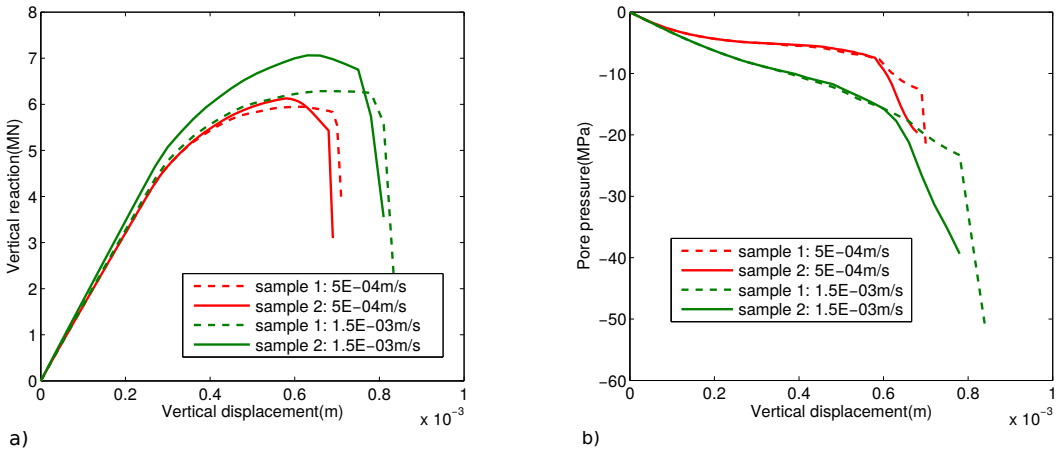

Figure 5.15: Macroscopic curves of the poro-plastic sample obtained within the compression test a) cumulative vertical reaction vs impose displacement b) pore pressure at the sample centre vs imposed displacement

cracks start to propagate at some point in time when the external load produces significant stress triggering the crack. The cracks then propagate quickly through the samples. The plots for samples with applied faster external load ($v_0 = 1.5 \cdot 10^{-3} m/s$) show, that in these cases, cracks propagate more quickly and the tests are completed in less time. Figure 5.16.b presents the time evolution of pore pressure in the centre of the sample and in the close neighboured of the crack, showing the shorter time needed for completion of test and faster rate of the pore pressure increase.

6 Final comments on the presented failure model of fluid-saturated rock medium

In this chapter the discrete element model suitable for describing the fracture process with localized failure zones in heterogeneous fluid-saturated poro-plastic medium is presented, where coupling between the fluid and solid obey the Biot theory of poroplasticity. The localized failure mechanisms are incorporated through the enhanced kinematics of Timoshenko beams that act as cohesive links between the grains of heterogeneous rock material. The embedded discontinuities can represent the failure modes I and II, as well as their combination. The fluid flow is governed by the Darcy law with assumed continuous pore pressure field.

The model ingredients are incorporated into the framework of embedded discontinuity finite element method, where the computation of the enhanced discontinuity parameters requires only local element equilibrium. Further use of the static condensation of the enhanced parameters at the element level, leads to the computationally very efficient approach and numerical implementation that fits within the standard finite element code

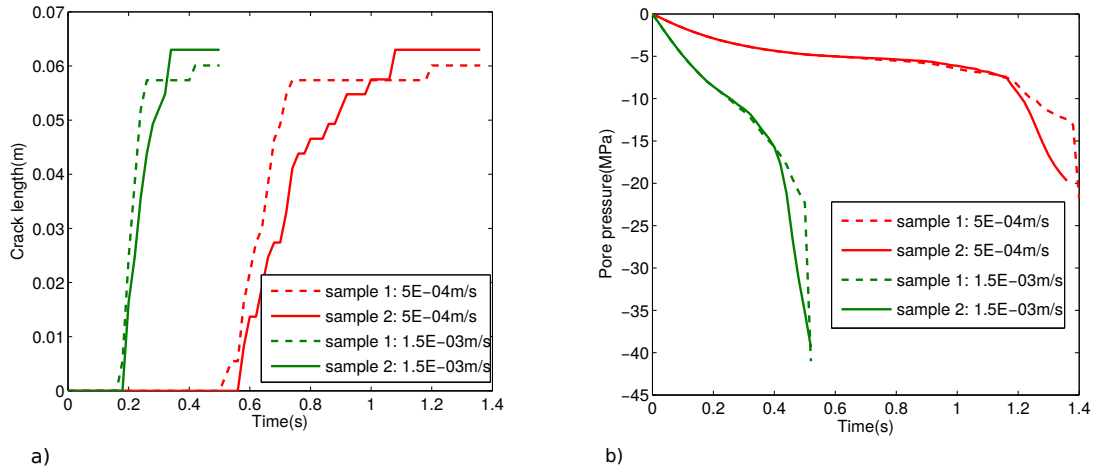

Figure 5.16: a) Crack length vs time b) pore pressure at the sample centre vs time

architecture.

The main strength of the proposed discrete model lies in its ability to account for material heterogeneities with localized macro-cracks propagating throughout the weaker parts of the material and forming the irregular geometries. Such a phenomenon is presented by the numerical simulations of two samples with equal geometries and material properties, but slightly different distribution of material heterogeneities throughout samples, which present different behaviour in terms of localized macro-crack propagation. The solid-fluid coupling plays important role here as well, bringing the variations in macroscopic responses and compliance of the samples. It is important to emphasise that heterogeneous effects become more pronounced with the coupling effects and higher rates of the imposed velocities.

Chapter 6

Conclusions and future perspectives

1 Conclusions

In this thesis three novel numerical models for localized failure of rocks were presented. Rock mechanics model for failure of 2D plain strain specimens was presented firstly. This model was expanded further into 3D space resulting with possibility of simulating full set of 3D failure mechanisms. Finally, the 2D model for failure of rocks was coupled with a fluid-flow for analysing the fracture process under the influence of internal flow through the porous medium.

All three models are constructed within the framework of discrete beam lattice models, where rock material is presented as assembly of material grains given as Voronoi cells, held together by Timoshenko beams as cohesive links. This represent the convenient way for constructing the discrete model since the Voronoi cells are dual to Delaunay triangulation. Localized failure in terms of tensile macro-cracks and shear sliding is allowed to propagate between the rock grains, cutting the cohesive links by half. The enhanced kinematics was added for this purpose within the cohesive links, i.e. Timoshenko beams resulting in embedded discontinuities. Due to this enhancement, re-meshing process is not needed for proper propagation of discontinuities.

Embedded discontinuities within the cohesive links provide the possibility to simulate failure in modes I and II for 2D case, and in modes I, II and III for 3D case. Thus, the full set of failure modes is implemented into these models. The special algorithms are developed for dealing with compression case with built in Mohr-Coulomb law and tension case with simultaneous softening in all failure modes.

Heterogeneous rock samples are considered in terms of two-phase composite in 2D case. Namely, phase I is assumed to be the strong phase, while phase II stands for weaker phase and representation of pre-existing defects. Gaussian statistical variation is used for distribution of material heterogeneities in presented 3D model, with mean value and standard deviation of material parameters which are obtained experimentally. The influence of pre-existing defects was also investigated appearing to be highly influential for localized failure mechanisms.

Numerical results obtained with a 2D model were further confirmed by a 3D model,

where comparison between the numerical and experimental results reveals very good matching. Moreover, the 3D model was also used in a new research study of influence of intact specimen shape deviations on unconfined compressive strength. Penalty contact elements were added to the presented model in order to capture the effects of geometrical micro deviations. It was shown that the model provides a reliable results, which was confirmed by comparing the numerical results with the experimental ones obtained on 90 rock specimens.

The presented 2D model was finally developed towards the coupling with fluids. Biot's theory of poroplasticity was used to handle the coupling conditions resulting with novel discrete lattice approach for simulating the failure under the influence of internal fluid flow. It was shown that the presented model can be used in both, poroelasticity applications, as well as poroplasticity with localized failure.

The main strength of the proposed models is in representing the heterogeneous material properties which directly influence the response of the material through the formation of localized macro-cracks making them geometrically irregular. This is achieved through the discrete lattice approach and embedded discontinuities within the cohesive links in presence of all failure modes, including tensile opening and shear sliding.

All presented models posses a precisely developed algorithms explained in detail, which achieve a desirable convergence for large simulations where a lot of different phenomena happens at the same time.

2 Future perspectives

The presented research and the novel numerical models have a great potential for probability studies of rock mechanics localized failure phenomena where the probability distribution of the heterogeneities and its direct influence on the resulting ultimate limit load computation can be quantified. The great potential also lies in the application of novel models in the large scale simulations of massive structures, especially for ones interacting with the fluid, like embankment dams and in hydraulic fracturing. Such a complex simulations require additional improvements to the existing models. The enhancements of the proposed models could be realized through the couple of stages:

- Development of the 3D model for the analysis of fully fluid-saturated fracture poroplastic medium.

- Implementation of the formulations for the partially saturated poroplastic medium into the existing models. The mechanical behaviour of partially saturated soils can be very different to that of fully saturated soils, and additionally, the effective stress principle is no longer applicable.

- Introducing the probability aspects to the models, considering the heterogeneities, defects and weak zones of the large scale structures, which could be crucial for failure of such a large and complex structures.

Bibliography

[Argyris, 1960] Argyris, J. H. (1960). *Energy Theorems and Structural Analysis*. Butterworths.

[Barber et al., 1996] Barber, C. B., Dobkin, D. P., and Huhdanpaa, H. (1996). The quickhull algorithm for convex hulls. *ACM Trans. Math. Softw.*, 22(4):469–483.

[Bathe, 2006] Bathe, K. (2006). *Finite Element Procedures*. Prentice Hall, New Jersey.

[Belytschko et al., 1996] Belytschko, T., Krongauz, Y., Organ, D., Fleming, M., and Krysl, P. (1996). Meshless methods: An overview and recent developments. *Computer Methods in Applied Mechanics and Engineering*, 139(1-4):3 – 47.

[Benito et al., 2001] Benito, J., Urena, F., and Gavete, L. (2001). Influence of several factors in the generalized finite difference method. *Applied Mathematical Modelling*, 25(12):1039 – 1053.

[Benkemoun et al., 2015] Benkemoun, N., Gelet, R., Roubin, E., and Colliat, J.-B. (2015). Poroelastic two-phase material modeling: theoretical formulation and embedded finite element method implementation. *International Journal for Numerical and Analytical Methods in Geomechanics*, 39:1255–1275.

[Benkemoun et al., 2010] Benkemoun, N., Hautefeuille, M., Colliat, J.-B., and Ibrahimbegovic, A. (2010). Failure of heterogeneous materials: 3d meso-scale fe models with embedded discontinuities. *International Journal for Numerical Methods in Engineering*, 82(13):1671–1688.

[Benkemoun et al., 2012] Benkemoun, N., Ibrahimbegovic, A., and Colliat, J.-B. (2012). Anisotropic constitutive model of plasticity capable of accounting for details of meso-structure of two-phase composite material. *Computers & Structures*, 90-91:153 – 162.

[Berton and Bolander, 2006] Berton, S. and Bolander, J. E. (2006). Crack band model of fracture in irregular lattices. *Computer Methods in Applied Mechanics and Engineering*, 195(52):7172 – 7181.

[Bieniawski, 1967] Bieniawski, Z. (1967). Mechanism of brittle fracture of rock: Part i - theory of the fracture process. *International Journal of Rock Mechanics and Mining Sciences & Geomechanics Abstracts*, 4(4):395 – 406.

[Biot, 1965] Biot, M. A. (1965). *Mechanics of incremental deformations*. John Wiley & Sons.

[Blandford et al., 1981] Blandford, G. E., Ingraffea, A. R., and Liggett, J. A. (1981). Two-dimensional stress intensity factor computations using the boundary element method. *International Journal for Numerical Methods in Engineering*, 17(3):387–404.

[Bonnet et al., 1998] Bonnet, M., Maier, G., and Polizzotto, C. (1998). Symmetric galerkin boundary element methods. *Applied Mechanics Reviews*, 51:669–704.

[Brancherie and Ibrahimbegovic, 2009] Brancherie, D. and Ibrahimbegovic, A. (2009). Novel anisotropic continuum-discrete damage model capable of representing localized failure of massive structures - part i. *Engineering Computations*, 26(1/2):100–127.

[Brighi et al., 1998] Brighi, B., Chipot, M., and Gut, E. (1998). Finite differences on triangular grids. *Numerical Methods for Partial Differential Equations*, 14(5):567–579.

[Bui et al., 2014] Bui, N., Ngo, M., Nikolic, M., Brancherie, D., and Ibrahimbegovic, A. (2014). Enriched timoshenko beam finite element for modeling bending and shear failure of reinforced concrete frames. *Computers & Structures*, 143(0):9 – 18.

[Cacas et al., 1990] Cacas, M. C., Ledoux, E., de Marsily, G., Tillie, B., Barbreau, A., Durand, E., Feuga, B., and Peaudecerf, P. (1990). Modeling fracture flow with a stochastic discrete fracture network: calibration and validation: 1. the flow model. *Water Resources Research*, 26(3):479–489.

[Callari and Armero, 2002] Callari, C. and Armero, F. (2002). Finite element methods for the analysis of strong discontinuities in coupled poro-plastic media. *Computer Methods in Applied Mechanics and Engineering*, 191(39-40):4371 – 4400.

[Callari et al., 2010] Callari, C., Armero, F., and Abati, A. (2010). Strong discontinuities in partially saturated poroplastic solids. *Computer Methods in Applied Mechanics and Engineering*, 199(23-24):1513 – 1535.

[Chang et al., 2002] Chang, C., Wang, T., Sluys, L., and van Mier, J. (2002). Fracture modeling using a micro-structural mechanics approach - i. theory and formulation. *Engineering Fracture Mechanics*, 69(17):1941 – 1958.

[Clough, 1960] Clough, R. W. (1960). *The Finite Element Method in Plane Stress Analysis*. American Society of Civil Engineers.

[Crouch and Starfield, 1983] Crouch, S. and Starfield, A. M. (1983). *Boundary Element Methods in Solid Mechanics: With Applications in Rock Mechanics and Geological Engineering*. George Allen & Unwin.

[Cundall, 1971] Cundall, P. (1971). A computer model for simulating progressive, large-scale movements in blocky rock systems. In *Proceedings of the International symposium Rock Fracture, Nancy, France*.

[Cundall, 1988] Cundall, P. (1988). Formulation of a three-dimensional distinct element model-part i. a scheme to detect and represent contacts in a system composed of many polyhedral blocks. *International Journal of Rock Mechanics and Mining Sciences & Geomechanics Abstracts*, 25(3):107 – 116.

[Cusatis et al., 2006] Cusatis, G., Bazant, Z., and Cedolin, L. (2006). Confinement-shear lattice csl model for fracture propagation in concrete. *Computer Methods in Applied Mechanics and Engineering*, 195:7154–7171.

[da Costa et al., 2009] da Costa, D. D., Alfaiate, J., Sluys, L., and Julio, E. (2009). Towards a generalization of a discrete strong discontinuity approach. *Computer Methods in Applied Mechanics and Engineering*, 198(47-48):3670 – 3681.

[de Borst et al., 2006] de Borst, R., Rethore, J., and Abellan, M.-A. (2006). A numerical approach for arbitrary cracks in a fluid-saturated medium. *Archive of Applied Mechanics*, 75(10-12):595–606.

[Fallah et al., 2000] Fallah, N., Bailey, C., Cross, M., and Taylor, G. (2000). Comparison of finite element and finite volume methods application in geometrically nonlinear stress analysis. *Applied Mathematical Modelling*, 24(7):439 – 455.

[Feng et al., 2014] Feng, J., Li, C., Cen, S., and Owen, D. (2014). Statistical reconstruction of two-phase random media. *Computers & Structures*, 137(0):78 – 92.

[Fries and Belytschko, 2006] Fries, T.-P. and Belytschko, T. (2006). The intrinsic xfem: a method for arbitrary discontinuities without additional unknowns. *International Journal for Numerical Methods in Engineering*, 68(13):1358–1385.

[Fries and Belytschko, 2010] Fries, T.-P. and Belytschko, T. (2010). The extended/generalized finite element method: An overview of the method and its applications. *International Journal for Numerical Methods in Engineering*, 84(3):253–304.

[Geuzaine and Remacle, 2009] Geuzaine, C. and Remacle, J.-F. (2009). Gmsh: A 3-d finite element mesh generator with built-in pre- and post-processing facilities. *International Journal for Numerical Methods in Engineering*, 79(11):1309–1331.

[Ghaboussi, 1988] Ghaboussi, J. (1988). Fully deformable discrete element analysis using a finite element approach. *Computers and Geotechnics*, 5(3):175 – 195.

[Goodman et al., 1968] Goodman, R. E., Taylor, R. L., and Brekke, T. L. (1968). A model for the mechanics of jointed rock. *Journal of the Soil Mechanics and Foundations Division*, 94(3):637–660.

[Govindjee et al., 1995] Govindjee, S., Kay, G. J., and Simo, J. C. (1995). Anisotropic modelling and numerical simulation of brittle damage in concrete. *International Journal for Numerical Methods in Engineering*, 38(21):3611–3633.

[Hautefeuille et al., 2009] Hautefeuille, M., Melnyk, S., Colliat, J., and Ibrahimbegovic, A. (2009). Failure model for heterogeneous structures using structured meshes and accounting for probability aspects. *Engineering Computations*, 26(1/2):166–184.

[Ibrahimbegovic, 2009] Ibrahimbegovic, A. (2009). *Nonlinear Solid Mechanics: Theoretical Formulations and Finite Element Solution Methods*. Springer.

[Ibrahimbegovic and Delaplace, 2003] Ibrahimbegovic, A. and Delaplace, A. (2003). Microscale and mesoscale discrete models for dynamic fracture of structures built of brittle material. *Computers & Structures*, 81(12):1255 – 1265.

[Ibrahimbegovic and Markovic, 2003] Ibrahimbegovic, A. and Markovic, D. (2003). Strong coupling methods in multi-phase and multi-scale modeling of inelastic behavior of heterogeneous structures. *Computer Methods in Applied Mechanics and Engineering*, 192(28-30):3089 – 3107.

[Ibrahimbegovic and Matthies, 2012] Ibrahimbegovic, A. and Matthies, H. G. (2012). Probabilistic multiscale analysis of inelastic localized failure in solid mechanics. *Computer Assisted Methods in Engineering and Science*, Vol. 19, no. 3:277–304.

[Ibrahimbegovic and Melnyk, 2007] Ibrahimbegovic, A. and Melnyk, S. (2007). Embedded discontinuity finite element method for modeling of localized failure in heterogeneous materials with structured mesh: an alternative to extended finite element method. *Computational Mechanics*, 40(1):149–155.

[Ibrahimbegovic and Wilson, 1991] Ibrahimbegovic, A. and Wilson, E. L. (1991). A modified method of incompatible modes. *Communications in Applied Numerical Methods*, 7(3):187–194.

[Jasak and Weller, 2000] Jasak, H. and Weller, H. G. (2000). Application of the finite volume method and unstructured meshes to linear elasticity. *International Journal for Numerical Methods in Engineering*, 48(2):267–287.

[Jukic et al., 2013] Jukic, M., Brank, B., and Ibrahimbegovic, A. (2013). Embedded discontinuity finite element formulation for failure analysis of planar reinforced concrete beams and frames. *Engineering Structures*, 50(0):115 – 125.

[Karihaloo et al., 2003] Karihaloo, B., Shao, P., and Xiao, Q. (2003). Lattice modelling of the failure of particle composites. *Engineering Fracture Mechanics*, 70(17):2385 – 2406.

[Kontoni, 1992] Kontoni, D. (1992). The dual reciprocity boundary element method for the transient dynamic analysis of elastoplastic problems. In Brebbia, C. and Ingber, M., editors, *Boundary Element Technology VII*, pages 653–669. Springer Netherlands.

[Kucerova et al., 2009] Kucerova, A., Brancherie, D., Ibrahimbegovic, A., Zeman, J., and Bittnar, Z. (2009). Novel anisotropic continuum-discrete damage model capable of representing localized failure of massive structures, part ii. *Engineering Computations*, 26(1/2):128–144.

[Lahrmann, 1992] Lahrmann, A. (1992). An element formulation for the classical finite difference and finite volume method applied to arbitrarily shaped domains. *International Journal for Numerical Methods in Engineering*, 35(4):893–913.

[Lajtai and Lajtai, 1974] Lajtai, E. Z. and Lajtai, V. N. (1974). The evolution of brittle fracture in rocks. *Journal of the Geological Society*, 130:1–18.

[Lemaitre and Chaboche, 1994] Lemaitre, J. and Chaboche, J.-L. (1994). *Mechanics of Solid Materials*. Universite de Paris VI (Pierre et Marie Curie).

[Lewis and Schrefler, 1998] Lewis, R. W. and Schrefler, B. A. (1998). *The Finite Element Method in the Static and Dynamic Deformation and Consolidation of Porous Media*. Wiley, Chichester, 2nd edition edition.

[Lilliu and van Mier, 2003] Lilliu, G. and van Mier, J. (2003). 3d lattice type fracture model for concrete. *Engineering Fracture Mechanics*, 70(7-8):927 – 941.

[Liu et al., 2009] Liu, J., Zhao, Z., Deng, S., and Liang, N. (2009). Numerical investigation of crack growth in concrete subjected to compression by the generalized beam lattice model. *Computational Mechanics*, 43(2):277–295.

[Luo, 2008] Luo, Y. (2008). An efficient 3d timoshenko beam element with consistent shape functions. *Adv. Theor. Appl. Mech.*, 1:95 – 106.

[Mahabadi et al., 2012] Mahabadi, O., Lisjak, A., Munjiza, A., and Grasselli, G. (2012). Y-geo: New combined finite-discrete element numerical code for geomechanical applications. *International Journal of Geomechanics*, 12(6):676–688.

[Martin and Chandler, 1994] Martin, C. and Chandler, N. (1994). The progressive fracture of lac du bonnet granite. *International Journal of Rock Mechanics and Mining Sciences & Geomechanics Abstracts*, 31(6):643 – 659.

[Mi and Aliabadi, 1992] Mi, Y. and Aliabadi, M. (1992). Dual boundary element method for three-dimensional fracture mechanics analysis. *Engineering Analysis with Boundary Elements*, 10(2):161 – 171.

[Moes et al., 1999] Moes, N., Dolbow, J., and Belytschko, T. (1999). A finite element method for crack growth without remeshing. *International Journal for Numerical Methods in Engineering*, 46(1):131–150.

[Munjiza et al., 1995] Munjiza, A., Owen, D., and Bicanic, N. (1995). A combined finite-discrete element method in transient dynamics of fracturing solids. *Engineering Computations*, 12(2):145–174.

[Naylor et al., 1981] Naylor, D. J., Pande, G. N., Simpson, B., and Tabb, R. (1981). *Finite elements in geotechnical engineering*. Pineridge Press.

[Nguyen et al., 2008] Nguyen, V. P., Rabczuk, T., Bordas, S., and Duflot, M. (2008). Meshless methods: A review and computer implementation aspects. *Mathematics and Computers in Simulation*, 79(3):763 – 813.

[Nikolic and Ibrahimbegovic, 2015] Nikolic, M. and Ibrahimbegovic, A. (2015). Rock mechanics model capable of representing initial heterogeneities and full set of 3d failure mechanisms. *Computer Methods in Applied Mechanics and Engineering*, 290:209 – 227.

[Nikolic et al., 2015a] Nikolic, M., Ibrahimbegovic, A., and Miscevic, P. (2015a). Brittle and ductile failure of rocks: Embedded discontinuity approach for representing mode i and mode ii failure mechanisms. *International Journal for Numerical Methods in Engineering*, 102(8):1507–1526.

[Nikolic et al., 2015b] Nikolic, M., Ibrahimbegovic, A., and Miscevic, P. (2015b). Discrete element model for the analysis of fluid-saturated fractured poro-plastic medium based on sharp crack representation with embedded strong discontinuities. *Computer Methods in Applied Mechanics and Engineering*. in press.

[Onate et al., 1994] Onate, E., Cervera, M., and Zienkiewicz, O. C. (1994). A finite volume format for structural mechanics. *International Journal for Numerical Methods in Engineering*, 37(2):181–201.

[Ortiz et al., 1987] Ortiz, M., Leroy, Y., and Needleman, A. (1987). A finite element method for localized failure analysis. *Computer Methods in Applied Mechanics and Engineering*, 61(2):189 – 214.

[Ostoja-Starzewski, 2002] Ostoja-Starzewski, M. (2002). Lattice models in micromechanics. *Applied Mechanics Reviews*, 55(1):35–60.

[Perrone and Kao, 1975] Perrone, N. and Kao, R. (1975). A general finite difference method for arbitrary meshes. *Computers & Structures*, 5(1):45 – 57.

[Pham et al., 2013] Pham, B., Brancherie, D., Davenne, L., and Ibrahimbegovic, A. (2013). Stress-resultant models for ultimate load design of reinforced concrete frames and multi-scale parameter estimates. *Computational Mechanics*, 51(3):347–360.

[Rethore et al., 2007] Rethore, J., Borst, R. d., and Abellan, M.-A. (2007). A two-scale approach for fluid flow in fractured porous media. *International Journal for Numerical Methods in Engineering*, 71(7):780–800.

[Rethore et al., 2008] Rethore, J., de Borst, R., and Abellan, M.-A. (2008). A two-scale model for fluid flow in an unsaturated porous medium with cohesive cracks. *Computational Mechanics*, 42(2):227–238.

[Saksala, 2014] Saksala, T. (2014). Rate-dependent embedded discontinuity approach incorporating heterogeneity for numerical modeling of rock fracture. *Rock Mechanics and Rock Engineering*, 48:1605–1622.

[Saksala et al., 2015] Saksala, T., Brancherie, D., Harari, I., and Ibrahimbegovic, A. (2015). Combined continuum damage-embedded discontinuity model for explicit dynamic fracture analyses of quasi-brittle materials. *International Journal for Numerical Methods in Engineering*, 101(3):230–250.

[Schrefler et al., 2006] Schrefler, B. A., Secchi, S., and Simoni, L. (2006). On adaptive refinement techniques in multi-field problems including cohesive fracture. *Computer Methods in Applied Mechanics and Engineering*, 195(4-6):444 – 461.

[Secchi and Schrefler, 2012] Secchi, S. and Schrefler, B. (2012). A method for 3-d hydraulic fracturing simulation. *International Journal of Fracture*, 178(1-2):245–258.

[Secchi and Schrefler, 2014] Secchi, S. and Schrefler, B. A. (2014). Hydraulic fracturing and its peculiarities. *Asia Pacific Journal on Computational Engineering*, pages 1–8.

[Shi, 1992] Shi, G. (1992). Discontinuous deformation analysis: a new numerical model for the statics and dynamics of deformable rock structures. *Engineering Computations*, 9(2):157–168.

[Simo et al., 1993] Simo, J., Oliver, J., and Armero, F. (1993). An analysis of strong discontinuities induced by strain-softening in rate-independent inelastic solids. *Computational Mechanics*, 12(5):277–296.

[Simo and Rifai, 1990] Simo, J. C. and Rifai, M. S. (1990). A class of mixed assumed strain methods and the method of incompatible modes. *International Journal for Numerical Methods in Engineering*, 29(8):1595–1638.

[Smoljanovic et al., 2013] Smoljanovic, H., Zivaljic, N., and Nikolic, Z. (2013). A combined finite-discrete element analysis of dry stone masonry structures. *Engineering Structures*, 52:89 – 100.

[Stagg and Zienkiewicz, 1968] Stagg, K. G. and Zienkiewicz, O. C. (1968). *Rock Mechanics in Engineering Practice*. John Wiley & Sons Ltd.

[Stambuk-Cvitanovic, 2012] Stambuk-Cvitanovic, N. (2012). *Investigation on the effects of intact specimens shape deviations on limestone rock mechanical properties*. PhD thesis, University of Split, Croatia: Faculty of Civil Engineering, Architecture and Geodesy.

[Stambuk-Cvitanovic et al., 2015] Stambuk-Cvitanovic, N., Nikolic, M., and Ibrahimbegovic, A. (2015). Influence of specimen shape deviations on uniaxial compressive strength of limestone and similar rock. *International Journal of Rock Mechanics and Mining Sciences*. in press.

[Strouboulis et al., 2000] Strouboulis, T., Babuska, I., and Copps, K. (2000). The design and analysis of the generalized finite element method. *Computer Methods in Applied Mechanics and Engineering*, 181(1-3):43 – 69.

[Strouboulis et al., 2001] Strouboulis, T., Copps, K., and Babuska, I. (2001). The generalized finite element method. *Computer Methods in Applied Mechanics and Engineering*, 190(32-33):4081 – 4193.

[Taylor, 2011] Taylor, R. (2011). *FEAP - Finite Element Analysis Program*. University of California, Berkeley, http://www.ce.berkeley.edu rlt.

[Terzaghi, 1943] Terzaghi, K. (1943). *Theoretical Soil Mechanics*. Wiley.

[Tsang and Tsang, 1987] Tsang, Y. W. and Tsang, C. F. (1987). Channel model of flow through fractured media. *Water Resources Research*, 23(3):467–479.

[Vassaux et al., 2015] Vassaux, M., Richard, B., Ragueneau, F., Millard, A., and Delaplace, A. (2015). Lattice models applied to cyclic behavior description of quasi-brittle materials: advantages of implicit integration. *International Journal for Numerical and Analytical Methods in Geomechanics*, 39(7):775–798.

[Washizu, 1982] Washizu, K. (1982). *Variational Methods in Elasticity and Plasticity*. Pergamon Pr., 3rd edition edition.

[Wawersik and Fairhurst, 1970] Wawersik, W. and Fairhurst, C. (1970). A study of brittle rock fracture in laboratory compression experiments. *International Journal of Rock Mechanics and Mining Sciences & Geomechanics Abstracts*, 7(5):561 – 575.

[Wheel, 1996] Wheel, M. A. (1996). A geometrically versatile finite volume formulation for plane elastostatic stress analysis. *The Journal of Strain Analysis for Engineering Design*, 31(2):111–116.

[Wriggers, 2006] Wriggers, P. (2006). *Computational Contact Mechanics*. Springer Berlin Heidelberg.

[Zheng et al., 2003] Zheng, Y., Burridge, R., and Burns, D. (2003). Reservoir simulation with the finite element method using biot poroelastic approach. Massachusetts Institute of Technology. Earth Resources Laboratory.

[Zienkiewicz et al., 1983] Zienkiewicz, O. C., Emson, C., and Bettess, P. (1983). A novel boundary infinite element. *International Journal for Numerical Methods in Engineering*, 19(3):393–404.

[Zienkiewicz and Taylor, 2000] Zienkiewicz, O. C. and Taylor, R. L. (2000). *Finite Element Method*. Butterworth-Heinemann, 5th edition edition.

[Zivaljic et al., 2014] Zivaljic, N., Nikolic, Z., and Smoljanovic, H. (2014). Computational aspects of the combined finite-discrete element method in modelling of plane reinforced concrete structures. *Engineering Fracture Mechanics*, 131:669 – 686.

[Zivaljic et al., 2013] Zivaljic, N., Smoljanovic, H., and Nikolic, Z. (2013). A combined finite-discrete element model for rc structures under dynamic loading. *Engineering Computations*, 30(7):982–1010.